2014

Development of novel materials for rechargeable lithium batteries

Xuanwen Gao
University of Wollongong

UNIVERSITY OF WOLLONGONG

Institute for Superconducting & Electronic Materials

(ISEM)

DEVELOPMENT OF NOVEL MATERIALS FOR

RECHARGEABLE LITHIUM BATTERIES

Xuanwen Gao

This thesis is presented as part of the requirement for the

Award of the Degree of

Doctor of Philosophy

The University of Wollongong

August 2014

DEDICATION

For my father and mother,

Who love and support me all the time

CERTIFICATE OF ORIGINALITY

I, Xuanwen Gao, declare that this thesis, submitted in fulfilment of the requirements for the award of Doctor of Philosophy of Engineering-Research, in the Institute for Superconducting & Electronic Materials, Faculty of Engineering, University of Wollongong, is wholly my own work unless otherwise referenced or acknowledged. This document has not been submitted for qualifications at any other academic institution.

Xuanwen Gao

August, 2014

(Signature)……

Table of Contents

Table of Figures

List of Tables

ABSTRACT

In the field of electrical energy storage, lithium ion batteries (LIBs) are considered as one of the most promising technologies due to their particularly higher energy density and longer shelf life, as well as they do not suffer from the serious memory effect problems that afflict Ni-MH batteries. Graphite and $LiCoO_2$ are currently the most common commercial anode and cathode materials for the LIB, but they still suffer from low theoretical capacities of 372 mAh g^{-1} and 170 mAh g^{-1}, respectively. Such low discharge capacity would be unable to satisfy the growing demand for large-scale potential lithium ion battery applications, such as electric vehicles (EVs), hybrid electric vehicles (HEVs), and stationary energy storage for solar and wind electrical energy generation. Therefore, the electrical performance of active electrode materials in rechargeable lithium ion batteries must continue to be improved. In this doctoral work, several promising materials for both anode and cathode electrodes were synthesized and combined with conductive polymer to further improve their electrochemical performance. These include LiV_3O_8-polyaniline, Germanium-polypyrrole, and $LiNi_{0.5}Mn_{1.5}O_4$-polypyrrole composites. Monodisperse porous $Ni_{0.5}Zn_{0.5}Fe_2O_4$ nanospheres are also successfully synthesized by the solvothermal method and their electrical performances as novel anode materials for LIB are investigated in detailed. In addition, another key aspect for the electrochemical performance of LIB is the stability of the electrolyte. The most widely used electrolyte for lithium ion batteries is $LiPF_6$ dissolved in ethylene carbonate (EC), dimethyl carbonate (DMC) and diethyl carbonate (DEC). The battery performance may be limited, however, by the highly oxidizing conditions at high voltage (> 4.5 V). Herein, room temperature ionic liquid was used as a new type of electrolyte for the

high-voltage cathode material $LiNi_{0.5}Mn_{1.5}O_4$, and the relationship between the electrolyte characteristics and the performance of $Li/LiNi_{0.5}Mn_{1.5}O_4$ cells at the high potential of 5.1 V was studied in more detail.

Anode materials for the LIBs

Nano-Germanium/polypyrrole composite has been synthesized by a simpe chemical reduction method in aqueous solution. The Ge nanoparticles were directly coated on the surface of the polypyrrole. The morphology and structural properties of samples were determined by X-ray diffraction, scanning electron microscopy (SEM) and transmission electron microscopy (TEM). Thermogravimetric analysis was carried out to determine the polypyrrole content. The electrochemical properties of the samples have been investigated and their suitability as anode materials for the LIB was examined. The discharge capacity of the Ge nanoparticles in the Ge-polypyrrole composite was calculated as 1014 mAh g^{-1} after 50 cycles at the 0.2 C rate, which is much higher than that of pristine germanium (439 mAh g^{-1}). The composite also demonstrates high specific discharge capacity at different current rates (1318, 1032, 661, and 460 mAh g^{-1} at 0.5, 1.0, 2.0, and 4.0 C, respectively). The superior electrochemical performance of Ge-polypyrrole composite could be attributed to the polypyrrole core, which provides an efficient transport pathway for electrons. SEM images of the electrodes have demonstrated that polypyrrole can also act as a conductive binder and alleviate the pulverization of electrode caused by the huge volume changes of the nanosized germanium particles during Li^+ intercalation/de-intercalation.

Monodisperse porous $Ni_{0.5}Zn_{0.5}Fe_2O_4$ nanospheres have been successfully synthesized by the solvothermal method. The diameter of the nanospheres can be tuned by controlling the reactant concentration. Lower reactant concentration is favoured for the synthesis of mesoporous $Ni_{0.5}Zn_{0.5}Fe_2O_4$ nanospheres with higher surface area. The electrochemical results show that mesoporous $Ni_{0.5}Zn_{0.5}Fe_2O_4$ nanospheres exhibit high reversible specific capacity (1110 mAh g^{-1}) for Li storage and high capacity retention, with 700 mAh g^{-1} retained up to 50 cycles. The excellent electrochemical properties could be attributed to the large surface area and mesoporous structure. The results suggest that $Ni_{0.5}Zn_{0.5}Fe_2O_4$ could be a promising high capacity anode material for lithium ion batteries.

Cathode materials for the LIBs

LiV_3O_8-polyaniline nanocomposites have been synthesized via chemical oxidative polymerization, directed by the anionic surfactant sodium dodecyl benzene sulfate. The polyaniline particles are uniformly coated on the LiV_3O_8 nanorods. The composite with 12 wt. % polyaniline retains a discharge capacity of 204 Ah kg^{-1} after 100 cycles and has better rate capability (175 Ah kg^{-1} at 2 C, and 145 Ah kg^{-1} at 4 C) than the bare LiV_3O_8 reference electrode in the potential range of 1.5-4.0 V. The polyaniline coating can buffer the electrode dissolution into the $LiPF_6$ that occurs in LiV_3O_8 during cycling. The charge transfer resistance of the composite electrode is much lower than that of the bare LiV_3O_8 electrode, indicating that the polyaniline coating significantly increases the electrical conductivity between the LiV_3O_8 nanorods. Conductive polyaniline is also proven as a conductive binder which buffers the dissolution of LiV_3O_8 into the electrolyte and reduces the contact resistance among the nanorods, so the performance of the composite is significantly improved.

Conductive polypyrrole-coated $LiNi_{0.5}Mn_{1.5}O_4$ (LNMO) composites have been applied as another promising cathode materials in LIB, and their electrochemical properties are explored at both room and elevated temperature. The morphology, phase evolution, and chemical properties of the as-prepared samples were analyzed by means of X-ray powder diffraction, thermogravimetric analysis, Raman spectroscopy, and scanning and transmission electronic microscopy techniques. The composite with 5 wt. % polypyrrole coating shows discharge capacity retention of 92 % after 300 cycles and better rate capability than the bare LNMO electrode in the potential range of 3.5-4.9 V vs. Li/Li^+ at room temperature. At elevated temperature, the cycling performance of the electrode made from LNMO-5 wt. % polypyrrole (PPy) is also remarkably stable (~91 % capacity retention after 100 cycles). It is revealed that the polypyrrole coating can suppress the dissolution of manganese in to the electrolyte which occurs during cycling. The charge transfer resistance of the composite electrode is much lower than that of the bare LNMO electrode after cycling, indicating that the polypyrrole coating significantly increases the electrical conductivity of the LNMO electrode. Polypyrrole can also work as an effective protective layer to suppress the electrolyte decomposition arising from undesirable reactions between the cathode electrode and the electrolyte on the surface of the active material at elevated temperature, leading to high coulombic efficiency.

Ionic liquid electrolyte for the LIB

Among the high voltage cathode materials, $LiNi_{0.5}Mn_{1.5}O_4$ is of particular interest, with comparable capacity (around 140 Ah kg^{-1}) to $LiCoO_2$ and $LiFePO_4$, and with much higher specific energy (658 Wh kg^{-1}). The stability of the electrolyte is still a

major concern, however, for the high voltage spinel cathode materials because the potential range is beyond the decomposition potential of conventional electrolyte (~4.7 V vs. Li/Li$^+$). In this research work, a 5 V cathode material, LiNi$_{0.5}$Mn$_{1.5}$O$_4$ nanoparticles, was prepared via the sol-gel method. The room temperature ionic liquid, 1 M lithium bis(trifluoromethysulfony)imide (LiTFSI) in N-butyl-N-methyl-pyrrolidinium bis(trifluoromethane-sulfonyl) imide (Py14TFSI), was used as electrolyte. The electrochemical performance shows that the LiNi$_{0.5}$Mn$_{1.5}$O$_4$ nanoparticles with room temperature ionic liquid as electrolyte show comparable capacity to that of conventional electrolyte (1 M LiPF$_6$ in EC: DEC = 1:2 (v/v)), with improved coulombic efficiency at the high voltage of 5.1 V.

ACKNOWLEDGEMENTS

Finally, I would like to express my deepest respect and special thanks to my father and mother for their continued support, understanding, and encouragement during my study, which enabled me complete this thesis.

ABBREVIATIONS

BET	Brunauer-Emmett-Teller
C$_4$mpyrNTf$_2$	N-butyl-N-methylpyrrolidinium bis(trifluoromethanesulfonyle) imide
CMC	Sodium carboxymethyl cellulose
CV	Cyclic voltammetry
DEC	Diethyl carbonate
DMC	Dimethyl carbonate
EC	Ethylene carbonate
EDS	Energy dispersive spectroscopy
EMC	Ethyl methyl carbonate
EIS	Electrochemistry impedance spectroscopy
EV	Electric vehicle
FESEM	Field emission Scanning electron microscopy
HEV	Hybrid electric vehicle
HRTEM	High-resolution transmission electron microscope
HOMO	Highest occupied molecular orbital
IL	Ionic liquid
LIB	Lithium-ion battery
LiNTf$_2$	Lithium bis(trifluoromethanesulfonyl) imide
LNMO	LiNi$_{0.5}$Mn$_{1.5}$O$_4$
LUMO	Lowest unoccupied molecular orbital
MTMO	Mixed transition-metal oxide
Ni-MH	Nickel metal hydride
NMP	N-methyl-2-pyrrolidinone

NZFO	$Ni_{0.5}Zn_{0.5}Fe_2O_4$
PC	Propylene carbonate
PVP	Polyvinyl pyridine
Py	Pyrrole
PPy	Polypyrrole
*p*TS	p-toluenesulfonate
PAn	Polyaniline
PVDF	Polyvinylidene Fluoride
ROCO₂H	Carbonic acid ester
ROCO₂Li	Lithium alkyl carbonate
ROLi	Lithium alkoxide
ROH	Alcohol
RTIL	Room temperature ionic liquid
SAED	Selected area electron diffraction
SBDS	Sodium dodecylbenzenesulfonate
SEI	Solid electrolyte interphase
SEM	Scanning electron microscopy
TEM	Transmission electron microscope
TGA	Thermogravimetric analysis
XRD	X-ray diffraction
F	Faraday
mW	Miliwatt
g	Gram
mins	Minutes
hrs	Hours
M	Moles per litre

nm	Nanometre
V	Volts

Chapter 1   Introduction

Electrochemical energy storage systems (batteries) have a tremendous role in technical applications. They are used in computers, communication devices, industrial control, electric vehicles, spaceships, laboratory equipment, etc. They are also of crucial importance for portable instruments, remote control, solar power, pacemakers, and toys, to name only a selection of familiar uses. Amongst the energy storage systems, Lithium-ion batteries (LIBs) have relatively high energy density and superior performance to the lead acid battery, as well as the nickel cadmium or nickel metal hydride battery systems [1]. Lithium is also found in unlimited quantities in sea water, and concentrating it from brine is much greener (requiring just solar energy) than conventional mining. The demand for lithium could also be eased by recycling, which has already proven its value with lead-acid batteries. Therefore, LIBs have shown the greatest success in the portable electronics market over the past two decades. With the technologies emerging today, the rechargeable LIBs are further expected find applications in electric vehicles (EVs) and hybrid electric vehicles (HEVs). Compared with traditional combustion engines and gas turbines, however, the lithium ion batteries still exhibit much lower power. The overall electrochemical performance of LIBs is determined by the properties of the electrolyte, cathode, and anode materials. In this project, various different types of anode and cathode materials were prepared and their electrochemical properties were tested. In addition, a novel electrolyte made from room temperature ionic liquid (RTIL) was also tested in 5 V spinel $LiMn_{1.5}Ni_{0.5}O_4/Li$ cells to investigate its stability at high voltage.

A brief overview of the chapters in this thesis:

Chapter 1 contains the introduction and an outline of the thesis.

Chapter 2 commences with a literature review related to the lithium batteries. The chapter includes a brief overview of the history, basic concepts and principles, and the general components of rechargeable lithium ion batteries.

Chapter 3 presents the overall experimental methods and procedures used in this study, as well as the details of the starting materials and chemicals used in the synthesis and fabrication. Additional specific details are given at the beginning of each chapter as required.

Chapter 4 is devoted to germanium-polypyrrole composite with a unique core-shell structure as a promising anode material for LIBs. In recent years, germanium (Ge) has attracted much research interest due to its high theoretical capacity, up to 1623 mAh g^{-1}, which is 4 times higher than that of commercial graphite anode (only 372 mAh g^{-1}). Nevertheless, during lithiation/delithiation processes, Ge nanoparticles still suffer drastic volume changes, which will induce pulverization of the bulk materials and finally lead to isolation between the particle and the current collector. In this research work, Ge nanoparticles were deposited in-situ onto the porous polypyrrole particles by a simple chemical reduction reaction. The composite was physically characterized by field emission scanning electron microscopy and transmission electron microscopy, followed by electrochemical evaluation via galvanostatic discharge-charge cycling, cyclic voltammetry, and impedance spectroscopy. The polypyrrole core in the composite materials could not only act as an electronically conductive matrix, but also provides void space to buffer the volume changes of germanium nanoparticles during discharge/charge cycles.

Among the newly developed anode materials, zinc ferrite ($ZnFe_2O_4$) has been considered to be another promising candidate for LIB anodes because of its non-toxicity, environmental friendliness, good structural stability, and low cost. In Chapter 5, novel monodisperse porous $Ni_{0.5}Zn_{0.5}Fe_2O_4$ (NZFO) nanospheres have been successfully synthesized via a one-step solvothermal method. The diameter of the nanospheres can be controllable by the reactant concentration, which demonstrated lower reactant concentration is beneficial to the synthesis NZFO nanospheres with high surface area. The electrochemical results show that the monodisperse NZFO nanospheres can deliver high reversible specific capacity (1110 mAh g^{-1}) for Li storage and high capacity retention, with 700 mAh g^{-1} retained up to 50 cycles. The results suggest that NZFO could be a promising high capacity anode material for lithium ion batteries.

Chapter 6 discusses the synthesis and, structures of LiV_3O_8-polyaniline nanorods. Lithium vanadium oxide (LiV_3O_8) is well-known as a promising cathode material for lithium metal batteries due to its high-specific capacity, good structural stability, low cost, and good safety features. In various morphologies of LiV_3O_8 materials, LiV_3O_8 nanorods present superior electrochemical performance, in aspects such as change-discharge capacity, rate capacity, and cycling stability. Herein, the effects of the content of polyaniline (PAn) coating content on the electrochemical characteristics of LiV_3O_8 nanorods are explored. Field emission scanning electron microscopy and transmission electron microscopy analysis have revealed the morphologies of LiV_3O_8-PAn. LiV_3O_8-12 wt. % PAn shows the best electrochemical performance, and it delivers a reversible capacity of 204 mAh g^{-1} after 100 cycles in the voltage range of 1.5-4.0 V, while the bare LiV_3O_8 shows much lower discharge capacity (108 mAh g^{-1}). The PAn coating layer can buffer the LiV_3O_8 dissolution into the $LiPF_6$ electrolyte and increase the conductivity of

the electrode. It also can work as a conductive binder to protect the electrode from agglomeration and exfoliation.

The spinel $LiMn_{1.5}Ni_{0.5}O_4$ has been identified as an attractive cathode candidate for lithium-ion batteries because it has a high working voltage (~ 4.7 V vs. Li/Li^+) and low price. In Chapter 7, a series of polypyrrole/$LiMn_{1.5}Ni_{0.5}O_4$ (LNMO) composites was directly synthesized via chemical oxidative polymerization. The morphology and the electrochemical performance at room temperature (25 $^\circ$C) or elevated temperature (55 $^\circ$C) of the polypyrrole/LNMO composites were investigated. The composite with 5 wt. % polypyrrole coating shows the most stable cycling, with negligible capacity fading and the best rate performance up to 4.0 C at room temperature. At elevated temperature, the cycling performance of the electrode made from LNMO-5 wt. % polypyrrole (PPy) is also remarkably stable (~ 91 % capacity retention after 100 cycles). The PPy layer reduces the charge transfer resistance of the composite electrode due to its high electrical conductivity. It is also revealed that PPy protective layer suppresses the dissolution of manganese into the electrolyte as well as inhibiting electrolyte decomposition after stored at elevated temperature.

Safety is one of the most important requirements for commercialization of lithium-ion batteries. As a result, the replacement of conventional volatile and flammable organic alkyl carbonate electrolytes with ionic-liquid-based electrolytes has attracted much attention. In this thesis, Chapter 8 identifies a room temperature ionic liquid (RTIL) as a new electrolyte candidate, 1 M lithium bis(trifluoromethanesulfonyl) imide ($LNTf_2$) in N-butyl-N-methyl-pyrrolidinium bis(trifluoromethane-sulfonyl) imide ($C4mpyrNTf_2$), for LIB application at high voltage, based on its good electrochemical and thermal stability, high ionic conductivity, non-volatility and non-flammability. In this study, high-voltage

LiNi$_{0.5}$Mn$_{1.5}$O$_4$ (LNMO) cathode material was synthesized by the rheological phase method, and comparative study was carried out in two different electrolytes: LiPF$_6$/EC: DEC and RTIL. The electrochemical performances show that the LNMO nanoparticles using RTIL as electrolyte show comparable capacity to that with LiPF$_6$/EC: DEC, as well as significantly improved coulombic efficiency.

Finally, the main results and achievements of this doctoral thesis are summarized in Chapter 9, followed by the lists of references and publications during the period of this study.

Chapter 2   LITERATURE REVIEW

2.1 General background

In response to the needs of modern society and emerging ecological concerns, it is now essential to promote the rapid development of low-cost and environmentally friendly energy conversion and storage system. If a new energy economy is to emerge, it must be based on a cheap and sustainable energy supply. One of the most flagrantly wasteful activities is travel, and energy devices will therefore be critical for effectively levelling the cyclic nature of sustainable sources such as wind or solar power.

Electrical energy storage systems can be divided into two main categories: batteries and electrochemical capacitors (ECs). As shown in Fig. 2.1, batteries can generally store significantly more energy per unit mass than ECs, because they use electrochemical reactions called faradaic processes. Faradaic processes, which involve the transfer of charge across the interfaces between a battery's electrodes and the electrolyte solution, lead to reduction and oxidation, or redox reactions, of species at the interfaces. When a battery is charged or discharged, the redox reaction changes the molecular or crystalline structure of the electrode material, which often affects its stability, so batteries generally must be replaced after several thousand charge-discharge cycles. Therefore, much effort has been put into increasing the energy density and cycling life of batteries to meet the heavy new requirements.
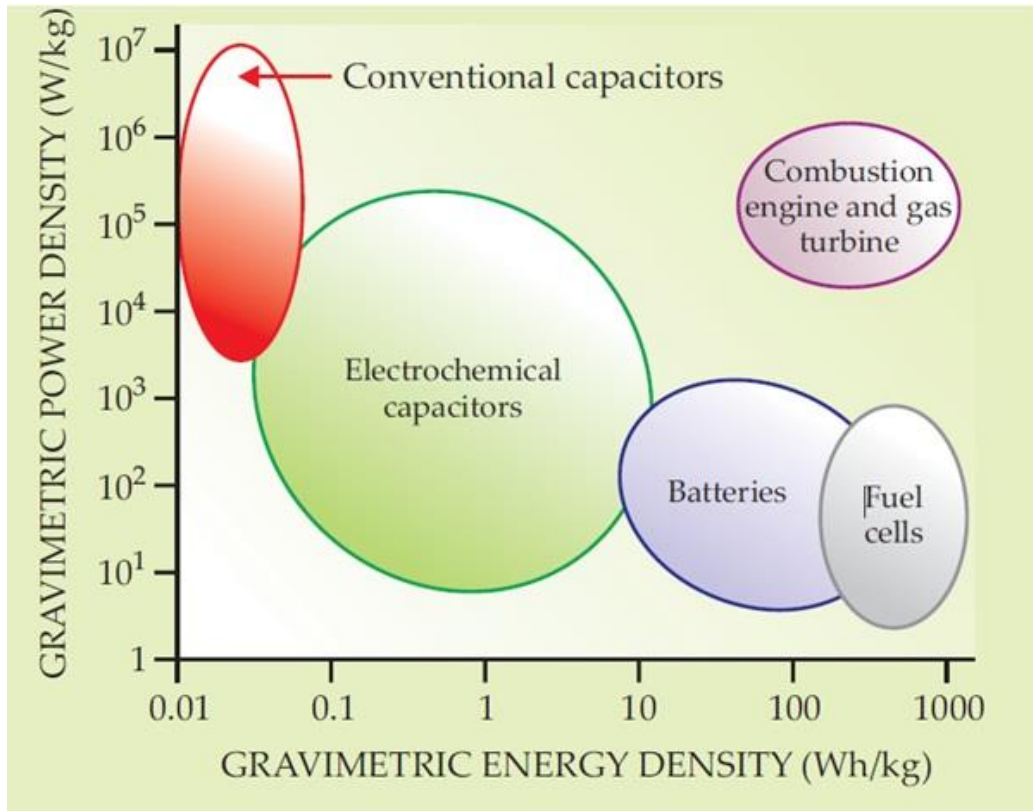
Figure 2.1 Comparison of various electrochemical energy conversion systems with the internal combustion engine and gas turbine in terms of power and energy [2].

In general, electric batteries are composed of one or more electrochemical cells that convert stored chemical energy into electrical energy. Each cell contains a positive terminal, or cathode, and a negative terminal, or anode. Electrolytes allow ions to move between the electrodes and terminals, which allows current to flow out of the battery to perform work. When these electrodes are connected by means of an external device, electrons spontaneously flow from the more negative to the more positive potential. Ions are transported through the electrolyte, maintaining the charge balance, and electrical energy can be tapped by the external circuit.

Today, commercially available rechargeable batteries include lithium-ion, nickel-metal-hydride, and nickel-cadmium devices. As shown in Fig. 2.2, lithium-ion and other

7

lithium-based batteries have the highest energy densities (per unit volume or per unit mass) of all rechargeable batteries, and such high energy outputs of Li-based batteries are mainly a result of the electrochemical and physicochemical properties of Li. As the lightest metal, Li has a theoretical gravimetric capacity storable charge per unit weight of 3860 mAh g^{-1}. Moreover, Li is the strongest metal reducing agent. A Li anode thus generates a large potential difference between the anode and cathode, which leads to a larger energy output [3]. Since Sony Corporation commercialized the first lithium-ion battery (LIB), billons of lithium-ion cells have been produced for electronic devices, such as laptop computers, cell phones, cameras, etc., and account for more than 60 % of worldwide sales value in portable devices. In addition, LIBs have conquered nickel metal hydride (Ni-MH) batteries and are now being used in power tools. There are continuous demands, however, for batteries with higher power and longer cycling life to power newly emerging electronic devices and advanced communications. Recently, the LIB has come to be further expected to enter the hybrid electric-vehicle market and is a serious contender to power the electric cars of the future. In response to the needs of these potential uses, it is essential that there is rapid development of next-generation LIBs with high energy density, long cycle life, low cost, and high safety.
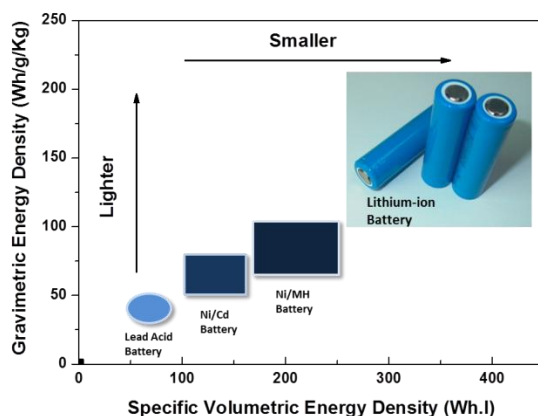
Figure 2.2 Comparison of the different battery technologies in terms of volumetric and gravimetric energy density [2].

2.2 Brief History

The earliest electrochemical energy storage system which may have served as a battery, the Baghdad battery, can be dated back to ancient times and it is quite simple and natural. In 1799, Alessandro Volta invented the first true battery, which came to be known as the voltaic pile, and discovered the first practical method of generating electricity [3]. The voltaic pile consisted of pairs of copper and zinc discs piled on top of each other, separated by a layer of cloth or cardboard soaked in brine. This voltaic pile produced a continuous and stable current of electricity when the two discs were connected by a wire conductor.

In 1836, a British chemist named John Frederic Daniell found a way to eliminate the hydrogen produced by the earlier batteries. He invented the Daniell cell, which is composed of a copper pot filled with a copper sulphate solution, in which was immersed an unglazed earthenware container filled with sulphuric acid and zinc electrode. The earthenware barrier was porous, which allowed ions to pass through but kept the solution from mixing. Without this barrier, when no current was drawn the copper ions would drift to the zinc anode and undergo reduction without producing a current, which would end the battery's life. Over time, copper bulid-up would block the pores in the earthenware barrier and cut short the battery's life. Nevertheless, the Daniell cell was a great improvement over the existing technology used in the early days of battery development and was the first practical source of electricity. It provided a longer and more reliable current than the voltaic cell because the electrolyte deposited copper (a conductor) rather than hydrogen (an insulator) on the cathode.

9

Sometime during the 1860s, a Frenchman by the name of Callaud invented a variant of the Daniell cell called the gravity cell. This simpler version dispensed with the porous barrier. The gravity cell consisted of a glass jar, in which a copper cathode sat on the bottom and a zinc anode was suspended beneath the rim. Copper sulphate crystals would be scattered around the cathode and then the jar would be filled with distilled water. As the current was drawn, a layer of zinc sulphate solution would form at the top around the anode. This top layer was kept separate from the bottom copper sulphate layer by its lower density and by the polarity of the cell. This simpler system reduced the internal resistance of the system and, thus the battery yielded a stronger current. It quickly became the battery of choice for the American and British telegraph networks. From then on, many different types of primary or rechargeable batteries were developed in the following centuries, such as the zinc-carbon battery, lead-acid battery, nickel-cadmium battery, zinc-air batter, alkaline battery, etc.

Experimentation with the LIB began in 1912 under G. N. Lewis, and in the 1970s, lithium batteries were being sold. In 1980, Prof. John B. Goodenough discovered the $LiCoO_2$ cathode (positive electrode) [4] and a French research scientist, Rachid Yazami, discovered the graphite anode (negative electrode) [5]. This led a research team managed by Akira Yoshino of Asahi Chemical, Japanto build the first LIB prototype in 1985, a rechargeable and more stable version of the lithium battery, followed by Sony, which commercialized the lithium ion battery in 1991.

In 1997, the lithium-ion polymer battery was released. These batteries hold their electrolyte in a solid polymer composite instead of a liquid solvent, and the electrodes and separators are laminated with each other. The latter difference allows the battery to be encased in a flexible wrapping instead of a rigid metal casing, which means that such

batteries can be specifically shaped to fit a particular device. They also have a higher energy density than normal lithium ion batteries. These advantages have made it the battery of choice for portable electronics such as mobile phones and personal digital assistants, as they allow for more flexible and compact design.

2.3 Basic concepts

In a LIB, the Li^+ ions shuttle between the cathode and anode hosts during the discharge and charge processes. The principles of Li-ion battery operation are shown in Fig. 2.3. In the discharge process, the anode is electrochemically oxidized, which results in the release, or deintercalation, of Li ions into the electrolyte. At the same time, electrons move through the external circuit and travel toward the cathode. The Li ions travel through the electrolyte to compensate for the negative charge flowing through the external circuit, which results in the uptake, or intercalation, of Li ions into the cathode. When the battery is recharged, the reverse processes occur. In this mode of operation, Li-ion batteries are generally called rocking-chair batteries to describe the toggling of Li ions back and forth between anode and cathode. Basically, the reactions on electrodes can be described by two half-cell reactions:

At the cathode: $aA + ne^- + nLi^+ \rightarrow cC$ (2.1)

At the anode: $bB \rightarrow dD + ne^- + nLi^+$ (2.2)

Overall reaction: $aA + bB \leftrightarrow cC + dD$ (2.3)

- Potential

Each of electrochemical reactions is related to a standard electrode potential, E^0, which can be calculated from Gibbs free energy (ΔG). The basic thermodynamic equations for the calculation of ΔG are given as:
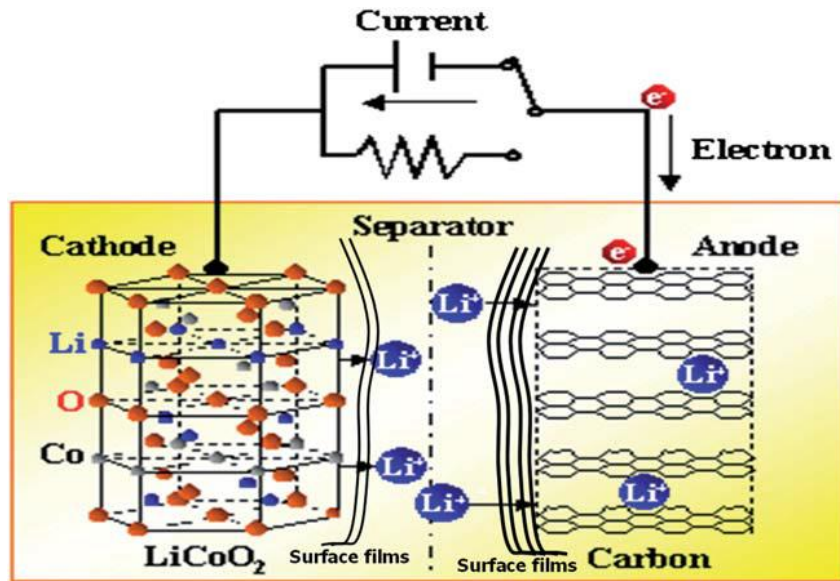
Figure 2.3 A schematic representation of the most commonly used Li-ion battery based on graphite anode and $LiCoO_2$ cathodes[6].

$$\Delta G = \Delta H^0 - T\Delta S^0 \tag{2.4}$$

Where, ΔH = enthalpy

T = absolute temperature

ΔS^0 = entropy

If we assume that the released Gibbs energy is all transformed to electrical work, then

$$\Delta G = W = -nFE^0 \tag{2.5}$$

Where, $-\Delta G$ = standard Gibbs free energy

n = number of electrons transferred

F = Faraday constant (96487 C)

And under standard conditions:

$$E^0 = {-\Delta G}/{nF} \tag{2.6}$$

- Open circuit voltage (V_{oc})

The design of a LIB system also requires careful selection of electrode pairs to obtain a high operating voltage (V_{oc}). Figure 2.4 is a schematic diagram of the relative electron energies in the electrodes and the electrolyte of thermodynamically stable battery cell with an aqueous electrolyte[7]. The energy separation E_g of the lowest unoccupied molecular orbital (LUMO) and the highest occupied molecular orbital (HOMO) of the electrolyte is the "window" of the electrolyte. The two electrodes are electronic conductors with anode and cathode electrochemical potentials μ_A and μ_C. An anode with a μ_A above the LUMO will reduce the electrolyte unless a passivation layer creates a barrier to electron transfer from the anode to the electrolyte LUMO; and a cathode with a μ_C below the HOMO will oxidize the electrolyte unless a passivation layer blocks electron transfer from the electrolyte HOMO to the cathode. Therefore, the anode and cathode materials are thermodynamically stable within the window of the electrolyte, which constrains the open-circuit voltage V_{oc} of a battery cell to:

$$V_{oc} = (\mu_A - \mu_C)/e \leq E_g \tag{2.7}$$

In this formula, e is the magnitude of the electron charge. A passivating solid/electrolyte-interphase (SEI) layer at the electrode/electrolyte boundary can give kinetic stability to a larger V_{oc} provided that $eV_{oc} - E_g$ is not too large.
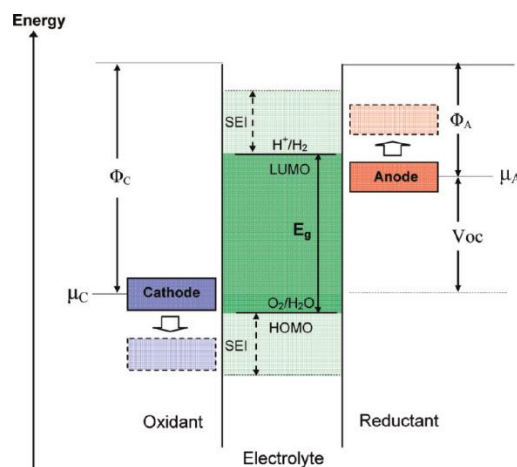
Figure 2.4 Schematic open-circuit energy diagram of an aqueous electrolyte, Φ_A and Φ_C are the anode and cathode work functions[7].

- Discharging

The conversion of the chemical energy stored within a cell to electrical energy, and the subsequent withdrawal of this electrical energy into a load.

- Charging

Charging is the operation in which energy is put into a secondary cell or rechargeable battery by forcing an electric current. The battery is restored to its original charged condition through charging.

- Overcharging

Attempting to charge a battery beyond its electrical capacity can also lead to a battery explosion, leakage, or irreversible damage to the battery. It may also cause damage to the charger or device in which the overcharged battery is later used.

- Electrical conductivity

The electrical conductivity is a measure of ease, with which a material conduct current.

- Short circuit

A short circuit is an electrical circuit that allows a current to travel along an unintended path, often where essentially no (or a very low) electrical impedance is encountered. It is an abnormal connection between two nodes of an electric circuit intended to be at different voltages, which results in an excessive electric current/overcurrent, limited only by the Thevenin equivalent resistance of the rest of the network, and potentially causes circuit damage, overheating, fire, or explosion.

- Theoretical specific capacity

The theoretical specific capacity is an important parameter to evaluate the active materials. It can be calculated from the equation:

$$Q_{tsc} = \frac{n \times F}{3600.M} \tag{2.8}$$

Where n is the number of moles of electrons transfered in the electrochemical reaction, F is the Faraday constant (96485 C), and M is the molecular weight of the active materials.

- Specific capacity

The specific charge capacity (Q_c) or specific discharge capacity (Q_d) can be calculated based the total amount of electrons transferred:

$$Q_c/Q_d = \frac{I \times t}{m} \tag{2.9}$$

where I is the current density (A), t is the time (h), and m is the mass of the active materials (g). The unit of specific capacity is mAh g^{-1} or Ah kg^{-1}.

- Energy density

Energy density is the amount of energy stored in a region of space per unit volume or mass. It is usually desirable that the energy density stored in a LIB system is as high as possible. The unit of energy density is Wh kg^{-1}, and energy density can be calculated by Eq. (2.10).

$$Energy\ density = \frac{E \times Q}{1000} \tag{2.10}$$

where E is the voltage (V), and Q is the specific capacity (Ah kg^{-1}).

- Charge/discharge rate

The term charge/discharge rate or C-rate is employed to estimate how fast lithium can be transferred. 1 C denotes either the theoretical charge capacity of a cell or the nominal

capacity of a cell. Charge/discharge rate is an expression of the speed with which a battery is being charged/discharged, at a specific point in time. For example, C/5 means a current allowing a full change/discharge in 5 hours.

- Irreversible capacity loss

Irreversible capacity results from irreversible lithium reactions which do not result in insertion into or extraction from the active materials. It equals the difference between the charge capacity and the discharge capacity for the nth cycle.

Irreversible capacity loss $= n^{th} Q_c - n^{th} Q_d$ (2.11)

- Capacity retention

Capacity retention, which is always used to evaluate the cycling stability, is the ratio of discharge capacity for the nth cycle to initial discharge capacity.

Capacity retention $= {C_n}/{C_1} \times 100 \%$ (2.12)

Where C_n is the discharge capacity for the nth cycle, and C_1 is the initial discharge capacity.

- Coulombic efficiency

Coulombic efficiency is defined as the ratio of the output of charge by a battery to the input of charge. Coulombic efficiency is determined by the internal resistance of a cell.

Coulombic efficiency $= {Q_d}/{Q_c} \times 100 \%$ (2.13)

- Elevated temperature

Chemical reactions take place much more readily at high temperatures than at low. Furthermore, the active materials are more porous and the internal resistance less at higher temperatures. Opposed to this is the fact that at high temperatures, the acid from

16

the electrolyte attacks the grids and the active materials, and serious solid electrolyte interphase (SEI) is formed, even though no current is taken from the battery. Other injurious effects include the destructive action of hot acid on the wooden separators used in batteries. Greater expansion of active material will also occur, and this expansion is not, in general, uniform over the surface of the plates. Therefore, charging temperature limits for LIBs are stricter than the operating limits. The chemical reaction in LIBs can perform well at elevated temperature (> 45 ˚C). High temperatures during charging may lead to battery degradation and discharge at elevated temperatures will also degrade battery performance.

2.4 Cathode materials

The choice of the positive electrode depends on whether we are dealing with rechargeable Li-metal or Li-ion batteries. For rechargeable Li batteries, owing to the use of metallic Li as the negative electrode, the positive electrode does not need to be lithiated before cell assembly. In contrast, for LIB, because the carbon negative electrode is empty (no Li); the positive one must act as a source of Li, thus requiring the use of air-stable Li-based intercalation compounds to facilitate the cell assembly. Figure 2.5 displays the alternative cathode materials and their corresponding characteristics. The compounds for positive electrodes are generally divided into five major categories: the layered transition metal oxides, the spinel oxides, the olivines, the vanadates and electrochemically active polymers [8].
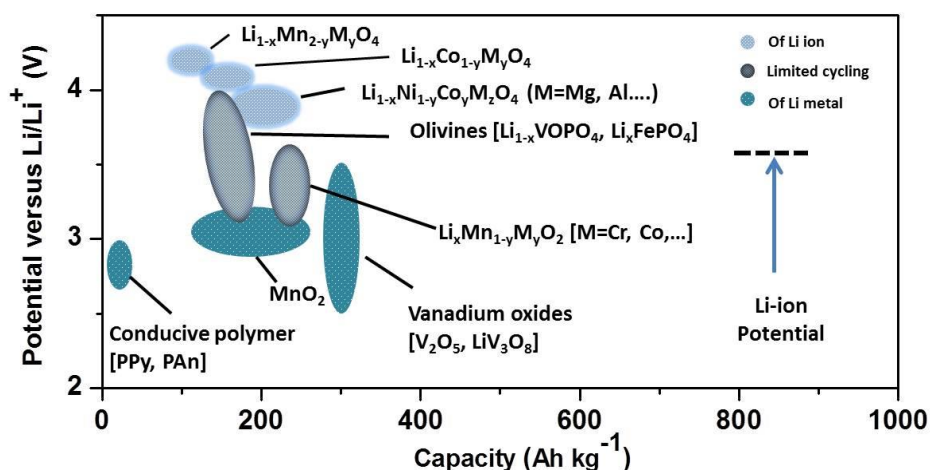
Figure 2.5 Voltage versus capacity for positive electrode materials presently that are used or under serious considerations for the next generation of rechargeable Li-based cells. The output voltage values for Li-ion cells and the Li-metal cell are presented [8].

In general, the active materials for the positive electrode are much less developed than for the anode. $LiCoO_2$ has been used most extensively in practical applications, but cobalt is relatively expensive and toxic. Capacities obtained from conventional inorganic cathode materials are limited by the number of lithium ions that they can intercalate while remaining structurally stable. When Li ions are deintercalated from an oxide, the material's lattice will contract. Extraction of all, or even 80 % - 90 %, of the Li ions would change the structure so much that the electrode would fail after a small number of charge-discharge cycles [9]. In practice, therefore, batteries are generally designed so that only about half of the Li ions are ever deterincalated from the cathode. The gravimetric capacities of cathode materials are thus limited to 120 to 250 mAh g^{-1} [10].

2.4.1 Layered transition metal oxides

The most common layered material used as cathode in commercial lithium-ion cells is

18

layered $LiCoO_2$ (Figure 2.6). In layered $LiCoO_2$, the lithium and the Co^{3+} ions occupy alternate (111) planes of the cubic rock-salt structure[11]. The lithium ion intercalates into or de-intercalates reversibly from the CoO_2 layers[11, 12].

$$yC + LiCoO_2 \leftrightarrow Li_xC_y + Li_{(1-x)}CoO_2, x \approx 0.5, y = 6, voltage \approx 3.7\ V \qquad (2.14)$$
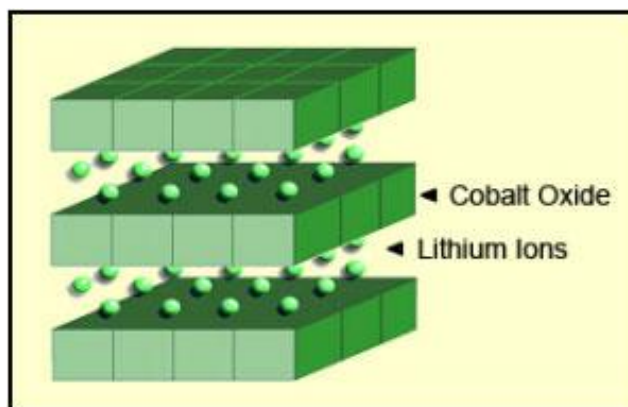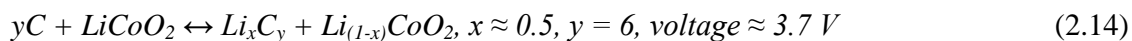
Figure 2.6 The two-dimensional crystal structure of $LiCoO_2$ [13].

$LiCoO_2$ has desirable electrochemical properties, such as good structural stability and moderately high capacity, and fabrication of high-quality $LiCoO_2$ is facile. The major drawbacks of $LiCoO_2$ are low specific capacity, high cost and toxicity. Actually, layered $LiNiO_2$ was initially considered as the commercial cathode material for Li-ion batteries, because it displayed favourable specific capacity ($\geq$ 180 mAh g^{-1}) compared with only 140 mAh g^{-1} for $LiCoO_2$ [14]. These expectations were dismissed for safety reasons, however, after exothermic oxidation of the organic electrolyte by the collapsing delithiated Li_xNiO_2 structure. Delithiated Li_xCoO_2 was found to be more thermally stable than its Li_xNiO_2 counterpart. Recently, substitution of Co for Ni in $LiNi_{1-x}Co_xO_2$ was adopted to provide a partial solution to the safety concerns surrounding $LiNiO_2$ for the next generation of rechargeable Li-based cells[15, 16].

Although the reversible delithiation of $LiCoO_2$ beyond 0.5 Li is feasible, delithiation for commercial applications has been limited to that value for safety reasons (charge cut-off limited to around 4.2 V). Several routes have been investigated to circumvent these safety and capacity issues. Among them was the successful stabilization of the layered structural framework by an electrochemically inert di-, tri- or tetravalent cationic substitute for Ni or Co (Al, Ga, Mg or Ti). This led to $LiNi_{1-x}Ti_{x/2}Mg_{x/2}O_2$ phases, which were claimed to be safe and displayed practical capacities of 180 mAh g^{-1} [17]. Another line of investigation involved the synthesis of layered $LiFeO_2$ and $LiMnO_2$ phases to take advantage of the Fe^{4+}/Fe^{3+} and Mn^{4+}/Mn^{3+} redox couples, respectively. Most of attempts to prepare electrochemically attractive $LiFeO_2$ failed, however, in spite of numerous and diverse synthesis methods. In contrast, research on $LiMnO_2$ has been more fruitful [18], and the structural instability where the layered phase reverts to the spinel $Li_xMn_2O_4$ upon cycling has recently been diminished through cationic substitution by chromium ($Li_{1+x}Mn_{0.5}Cr_{0.5}O_2$) [19]. This kind of material exhibits a capacity of 190 mAh g^{-1} (larger than that expected from the full oxidation of Mn^{3+} to Mn^{4+}) with little capacity fading upon cycling. It seems that within these materials, the role of Mn is to stabilize the layered structure of the chromium oxide, and that the large capacity is based in the Cr oxidation state, which changes reversibly from +3 to +6.

2.4.2 Spinel Oxides

Recently, the use of manganese oxides in Li-ion batteries has been stimulated. This is because spinel $LiMn_2O_4$ has a cubic spinel structure (Figure 2.7), where Li^+ ions diffuse within the structure, first moving from the 8a site to the neighbouring empty octahedral 16c site, and then to the next 8a site, in such a way that the Li ion takes the diffusion path (8s-16c-8a) [20].
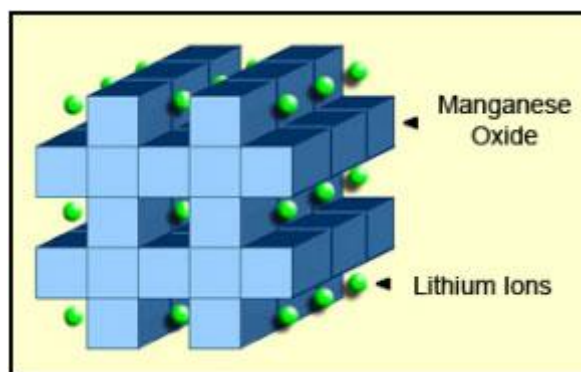
Figure 2.7 Two-dimensional crystal structure of $LiMn_2O_4$ [13].

The discharge curve for $Li_xMn_2O_4$ has two main peaks, occurring near 4 V and 3 V versus Li^+/Li, which correspond to the addition of one more Li, resulting in $Li_2Mn_2O_4$. The pristine $LiMn_2O_4$, although possessing ~ 10% less capacity than $LiCoO_2$, has an advantage in terms of cost and is perceived as being 'green' (that is, non-toxic and from abundant material source). Additionally, it has long been recognized as a potential alternative cathode. Its implementation has been delayed at elevated temperature, because of its limited cycling and storage performances resulting from the undesirable dissolution of Mn [21]. This problem can be addressed by the substitution of different cations (Li, B, Mg, Al, Fe, Co, Ni, or Zn) or by the introduction of nanodomain structure [22]. Coating the particles with a stabilizing surface layer may also help to alleviate such problems but will reduce the rate of lithium intercalation.

$LiNi_{0.5}Mn_{1.5}O_4$ is another promising example in the manganese family. This material is characterized by a two-phase electrochemical process, which is reflected in a flat voltage profile at 4.5 V vs. Li [23]. Its theoretical specific capacity is 146 mAh g^{-1} [24]. The advantage for this kind of material is its high working voltage, which gives it has more than 30 % greater energy density than what is associated with conventional lithium manganese spinel. On the other hand, the practical use of this cathode material is still prevented by

the lack of suitable electrolyte media, since the presently available organic carbonate solutions are not totally compatible with the high voltage of the lithium nickel manganese oxide, especially in the course of its charge process and at elevated temperature (> 55 °C)[25].

2.4.3 Transition Metal Phosphates

Transition metal phosphates, $Li_xM_y(PO_4)$ (M = transition metal) have been proposed as promising cathode materials for Li-ion batteries. Amongst the various compounds, $LiFePO_4$ possesses the advantages of potentially low cost, rich natural resources, and environmental friendliness, so that it has gained significant attention. It forms in the orthorhombic olive structure with the *Pnma* space group, in which the strong P-O covalency stabilizes the Fe^{3+}/Fe^{2+} redox couple through the Fe-O-P inductive effect, as shown in Fig. 2.8. FeO_6 and PO_4 form the zigzag skeleton by sharing oxygen, and Li-ions are located in the octahedral channel [26]. The FeO_6 octahedra are connected through the corners in the *bc* -plane, and LiO_6 grows as a linear chain along the *b*-axis, while each PO_4 tetrahedron shares edges with one FeO_6 and two LiO_6[27].
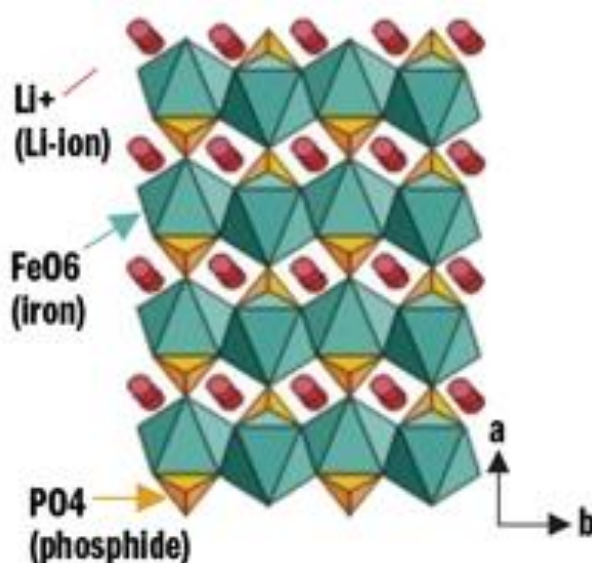
Figure 2.8 Two-dimensional crystal structure of $LiFePO_4$ [28].

The discharge potential of $LiFePO_4$ is about 3.4 V versus Li^+/Li and no obvious capacity fading is observed even after several hundred cycles. Its capacity approaches 170 mAh g^{-1}, which is higher than that of $LiCoO_2$ and comparable to that of stabilized $LiNiO_2$. Additionally, $LiFePO_4$ possesses a flat voltage plateau at 3.4 V vs. Li^+/Li, which is compatible with most existing organic electrolytes[29]. On the other hand, this material shows very low electrical conductivity at room temperature[27, 30]. Therefore, to achieve its theoretical capacity, the current density has to be controlled at a very low level. Many efforts have been made to improve the conductivity of $LiFePO_4$ by carbon-coating, forming metal-rich phosphide nanonetworks, super-valent ion doping, and cation substitution [13]. These methods simultaneously reduce the distance for Li^+ transport, and increase the electronic contact between the particles.

Following the success in the preparation of practical $LiFePO_4$ cathode materials, there have been intensive attempts to develop $LiMnPO_4$ [31, 32] and $LiCoPO_4$[33] as promising cathode materials, thereby gaining higher red-ox potential, and hence, higher energy density. The work on $LiMnPO_4$ was resulted in only partial success. Carbon-coated nano-$LiMnPO_4$ was proved to be a very stable cathode material in standard electrolyte solutions with a flat red-ox potential around 4.1 V, but a lower practical capacity (150 vs. 165 mAh g^{-1}) and a much lower rate capability, as compared to $LiFePO_4$[34, 35]. In contrast, $Li[MnFe]PO_4$ was found to be an excellent cathode material, with practical capacity approaches the theoretical one (160-165 vs. 170 mAh g^{-1}), and a very high rate capability. The optimal stoichiometry of these compounds was found to be $LiMn_{0.8}Fe_{0.2}PO_4$ [36]. Both $LiMnPO_4$ and $Li[MnFe]PO_4$ are highly stable in standard electrolyte solutions even at elevated temperatures. They can undergo very prolonged cycling, and demonstrate excellent safety features[36]. In recent years, $LiCoO_4$ has also been explored as a potential cathode material. Prolonged cycling could be demonstrated, but at a low capacity

compared to the olivine compounds (< 135 mAh g^{-1}) [37]. Intensive work on this material is presently underway, and there is a good chance of improving its performance, and bringing it up to practical importance.

2.4.4 Vanadate

One possible way to achieve higher capacities is to design materials in which the metal-redox oxidation state can change structure, and allow the insertion of more than one Li$^+$ per transition metal. Such an approach is feasible with a few V-based oxides, V^{5+} is reduced to an average state of 3.5 in Li$_3$V$_3$O$_5$ or 3.67 in Li$_5$V$_3$O$_8$ [38, 39]. Therefore, the layered trivanadate, LiV$_3$O$_8$, has attracted considerable interest as an excellent alternative candidate for use as the positive electrode in secondary lithium cells. Its layered structure can reversibly accommodate up to about 3.8 Li per formula unit with fair cyclability [40].

LiV$_3$O$_8$ can be prepared either by solid state reaction or via a sol-gel process, followed by heat treatment at different temperatures, as described by Pistoia et al. [41]. The electrochemical behaviour of such compounds has been studied in polymer or liquid electrolyte[42, 43], at 90-120 ˚C or room temperature [42, 44], respectively. It is generally agreed that the electrochemical performance of LiV$_3$O$_8$ mainly depends on the preparation process. For instance, reversible capacities between 1.8 [45] and 3 [41, 46, 47] Li per formula unit were reported during the first cycle at room temperature for samples prepared above 601 ˚C (melting point), while values between 3 [45] and 3.9 [48, 49] were obtained for samples prepared at 350 ˚C. According to some authors [50, 51], the capacity losses observed during cycling could be due to the occurrence of a two-phase phenomenon around 2.6 V, corresponding to the transformation from Li$_3$V$_3$O$_8$ to Li$_4$V$_3$O$_8$, and leading to a sudden change in structural parameters. Therefore, numerous research works have been focused

on the preparation of LiV_3O_8 nanostructures. Xu et al. prepared LiV_3O_8 nanorods by hydrothermal reaction from LiOH and V_2O_5 precursor[52]. The electrochemical performance showed that the high discharge specific capacity of 278 mAh g^{-1} was retained after 30 cycles for the sample annealed at 300 ˚C. Cui et al. used a combined sol-gel reaction and hydrothermal treatment to prepare LiV_3O_8 nanotubes[53]. Nevertheless, the disadvantage of these materials was the capacity fading, which took place very rapidly upon cycling. Doping with a conductive agent such as carbon [54] or conducting polymers [55] seems to be an attractive route to overcome these problems.

2.4.5 Li-rich layer-structured cathode

Another attractive candidate for the next-generation cathode materials is Li-rich layered oxides. Recently, Li-rich layered oxides with the formula $xLi_2MO_3\cdot(1-x)LiMO_2$ (M = Mn, Ni, Co, Fe, Cr, etc.) have been of the great interest as cathode materials in Li-ion batteries because they offer the very high reversible capacity and energy density[56]. Currently, research on Li-rich cathode materials is mainly focused on their structure and evolution of the materials upon cycling, because a good understanding of the reaction mechanism is necessary and will help to further improve the properties of Li-rich cathode materials[57]. For example, Lu et al. investigated the Li-rich layered cathode material $Li(Li_{0.2}Mn_{0.54}Ni_{0.13}Co_{0.13})O_2$, and corresponding doped materials to understand the mechanisms of capacity fade as well as the voltage decrease upon long-term cycling[58]. Their results revealed a phase-separation-like behaviour with increasing the cycle number, which was thought to be responsible for a gradual reduction in the discharge voltage. Boulineau et al. studied and observed structural evolution of Li-rich manganese-based layered oxides by using advanced transmission electron microscopy, and proposed a correlated mechanism[59]. In addition, the effects of the synthesis conditions, substitutions,

and surface treatment were also studied to enhance the electrochemical performance of Li-rich layered-oxide cathode materials[60, 61].

2.4.6 Electrochemically active polymers

Since the discovery of Shirakawa et al. in 1977 that virgin polyacetylene, $(CH)_x$, can be reversibly oxidized and reduced, and thus switched reversibly from the insulating to a semiconducting or conducting state [62], innumerable attempts have been made to utilize the redox reactions of $(CH)_x$ for battery energy storage [63-65]. Some other conducting polymers, such as polyphenylene, polypyrrole, polythiophene, and polyaniline have been proposed and investigated for charge storage, and the key parameters of Li/polymer batteries have been critically discussed.

During their electrochemical oxidation and reduction, polymer electrodes must take up or give off ions in order to maintain the electroneutrality of the material. This process is often called polymer doping/undoping. The doping is an ion insertion process that raises the redox state and electronic conductivity of the polymer [66]. The charge-compensating ions can move within the polymer. Thus a conducting polymer is actually an electronic as well as an ionic conductor. Conducting polymers exhibit the behaviour of metals or semi-conductors (Figure 2.9). Doping with an appropriate agent not only controls their conductivity, but also can affect the electrochemical and physical properties of the Li/polyer battery in response to electrical stimulation [67]. Such changes are the features behind potential application for Li-ion batteries with conducting polymers.
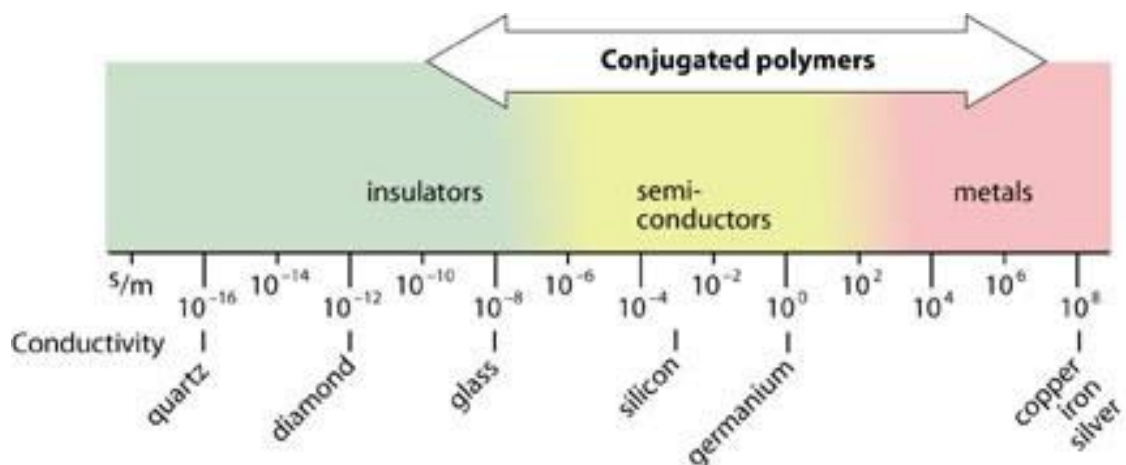
Figure 2.9 Semi-conductor and metallic properties of conjugated polymers [66].

2.4.6.1 Polypyrrole (PPy)

Polypyrrole is well known as an inherently electrically conductive polymer because the conjugation of the single and double bonds in a conjugated system is free to roam or move through the polymer chain, which induces electrical conductivity [68, 69]. Delocalised electrons along the conjugated backbone of polypyrrole result in an extended doping which is made up of valence electrons. Adding or removing electrons from the doping produces a charged unit called a polaron unit which results in the conduction of electricity, as shown in Fig. 2.10 [70]. The undoped polypyrrole (in the reduced state) has a low electrical conductivity of $\sim 10^{-6}$ S/cm. The conductivity of polypyrrole in the oxidised state can be significantly increased to the level of a few tenths of S/cm through doping with anion, such as ClO_4^-, Cl^-, or PF_6^- [71].
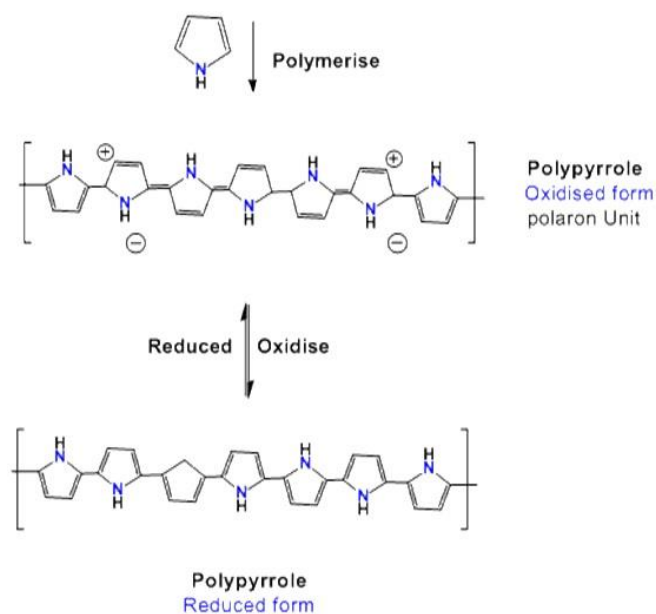
Figure 2.10 Model of conductive polypyrrole and polaron unit.

In the literature, polypyrrole is reported to be electrochemically active for lithium ion insertion and extraction in the voltage range of 2.0 to 4.5 V, with a theoretical capacity of 72 mAh g^{-1} [72, 73]. The doping level of polypyrrole and, consequently, the values of specific charge and energy attainable in Li/PPy cells at practical current densities strongly depend on the method used in fabricating the polymer electrode. For example, Panero et al. [74] measured a specific energy of 151 Wh kg^{-1} (based on the weights of the doped polymer and the Li consumed) for a Li/PPy cell with excess electrolyte at contained a PPy film about 1μm thin and was doped to a level of y = 0.24. Much higher values of specific energy, of up to 390 Wh kg^{-1} (based on the weight of the polymer) were reported by Osaka et al.[73] for their Li/LiClO$_4$-PC/PPy cells, where PC is propylene carbonate, after optimizing the PPy synthesis. Water trapped in the polymer (e.g. during the chemical synthesis in H$_2$O) also influences the specific capacity of PPy electrodes, which reaches a maximum when about 3 wt. % of water is present in PPy[75].

Recently, polypyrrole additive has been reported to be capable of working as both a

conductive agent and a cathode material for the LIB. It has been introduced into $LiMn_2O_4$ [76], V_2O_5 [77, 78], and $LiFePO_4$ [79, 80] composites; this strategy has given these cathode materials a significant enhancement of their conductivity. Pasquier et al.[81] have also coated $LiMn_2O_4$ particles with a conductive PPy layer to protect the cathode from capacity fading due to the dissolution of manganese into the electrolyte.

2.4.6.2 Polyaniline (PAn)

A conjugated polymer, polyaniline (PAn), has been considered as another promising cathode material for the Li-metal battery[82, 83]. Typically, polyaniline has two forms, emeraldine base and emeraldine salt, with different degrees of doping[84].
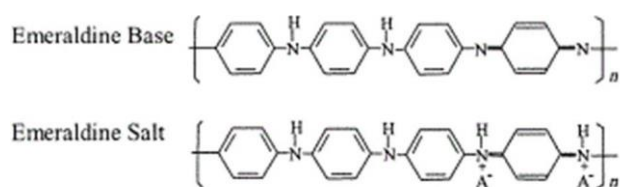
Figure 2.11 Model of conductive polyaniline[85].

The electrically conductive form of PAn (the emeraldine salt) protonates the imine nitrogen on the polymer backbone and induce charge carriers. When it is fully doped with a strong acid, the electrical conductivity of PAn is greatly increased compared to its undoped (emeraldine base) form[86]. Because of the existence of redox states in the presence of dopants (the emeraldine salt), the intrinsically electron-conducting PAn has demonstrated high specific energy ranging from 87 to 540 Wh kg^{-1} at an average discharge voltage of 3.65 V vs Li/Li^+ [87]. The cycle life of PAn electrode has also been studied in several laboratories in detail. The best result was reported by Tanaka et al.. During more than 500 constant-charge cycles at 0.1 mA cm^{-2} corresponding to a specific charge capacity of PAn of 83 Ah kg^{-1}, the PAn was remarkably stable, as no degradation

could be observed [88]. Interestingly, the specific discharge capacity of PAn generally improves with the number of charge-discharge cycles, and reaches a maximum after about 30 cycles, which is believed to be due to the progressive penetration of the electrolyte into the polymer, supplying sufficient quantities of anions for enhanced doping of the PAn [89].

Over the past two decades, several methodologies have been developed for the preparation of nanostructured PAn to investigate its electrochemistry in rechargeable batteries[90, 91]. The parameter for its potential application in the Li-ion battery is its electrical conductivity. The conductivity of PAn depends on its morphology, the acidity of the doped acid, plus the degree of doping [92]. For example, a specific charge capacity of 270 Ah kg^{-1} of PAn was found from the doping level of 0.9 that was attained in a PAn/Li cell, but due to solvent uptake and to incomplete doping (oxidation), only 160 Ah kg^{-1} of PAn could be realized during cycling [93].

2.5 Anode materials

Commercial Li-ion batteries are usually based on carbonaceous anode materials, into which the Li is inserted during charging. The resulting Li-interacted carbons show a low potential close to that of a metallic Li electrode [94]. It is recognized, however, that graphitic carbons suffer from solvent co-intercalation in propylene-carbonate-based electrolytes, which results in large interlayer expansion and subsequent degradation of the graphitic structure[95]. More importantly, the gravimetric and volumetric capacities of carbon materials are limited. The rapid development of electronic devices and electric vehicles (EVs) has fuelled demands for a much higher energy as well as a higher power density and smaller irreversible capacity for anodes. Therefore, ongoing research efforts

30

are focused on searching for carbon alternatives in the hope of finding suitable materials (Fig. 2.12). The materials investigated include Al, Si, Ge, Sn, Pb, Sb and Bi, and their alloys or oxides, which have both larger capacities and slightly more positive intercalation voltages compared to Li/Li$^+$ [8, 96].
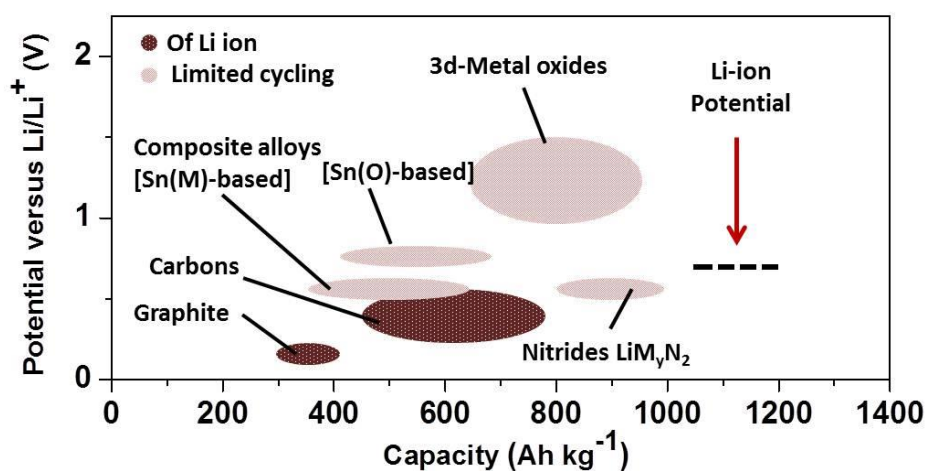
Figure 2.12 Voltage versus capacity for negative electrode materials presently used or under serious consideration for the next generation of rechargeable Li-based cells. The output voltage values for Li-ion cells are represented [8].

2.5.1 Carbonaceous anode

Graphite anode was the first commercial anode material for lithium ion batteries and is still the most widely used in the market, due to its stable specific capacity, small irreversible capacity and good cycling performance. Graphite intercalates reversibly with lithium to form LiC_6 as the final product according to the following reaction；

$$C_6 + Li^+ + e^- \rightleftharpoons LiC_6 \tag{2.15}$$

Graphite is commonly used because it has good capacity retention and low operating voltage; however, due to its low theoretical capacity of 372 mAh g^{-1}, there are many

studies on the development of high-capacity non-graphitized carbonaceous anode materials to replace graphite.

Soft carbon

(A)

Hard carbon

(B)
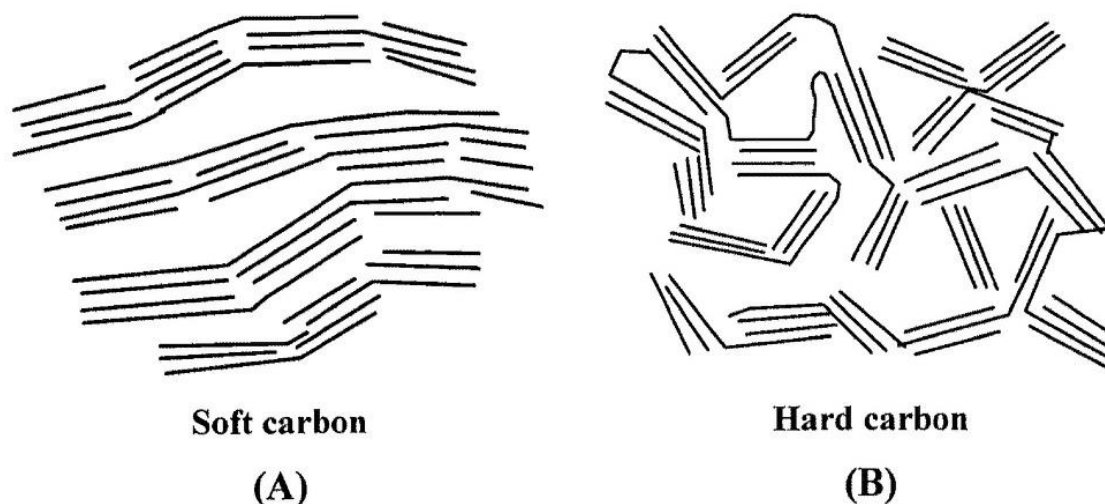
Figure 2.13 (A) Schematic diagram of a soft carbon, in which neighbouring stacks of graphene sheets or small aromatic rings are favourably oriented with respect to each other at a small angle that is conducive to growth or merging (graphitizable); (B) hard carbon (non-graphitizable)

Non-graphitized carbon materials consisted of soft carbon or hard carbon [97]. Soft carbon materials show a very high reversible Li-storage capacity but a serious voltage hysteresis during delithiation [98]. On the other hand, hard carbon shows a high capacity of 200-600 mAh g^{-1} over a voltage range of 1.5-0 V vs Li/Li$^+$ [95, 99], although hard carbon materials have disadvantages such as low initial coulombic efficiency and low tap density [100].

2.5.2 Nanosized alloy anodes

The electrochemical alloying reaction of lithium with metals has been widely studied since the 1970s. Many metals and alloys can store a large quantity of lithium by the

formation of alloys [101-103] ($Li_{4.4}Si$, which corresponds to a Li storage capacity of 4200

mAh g^{-1}, $Li_{4.4}Ge$: 1600 mAh g^{-1}, LiAl and $Li_{4.4}Sn$: 990 mAh g^{-1}, and Li_3Sb: 665 mAh g^{-1}).

The reaction usually proceeds reversibly according to the general scheme shown in Eq.

(2.16)

$$Li_xM \leftrightarrow x\ Li^+ + x\ e^- + M \qquad\qquad\qquad (2.16)$$

The main difficulties for using metal-based materials are their dramatic volume expansion

and contraction during Li insertion and extraction [104]. Serious agglomeration occurs for

these kinds of materials after one cycle [102]. Nano-sized materials have a high surface

energy, and they tend to form large agglomerates; however, in most cases, nanoparticles

do not merge together at room temperature because of the slow transport kinetics of the

host atoms and poor contact. During electrochemical lithiation, the particles are expanded,

which increases their contact probability[104, 105]. This leads to the pulverization of the

electrode materials, resulting in poor cycling performance.

Various approaches have been reported to enhance the cycling stability of transition

metals. These include (1) decreasing the active material's particle size [106, 107], (2)

dispersing the active material into an inactive/active buffer matrix [108, 109], (3) synthesizing

porous active materials [110], (4) using amorphous active materials [106, 111], and (5) forming

composites with conductive carbon [108] or polymer [112].

For instance, silicon materials has been intensively investigated by many groups since

silicon has both the highest gravimetric capacity (4200 mAh g^{-1}, $Li_{22}Si_5$) and the highest

volumetric capacity (9786 mAh cm^{-3}) among the anode material candidates[113]. It has been

confirmed that the high specific capacity value is due to the formation of intermetallic Li-

Si binary compounds. Nevertheless, the large volume modification (~ 400 %) during the

charge/discharge process causes poor cycling life and irreversible capacity. Secondly, the

formation of Si compounds at the solid electrolyte interface inhibits the alloying/de-alloying processes. In order to understand the exact reason for the poor cycling stability of Si as anode in LIBs, many in-situ investigations with different experimental techniques such as XRD, NMR, and TEM have been performed[114-116]. These studies demonstrated that the electrical contact between the active material and both the conductive carbon and the current collector are reduced due to the large volume expansion/contraction of the Si anode, leading to irreversibility in the lithium insertion/extraction. Eventually, these volume changes result in shorter cycling life and capacity fading. Similar behaviour has also been observed in germanium nanoparticles, which have high lithium storage capability (1623 mAh g^{-1}) with $Li_{22}Ge_5$ as equivalent stoichiometry. The practical usage of Ge as active electrode in LIBs is also hindered by the dramatic volume changes (~ 300 %) during lithium insertion/deinsertion[117]. Ge nanostructures, such as nanoparticles[118], nanowires[119], and nanotubes[120] can effectively sustain the volume change with better efficiency than in bulk and microstructured materials. Noticeable, improvements have been observed with hybrid composites of Ge nanoparticles using conductive matrices, obtained through simple preparation routes. From example, Ge nanoparticles, with diameters between 5 nm and 20 nm, were encapsulated inside carbon nanospheres with diameters in the range from 50 to 70 nm[108]. The role of the carbon nanospheres is to act as structural buffer and electro-active materials during the lithium insertion and de-insertion process and to avoid direct contact with the electrolyte. This last aspect protects Ge from the formation of SEI. These composites exhibited high anode capacity of around 980 mAh g^{-1} vs. Li/Li$^+$ and 800 mAh g^{-1} with LiFePO$_4$ as cathode. Similarly, comparable high reversible capacities, along with excellent cycling life and high rate capability, were achieved by combining Ge nanoparticles with carbon nanotubes and reduced graphene oxide.

Recently there have been quite a few reports on conducting polymer-based composites for anode materials [121, 122], and there has been improvement in the properties achieved in Li-ion batteries through approaches such as buffering of volume changes, supporting the anode material and prevention of aggregation of particles, or by increasing electrical conductivity and prevention of direct contact of the active material with the electrolyte. Previous studies have shown that Sn-polypyrrole composite has improved capacity and cycle life compared with pure Sn, since the conductive polypyrrole in the composite could effectively buffer the volume changes during the lithium insertion/extraction processes [112, 123]. PPy also acts an efficient conductive addition to increase the conductivity of the electrode. For example, silicon/PPy shows much higher conductivity than bare silicon[124].

2.5.3 Transition Metal Oxides (TMO)

In 2000, Poizot et al. [125] reported for the first time that lithium can be stored reversible in transition metal oxides (TMO) through a heterogeneous conversion reaction:

$$Li + TMO \rightarrow Li_2O + TM \tag{2.17}$$
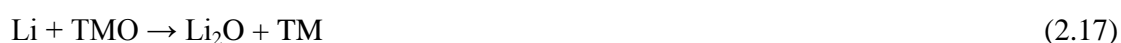
where TM is Co, Fe, Ni and Cu. Later, reversible lithium storage was also observed in transition metal (TM) fluorides, sulphides, nitrides, and phosphides[126-128]. This is very interesting in view of fundamental research findings that very inert LiF or Li_2O can react with a TM at room temperature [129]. It is clear now that the enhanced electrochemical reactivity of LiF or Li_2O is mainly a benefit of the special microstructure where the converted TMO components show an extremely small grain size (< 5 nm) and are uniformly interspersed with each other [130]. The very short diffusion lengths and large contact areas in nanocomposites are kinetically favourable for the unusually reversible electrochemical behaviours of TMO nanocomposites.

Interestingly, the elegant combination of two simple low-cost TMOs, or a TMO and a post-TMO, into spinel-like structures, can lead to the formation of mixed transition-metal oxides (MTMOs) (denoted as $A_xB_{3-x}O_4$; A, B = Co, Ni, Zn, Mn, Fe, etc.) with stoichiometric or even non-stoichiometric compositions. These spinel MTMOs have aroused widespread attention as appealing potential anode electrodes for next-generation LIBs due to their ease of large-scale synthesis, low cost, and remarkable electrochemical performance[131]. Their high electrochemical activity is owing to the complex chemical compositions, and their synergetic effects contribute to the exceptionally high specific capacity, which is typically 2-3 times higher than those of the graphite/carbon-based electrode materials[132]. More significantly, these MTMOs usually exhibit higher electrical conductivity than simple TMOs owing to the relatively low activation energy for electron transfer between cations[133, 134]. In the past decade, numerous spinel MTMOs with diverse nanostructures, including nanofibers[135], nanotubes[136, 137], nanowires[138, 139], nanorods[140], and nanoneedles[141], and have been applied as excellent electrode materials for high-performance LIBs.

In the past, iron oxides with impressive electrochemical properties have received an upsurge of interest owing to their fascinating and advantageous attributes, including low cost, environmental benignity, and high abundance. Nevertheless, when applied as anode materials, their higher oxidation potential, limited conductivity, and reaction kinetics restrict the battery output voltage and energy density[142, 143]. Furthermore, poor capacity retention also remains a major drawback, owing to the serious electrode pulverization related to the huge volumetric expansion/contraction during the charge/discharge process. Therefore, the spinel $MFeO_2$ series (M = Co^{144}, Ni^{144}, Cu^{145}, Mg^{146}, Ca^{147}, and Zn^{148}) have been extensively regarded as promising anodes for LIBs. It is highly anticipated that the existence of the other metal cation can effectively overcome the drawbacks of simple Fe-

based oxides, and deliver larger specific capacity, better cycling stability, and better rate performance by the careful selection of suitable combinations of different metal species. Among them, $ZnFe_2O_4$ stands out from the common ferrites as an attractive anode. Besides some common advantages such as low toxicity, easy synthesis, and low cost, $ZnFe_2O_4$ exhibits a relative low working voltage of about 1.5 V, which is much lower than that of Co-based anodes (2.1 V) [149] and Fe_2O_3 (1.74 V) [142]. Therefore an enhanced output voltage of the full cell is anticipated when coupled with a conventional cathode material. Furthermore, it is also interesting to note that $ZnFe_2O_4$ gives a high theoretical specific capacity of 1072 mA hg^{-1}, owing to the simultaneous implementation of both conversion and alloying reactions to reversibly store lithium. After the first report of nanocrystalline $ZnFe_2O_4$ used as anodes for LIBs[150], many endeavours have been devoted to further optimizing the performance of $ZnFe_2O_4$ with different structures and morphologies by various synthesis strategies, including the urea combustion method[148], octahedra synthesized by a one-step hydrothermal route[151], hollow microspheres synthesized by a hydrothermal reaction followed by annealing[152], etc. Recently, it has been reported the nickel-doping has positive effects for zinc ferrite in the terms of the Li-cycling behaviour[153]. In this doctoral work, we have reported the electrochemical performance of hollow or mesoporous structured $Zn_{0.5}Fe_{0.5}Ni_{0.5}O_4$ (NZFO) prepared by a one-step solvothermal method. The as-prepared mesoporous NZFO nanospheres showed excellent electrochemical performance with high initial discharge capacity and good capacity retention.

2.6 Electrolyte

2.6.1 Conventional electrolyte

Besides the electrodes, the electrolyte, which commonly refers to solution comprising salts and solvents, constitutes the third key component of a battery. About twenty years ago, alkyl carbonates were found to be the best and most suitable solvents for Li-ion batteries [154]. Fig. 2.14 shows several structural formulae for relevant alkyl carbonates. A major discovery was the selection of binary solvent mixtures such as ethylene carbonate (EC) and either dimethyl carbonate (DMC), ethyl methyl carbonate (EMC) or diethyl carbonate (DEC), used in conjunction with the Li salt, lithium hexafluorophosphate (LiPF$_6$), as the basic standard electrolyte solutions for Li-ion batteries [154, 155].
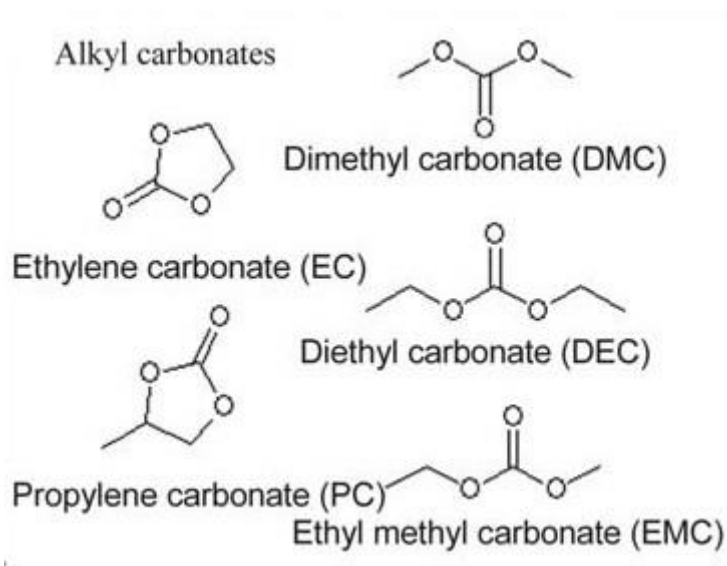
Figure 2.14 Family of alkyl carbonate solvents used in electrolyte in Li-ion batteries [6].

The common denominator of all the reaction products listed in Table 2.1 is that they precipitate on Li metal: non-active metals or carbon electrodes are polarized to low potential, and form thin surface films that block further electron transport when they reach a certain thickness, but they still allow Li-ion transport. Hence, a unique property of thin films of ionic Li compounds that are the main products of electro-reduction of non-aqueous Li salt solutions is that they behave as a solid electrolyte interphase (SEI) between the electrode and the solution [156]. This interphase may serve as a very effect

means of passivation for both Li and fully lithiated graphite, and thus enable their apparent stability in most Li salt solutions in nonaqueous polar aprotic solvents. The fact that most of the reduction processes of polar aprotic Li salt solutions, form passivating surface films that behave as SEI layers for Li ions, in what enables the selection of electrolyte solutions for LIBs to be focused on more problematic considerations, namely, the anodic stability of the electrolyte solutions. This point is very important because the limiting factor in Li-ion batteries in terms of voltage, specific capacity and energy is the cathode, the reversibility of which is critically dependent on the anodic stability of the electrolyte solution [157, 158].

Table 2.1 Major reduction products of nonaqueous Li salt solutions.

Solution species	Main reduction products	Potential range
O_2	LiO_2; Li_2O_2	1.5-2.0 V
H_2O	LiOH	1.5-1.2 V
HF, PF_5	LiF, Li_xPF_y	1.8 V and below
Ethers	ROLi	Below 0.5 V
Alkyl	$ROCO_2Li$, ROLi	Below 1.5 V
EC	$(CH_2OCO_2Li)_2$, C_2H_4,	Below 1.5 V
PC	$CH_3CH=CH_2$, $CH_3CH(OCO_2Li)CH_2OCO_2Li$	Below 0.5 V
DMC	CH_3OCO_2Li, CH_3OLi	Below 1.2 V
$LiClO_4$	LiCl, $LiClO_x$	Below 1.0 V

LiPF$_6$	LiF, Li$_x$PF$_y$	Below 1.0 V
LiN	LiF, LiCF$_3$, LiSO$_2$CF$_3$	Below 1.0 V

In all LiPF$_6$ solutions, there is some degree of decomposition of the salt to LiF and PF$_5$, which may be marked at elevated temperatures [159]. PF$_5$ is a strong Lewis acid that may be reduce at relatively high potentials (> 1.5 V vs. Li$^+$). Its involvement in surface reactions on the anode side may be detrimental to the anode's passivation. PF$_5$ reacts with any protic moiety (e.g., with unavoidably present trace water) to form HF and PF$_3$O (the latter also being a strong Lewis acid). HF interacts detrimentally with LiMO$_2$ and LiMPO$_4$ cathode materials[160, 161]. Ion exchange between protons and transition metal cations leads to the dissolution of the cations. The precipitation of transition metal clusters on the anode side, by reduction of the cations leads to the dissolved in solutions. HF itself reacts with lithium alkoxide (ROLi) and lithium alkyl carbonate (ROCO$_2$Li) surface species to form LiF and alcohol (ROH) or carbonic acid ester (ROCO$_2$H). Such reactions also worsen the anodes' passivation[162].
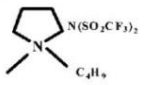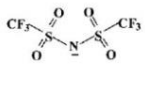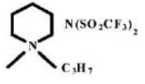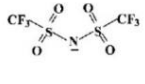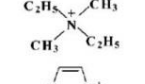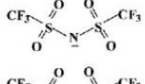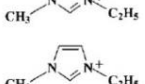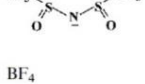
2.6.2 Ionic liquids (IL)

In recent years, highly interesting work on new electrolyte solutions for LIBs relates to ionic liquids (ILs), due to their thermal stability and non-flammability. In general there are several families of ionic liquids of interest that can be classified mostly via the cation. Several important families of relevant RTILs are listed, including their structural formulae and physical properties, in Table 2.2. Many papers have been published in recent years on the possible use of ILs in LIBs[163-165]. The limiting reactions of important

IL solutions on the anodic (cathode) and the cathodic (anode) sides of their electrochemical windows were thoroughly explored.

In general, the main advantages of ILs as solvents for LIBs are their wide electrochemical windows. Extension of the stability range of the Li^+ conducting electrolyte to above 4 V is necessary for practical application in LIBs. The electrochemical stability of liquid aprotic quaternary ammonium salts, determined usually at glassy carbon or platinum

Table 2.2 Important families of ionic liquids and their physical properties [6].

Cation	Anion	Melting point (°C)	Density/ g cm³ (20 °C)	Viscosity/ mPa s (25 °C)	Conductivity σ, 10⁻⁴ S cm⁻¹ (25 °C)
pyrrolidinium $N(SO_2CF_3)_2$, C_4H_9	$(CF_3SO_2)_2N$	−18	1.41	85	22
piperidinium $N(SO_2CF_3)_2$, C_3H_7	$(CF_3SO_2)_2N$	8.7	1.43	117	15.1
ammonium C_2H_5, CH_3, CH_3, C_2H_5	$(CF_3SO_2)_2N$	−14	1.41	83	12
imidazolium CH_3, C_2H_5	$(CF_3SO_2)_2N$	−15	1.52	34	87
imidazolium CH_3, C_2H_5	BF_4	13	1.28	37	140

electrodes, is within the wide range of 4-6 V[166]. Popular imidazolium salts show stability of ~ 4 V, while piperidinium and pyrrolidinium salts, especially based on imide anions, show stability at ~ 6 V. Symmetrical tetraalkylammonium cations (e.g. tetraethylammonium tetrafluoroborate) have been used for a long time as supporting electrolyte in organic solvents, due to their good stability. Asymmetric aliphatic tetraalkylammonium salts show lower melting points, and may be liquid at room temperature. Such ILs show very high electrochemical stability at the level of ~ 6 V[166]. Moreover, the cathodic stability limit is shifted to more negative potentials than that characteristic of the Li/Li$^+$ couple in this medium[167].

The main drawback of IL is high viscosity, which is much higher than that characteristic of water [$\eta(H_2O)$ = 0.89 cP at 25˚C]. Typically it is at the level of 30-50 cP, but in some cases it is much higher, even several hundreds of cP. After the addition of the [Li^+][X^-] salt to the neat ionic liquid [A^+][X^-], the viscosity of the resulting [Li^+]$_m$[A^+]$_n$[X^-]$_{m+n}$ system rather increases [104]. The high viscosity, characteristic of ionic liquids, causes some difficulties with their handling. Battery electrodes consist of active material mixed with an electron conductor (acetylene black) and a polymer (binder). The volume between particles should be filled with the electrolyte. In the case of viscous electrolytes and thick, quasi-three-dimensional electrodes this may be difficult. The relatively low capacity of the LiCoO$_2$ cathode (100 mA g^{-1}), working together with 1,2-diethyl-3,4-dimethylimidazolium imide, was explained as a consequence of a poor impregnation of the electrode by the viscous electrolyte[168]. A similar effect has been observed in the case of LiFePO$_4$ cathode: the coulombic efficiency of the system depends on the manner of electrode preparation. If the electrode was soaked with the ionic liquid electrolyte under vacuum for 8 h at 60 ˚C, the coulombic efficiency was higher in comparison to the same electrode filled with the same electrolyte but at ambient temperature and pressure[169].

The high viscosity may also lead to relatively low ionic conductivity. In general, the room temperature conductivity of aprotic ILs is within a broad range of 0.1-18 mS cm^{-1}. Conductivity at the level of 10 mS cm^{-1} is typical of ionic liquids based on the [EtMeIm$^+$] cation (14 mS cm^{-1} for [EtMeIm$^+$][BF^{4-}]), similar to that characteristic for classical electrolytes based on lithium salt solutions in mixtures of cyclic carbonates[170]. ILs based on such cations as pyrrolidinium or piperidinium show lower conductivities, however, at the level of 1-2 mS cm^{-1}. The dissolution of the [Li^+][X^-] salt in the [A^+][X^-] ionic liquid leads to a ternary system [Li^+]$_m$[A^+]$_n$[X^-]$_{(m+n)}$ with increased viscosity, thus leading to lower conductivity[170]. For example, it has been shown that the conductivity of the

[Li$^+$][BuEtPyrrol$^+$][NTf^{2-}] ternary ionic liquid exhibited lower conductivity in comparison to the neat [BuEtPyrrol$^+$][NTf^{2-}] ionic liquid. The conductivity of the solution decreased almost linearly with increasing LiNTf$_2$ concentration[171].

In this study, the room temperature ionic liquid (1 M LiNTf$_2$ in C$_4$mpyrNTf$_2$) was used as a new electrolyte for Li/LiNi$_{0.5}$Mn$_{1.5}$O$_4$ cells, and the cut-off voltages reached up to 5.1 V. The electrochemical performance revealed that, at such high voltage, the cells using the IL as electrolyte can deliver comparable discharge capacity to that with conventional electrolyte (1 M LiPF$_6$ in EC: DEC = 1:2 (v/v)), as well as significantly improved coulombic efficiency.

Chapter 3   EXPERIMENTAL METHODS

3.1 List of Materials

The list of materials and chemicals used during my study for the synthesis and characterization of materials is summarized in Table 3.1.

Table 3.1 Description of chemicals and materials used in this study

Materials/chemicals	Chemical formula	Purity (%)	Supplier
Acetone	CH_3COCH_3	≥ 99.5	Sigma-Aldrich
Ammonia solution	NH_3	28-30	Merck
Ammonium bicarbonate	NH_4HCO_3	>99.5	Sigma-Aldrich
Ammonium persulfate	$(NH_4)_2S_2O_8$	>98	Sigma-Aldrich
Aniline	$C_6H_5NH_2$	>99.5	Sigma-Aldrich
Argon gas	Ar	-	-
Carbon black	C		Timcal, Belgium
Cyclohexane	C_6H_{12}	99.5	Sigma-Aldrich
Diethyl carbonate	$C_5H_{10}O_3$	99	Sigma-Aldrich
Ethanol	C_2H_5O	Reagent	Q-Store Australia
Ethylene carbonate	$C_3H_4O_3$	99	Sigma-Aldrich
Ethylene glycol	$HOCH_2CH_2OH$	99.8	Sigma-Aldrich
Hydrochloric acid	HCl	37	Sigma-Aldrich
Iron (III) chloride	$FeCl_3$	97	Sigma-Aldrich

Iron (III) nitrate nonahydrate	$Fe(NO_3)_3 \cdot 9H_2O$	98	Sigma-Aldrich
Lithium hexafluorophosphate	$LiPF_6$	99.99	Aldrich
Lithium hydroxide monohydrate	$LiOH \cdot H_2O$	98	Aldrich
Lithium nitrate	$LiNO_3$	≥ 95	Sigma-Alrich
Lithium metal	Li	99.9	China
LP30 electrolyte	$LiPF_6$ in EC: DMC (1:1 by volume)	-	MERCK.KgaA, Germany
Manganese (II) acetate tetrahydrate	$Mn(CH_3COO_2) \cdot 4H_2O$	99	Sigma-Aldrich
Manganese sulphate monohydrate	$MnSO_4 \cdot H_2O$	98	Sigma-Aldrich
n-butanol	$CH_3(CH_2)_3OH$	99.0	Sigma-Aldrich
Nickel (II) acetate tetrahydrate	$Ni(CH_3COO_2) \cdot 4H_2O$	98	Aldrich
Nickel (II) nitrate hexhydrate	$Ni(NO_3)_2 \cdot 6H_2O$	98.5	Sigma-Aldrich
N-methyl-2-pyrrolidinone	C_5H_9NO	99.5	Sigma-Aldrich
Poly(vinylidene fluoride)	$(CH_2CF_2)_n$	-	Sigma-Aldrich
Polypropylene separator	$(C_3H_6)_n$	Celgard 2500	Hoechst Celanese Corporation, USA
Polyvinylpyrrolidone	$(C_6H_9NO)_n$	-	Sigma-Aldrich

Pyrrole	C_4H_5N	98	Sigma-Aldrich
Sodium borohydride	$NaBH_4$	>99	Fluka
Sodium carboxymethyl cellulose	-	-	Sigma-Aldrich
Sodium dodecyl benzene sulfonate	$C_{18}H_{29}NaO_3S$	> 98	Sigma-Aldrich
Sodium hydroxide	NaOH	≥ 98	Sigma-Aldrich
Sodium p-toluenesulfonate	$CH_3C_6H_4SO_3Na$	95	Aldrich
Vanadium pentoxide	V_2O_5	Puriss	Riedel-de Haen
Zinc nitrate hexahydrate	$Zn(NO_3)_2 \cdot 6H_2O$	98	Sigma-Aldrich

3.2 Experiment procedures

The experiments in this thesis can be classified into three broad categories, including synthesizing of material (anode, cathode, and room temperature ionic liquid electrolyte), structural and physical characterizations, and fabrication and electrochemical characterisations. Figure 3.1 shows the overall framework of the experiments.
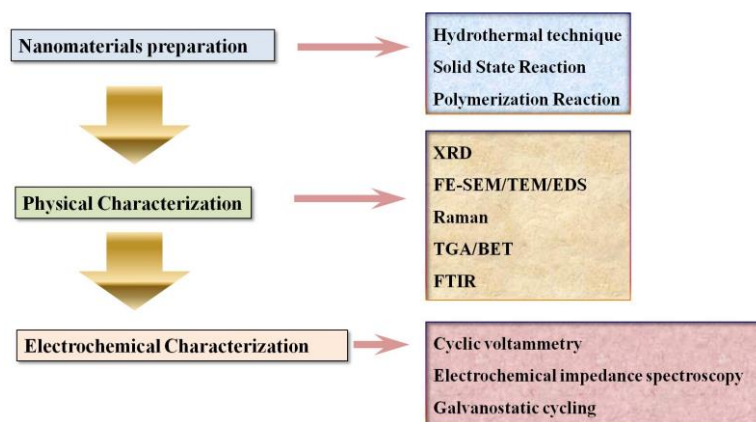
Figure 3.1 The overall framework of the experiment.

3.3 Materials preparation

3.3.1 Hydrothermal synthesis

Hydrothermal synthesis includes the various techniques of crystallizing substances from high-temperature aqueous solutions at high vapour pressures. Hydrothermal synthesis can be defined as a method of synthesis of single crystals that depends on the solubility of minerals in hot water under high pressure. The crystal growth is performed in apparatus consisting of a steel pressure vessel called an autoclave, in which a nutrient is supplied along with water. A temperature gradient is maintained between the opposite ends of the growth chamber. At the hotter end the nutrient solute dissolves, while at the cooler end it is deposited on a seed crystal, growing the desired crystal.

In this thesis, the 4748 Acid Digestion Bomb autoclave from Parr Instruments was used. It contains a 125 mL Teflon cup in a stainless steel body with six cap screws in the screw cap to seal the flanged Teflon cup (Fig. 3.2). An expandable wave spring maintains continuous pressure on the seal during the cooling cycle when the Teflon parts might otherwise relax and leak. The synthesis reactions can be carried out at temperatures below 250 C and pressures less than 1900 psi. In a typical experiment, the precursor solution is transferred to the Teflon cup, filling up to 80 % of the whole volume, and the autoclave is then kept in an oven for the pre-set temperature and time. The resultant product is filtered, washed, and centrifuged to remove the remaining ions.

3.3.2 Solvothermal synthesis

Solvothermal synthesis is a method of producing chemical compounds. It is very similar

47
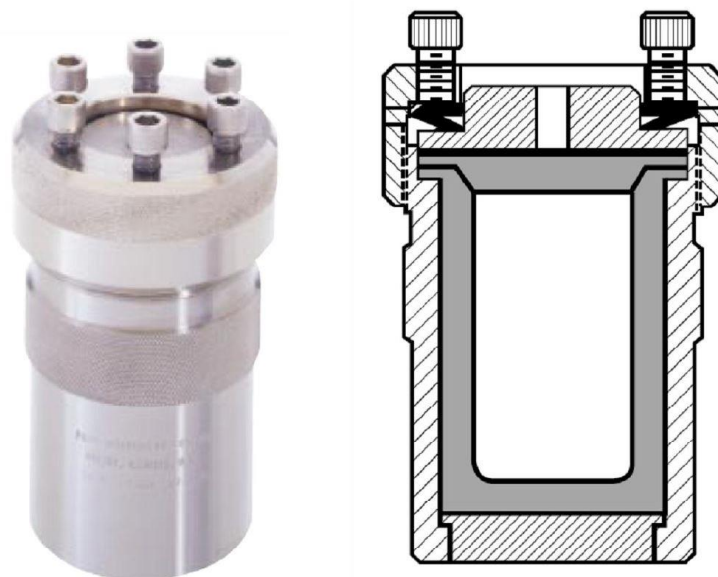
Figure 3.2 Schematic diagram of 4748 Acid Digestion Bomb from Parr Instruments.

to the hydrothermal route (where the synthesis is conducted in a stainless steel autoclave), the only different being that the precursor solution is usually not aqueous. The solvothermal synthesis allows for the precise control over the size, shape distribution, and crystallinity of metal oxide nanoparticles or nanostructures. These characteristics can be altered by changing certain experimental parameters, including reaction temperature, reaction time, solvent type, surfactant type, and precursor type.

3.3.3 Solid State Reaction

The solid-state reaction route is the most widely used method for the preparation of polycrystalline solids from a mixture of solid starting materials. Solids do not react together at room temperature over normal time scales and it is necessary to heat them to much higher temperatures, often to 500 ˚C to 1500 ˚C in order for reaction to occur at an appreciable rate. The factors on which the feasibility and rate of a solid state reaction depend include reaction conditions, structural properties of the reactants, surface area of

the solids, their reactivity and the thermodynamic free energy change associated with the reaction. The limiting factor for solid state reaction is the solid diffusion, governed by Fick's Law:

$$J = -D \left(\frac{dc}{dx}\right) \tag{3.1}$$

Where J is the flux of diffusing species, D is the diffusion coefficient, and dc/dx is the concentration gradient. D increases with temperature. Because of the low diffusion in solids, high treatment temperature and long heating time are always required for solid state reactions. In order to facilitate diffusion, the powder is usually pressed into pellets at high pressure before sintering. For some reactions, grinding, pressing and sintering may need to be repeated several times to obtain pure products.

3.3.4 Polymerization Reaction

Polymerization is a process of reacting monomer molecules together in a chemical reaction to form polymer chains or three-dimensional networks. In general, polymers such as polyvinyl chloride are referred to as "homopolymers", as they consist of repeated long chains or structure of the same monomer unit (Eq. 3.2), whereas polymers that consist of more than one molecule are referred to as copolymers (Eq. 3.3).

Homopolymers: $A + A + A... \rightarrow AAA...$ (3.2)

Copolymers: $A + B + A... \rightarrow ABA$ (3.3)

There are two basic ways to form polymers: (a) linking small molecules together, such as polyethylene, and (b) combining two molecules (of the same or different type) with the elimination of a stable small molecule such as water. This latter type of polymerization combines addition and elimination reactions and is called a condensation reaction.

In chemical compounds, polymerization occurs via a variety of reaction mechanisms that vary in complexity due to the functional groups present in reacting compounds and their inherent steric effects [172]. In more straightforward polymerization, alkenes, which are relatively stable due to σ bonding between carbon atoms, form polymers through relatively simple radical reactions; in contrast, more complex reactions such as those that involve substitution at the carbonyl group, require more complex synthesis due to the way in which reacting molecules polymerize [173].

3.4. Techniques for structural and physical characterization

The techniques for characterization of the as-prepared materials will be introduced in detail in the following sections.

3.4.1 X-Ray diffraction (XRD)

X-ray diffraction (XRD) is a non-destructive analytical method for identifying the atomic and molecular structure of a crystal, in which the crystalline atoms cause a beam of incident X-rays to diffract into many specific directions. In general, crystals are regular arrays of atoms, and X-rays can be considered waves of electromagnetic radiation. Atoms scatter X-ray waves, primarily through the atoms' electrons. Just as an ocean wave striking a lighthouse produces secondary circular waves emanating from the lighthouse, so an X-ray striking an electron produces secondary spherical waves emanating from the electron. This phenomenon is known as elastic scattering, and the electron (or lighthouse) is known as the scatterer. A regular array of scatterers produces a regular array of spherical waves. Although these waves cancel one another out in most directions through

destructive interference, they add constructively in a few specific directions, as determined by Bragg's law:

$$2d \sin \theta = n\lambda \tag{3.4}$$

Here d is the spacing between diffracting planes, θ is the incident angle, n is any integer, and λ is the wavelength of the beam. These specific directions appear as spots on the diffraction pattern called reflections. Thus, X-ray diffraction results from an electromagnetic wave (the X-ray) impinging on a regular array of scatterers (the repeating arrangement of atoms within the crystal).

The crystal size also can be calculated from the broadening of the peaks according to the Scherrer equation:

$$L = \frac{0.9\,\lambda}{B \cos \theta} \tag{3.5}$$

Where L is crystallite size, λ is 1.5418 Å and B is the peak full-width at half maximum (FWHM) in radians.

In this work, XRD was performed with a generator and diffractometer using Cu Kα radiation and a graphite monochromator. The systems were interfaced with Visual XRD and Traces software for graphical processing and data manipulations. Samples in powder form were dropped with ethanol onto clean glass slides and left to dry. The glass slide was then placed in the sample holder of the diffractometer and directly scanned at 2θ angles between 5° and 90° at a scan rate of 2° min^{-1}.

3.4.2 Scanning electron microscopy (SEM) or field-mission scanning electron microscopy (FESEM) with energy dispersive spectroscopy (EDS)

The scanning electron microscope (SEM) is a type of electron microscope that produces

images of a sample by scanning it with a focused beam of electrons. The electrons interact with atoms in the sample, producing various signals that can be detected and that contain information about the sample's surface topography and composition. The electron beam is generally scanned in a raster scan pattern, and the beam's position is combined with the detected signal to produce an image. SEM can achieve resolution better than 1 nanometer.

Further high magnification images could be obtained using a field-emission scanning electron microscope (FESEM). In the common or standard detection mode, through secondary electron imaging, the FESEM can produce very high-resolution images of a sample surface, revealing details less than 1 nm in size. Energy dispersive spectroscopy (EDS) is an accompanying elemental analysis technique that detects atomic numbers 6 through 92 with a detectability limit of approximately 0.1 weight percent. The analysis diameter and depth for EDS is typically a few micrometers. Images obtained in backscatter electron mode offer quick identification of areas with different atomic number. EDS mapping illustrates the distribution of species in the near-surface region.

3.4.3 Transmission electron microscopy (TEM)

The transmission electron microscope (TEM) operates on the same basic principles as the SEM and FESEM. The electron source emits electrons that travel through vacuum in the column of the microscope. In TEM technique, a beam of electrons is transmitted through an ultra-thin specimen, interacting with the specimen as it passes through. An image is formed from the interaction of the electrons transmitted through the specimen; the image is magnified and focused onto an imaging device, such as a

fluorescent screen or a layer of photographic film, or to be detected by a sensor such as a charge-coupled device camera.

TEMs are capable of imaging at a significantly higher resolution than light microscopes, owing to the small de Broglie wavelength of electrons. This enables the instrument's user to examine fine detail, even as small as a single column of atoms, which is thousands of times smaller than the smallest resolvable object in a light microscope. It is also capable of forming a focused electron probe, as small as 20 Å, which can be positioned on very fine features in the sample for diffraction information or analysis of X-rays for compositional information. The darker areas represent areas where fewer electrons have passed through as a result of higher specimen density.

3.4.4 Thermogravimetric analysis (TGA)

Thermogravimetric analysis (TGA) is a method of thermal analysis in which changes in the physical and chemical properties of materials are detected as a function of increasing temperature, or as a function of time. Generally, it measures the amount and rate of change in the mass of a sample as a function of temperature or time in a controlled atmosphere. In this doctoral work, a Mettler-Toledo thermogravimeteric analysis Star[e] System was used to determine the amount of polypyrrole and polyaniline in the composite samples.

3.4.5 Raman spectroscopy

Raman spectroscopy is a spectroscopic technique used to observe vibrational, rotational, and other low-frequency modes in a system. It relies on inelastic scattering, or Raman scattering, of monochomatic light, usually from a laser in the visible, near infrared, or near ultraviolet range. The laser light interacts with molecular vibrations, phonons, or other excitations in the system, resulting in the energy of the laser photons being shifted up or down. These shifts provide information about vibrational, rotational, and other low frequency transitions in molecules. Herein, Raman spectra of the samples were collected using a JOBIN YVON HR800 Confocal Raman system from HORIBA Ltd., France with 632.8 nm diode laser excitation on a 300 line mm^{-1} grating at room temperature.

3.4.6 Brunauer-Emmett-Teller (BET) measurement

The well-known Brunauer-Emmett-Teller (BET) theory explains the physical adsorption of gas molecules on a solid surface, and serves as the basis for an important analysis technique for the measurement of the specific surface area of a material. The adsorption is based on the following hypotheses: (1) gas molecules are physically adsorbed on a solid in an unlimited number of layers; (2) there is no interaction between each adsorption layer; and (3) the Langmuir theory can be applied to each layer. The resulting BET equation is,

$$\frac{1}{\left[V\left(\frac{P_0}{P}-1\right)\right]} = \frac{C-1}{V_m C} \times \frac{P}{P_0} + \frac{1}{V_m C} \tag{3.6}$$

, where P and P_0 are the equilibrium and saturation pressures of adsorbents at the temperature of adsorption, respective, V is the adsorbed gas quantity, and V_m is the monolayer adsorbed gas quantity. C is the BET constant.

In this study, the BET measurements were conducted on a Quantachrome Nova 1000 nitrogen gas analyser, and Autosorb-iQ-Cx nitrogen adsorption instrument to determine the specific surface area of the synthesized powders.

3.5 Electrode preparation and coin-cell assembly

The electrodes of LIBs were made by dispersing a mixture of 80 wt. % active materials, 10 wt. % carbon black and 10 wt. % polyvinylidene fluoride (PVDF)/ carboxymethyl cellulose (CMC) binder in N-methyl-2-pyrrolidone (NMP)/ deionised water to obtain slurry. The slurry was spread on to aluminium foil (for cathode materials) or copper foil (for anode materials). The electrode were then dried and pressed under a pressure of 300 kg cm^{-2}. The electrodes was then dried in a vacuum furnace for 12 hours and then finally transferred to a glove box. The electrode area was approximately 1.0 cm^2, and the typical thickness of the electrode was about 100 μm. The mass loading of the active material within the electrode was about 1 mg cm^{-1}.

The test cells were assembled in an argon-filled glove box (Unilab, Mbraun, USA), in which moisture and oxygen were automatically controlled to be less than 5 ppm. In order to examine the electrochemical properties of the prepared electrode materials, lithium metal was used as a standard counter electrode in all test cells. The electrolyte was 1 M LiPF$_6$ in solution of ethylene carbonate (EC) and dimethyl carbonate (DMC) / diethyl carbonate (DEC). The separator was Celgard 2500 porous plastic film, and the test cell is standard CR2032.

3.6 Electrochemical measurements

3.6.1 Galvanostatic charge-discharge

The discharge/charge capacity and cycling performance of the materials were investigated in constant current density mode. The charge/discharge (Q) equals the total electron charge in each process and can be calculated from the recording current and the time $Q = I \times t$. The coin cells were tested on Land CT2001A battery testers.

3.6.2 Cyclic voltammetry

Cyclic voltammetry (CV) is type of potentiodynamic electrochemical measurement to investigate the thermodynamics and kinetics of electron transfer in an electrochemical reaction in the working electrode. In a cyclic voltammetry experiment, the working electrode potential is ramped linearly versus time as in linear sweep voltammetry. Cyclic voltammetry takes the experiment a step further than linear sweep voltammetry, which ends when it reaches a set potential. When cyclic voltammetry reaches a set potential, the working electrode's potential ramp is inverted. This inversion can take place multiple times during a single experiment. The current at the working electrode is plotted versus the applied voltage to give the cyclic voltammograms trace. Cyclic voltammetry is generally used to study the electrochemical properties of an analyte in solution.

3.6.3 Electrochemical impedance spectroscopy

Electrochemical impedance spectroscopy (EIS) is well known as an experimental method for characterizing electrochemical systems. It measures the impedance of a system over a

range of frequencies, and therefore the frequency response of the system, including the energy storage and dissipation properties, is revealed.

EIS can be performed in potentiostatic or galvanostatic mode. In potentiostatic mode, impedance measurements are conducted by applying a sine wave around a potential E that can be set to a fixed value or a value that is relative to the working electrode equilibrium potential over a range of frequencies. A typical impedance spectrum consists of a low frequency semicircle resulting from the kinetic processes and a high frequency tail corresponding to the diffusion processes. The galvanostatic technique is very similar to potentiostatic mode, except that the current is controlled instead of the potential.

Chapter 4   Germanium/Polypyrrole Composite

for high power Lithium-ion batteries

4.1 Introduction

Rechargeable LIBs are currently leading candidates for powering electric vehicles and portable electronic devices. Although such batteries have gained commercial success, their capacity is still limited by the amount of lithium that can be stored in the anode (graphite) and cathode ($LiCoO_2$) electrodes, which have theoretical lithium-ion storage capacities of 372 mAh g^{-1} and 137 mAh g^{-1}, respectively [174, 175]. Therefore, intensive research efforts are continuing in the search for battery electrode materials with higher energy densities, long cycle life, and high reversible capacity [176]. Recently, as an alternative to the traditional graphitic anode materials, the Group IV metals (Sn, Ge, Si) have been considered as ideal candidate anode materials for reversible lithium energy storage due to their significantly higher lithium-ion storage capacities [177-179]. In 2005, Sony released a new LIB system, which used Sn-Co-C composite as its anode material. This further accelerated the interest in anode electrodes made from metal or alloy.

Among these Group IV metals, germanium, with high theoretical capacity (1600 mAh g^{-1} compared with 372 mAh g^{-1} for graphite), good lithium diffusivity (400 times faster than in silicon), and high electrical conductivity (104 times higher than silicon), has been proved to be one of the most attractive potential anode materials for LIBs. Consequently, many researchers have tried to fabricate Ge nanoparticles for battery application[180, 181]. It has been widely recognized that reduction of the Ge particle size could enhance the

electrochemical activity of Ge due to its shorter electron paths and larger reaction surface. Unfortunately, similarly to silicon[177] and tin[182], nanosized Ge particles always aggregate severely and merge into micron-sized particles during Li-ion insertion/extraction processes. This aggregation will lead to severe pulverization and delamination on the surface of the electrode, and a rapid decline in the electrochemical capacity[183, 184]. Up to now, various strategies have been devised in attempts to overcome this issue. In general, this aggregation can be partially hindered by mixing the Ge with a large amount of carbon-based materials, such as carbon black [178, 185], carbon nanotubes [186, 187], and graphene[188, 189].

Recently, conductive polypyrrole (PPy) has attracted much attention as another effective additive material to improve the performance of anode materials in LIBs [112, 124, 190]. A series of anode materials, including SnO_2-PPy [191], Sn-PPy [112], Si-PPy [124, 192], C-PPy [193], and TiO_2-PPy [194, 195], have been synthesised and shown enhanced electrical performance in the LIB system. Conductive PPy can effectively buffer the volume changes during the cycling process and increase the conductivity of the active materials[79, 196, 197]. Meanwhile, the PPy also can connect isolated particles, acting as an efficient host matrix to prevent cracking and pulverization on the surface of electrodes[55, 112, 197, 198]. To the best of our knowledge, however, there have been no reports to date on the synthesis of germanium-conducting polymer composite for application as anode in LIBs. In this paper, we have fabricated amorphous nanostructured Ge particles on the surface of PPy through one simple reduction reaction in aqueous solution and investigated the electrochemical properties of the Ge-PPy composite as negative electrode material in the LIB.

4.2 Experimental

4.2.1 Preparation of materials

PPy powders were synthesised by chemical oxidation in an aqueous solution. 1 g pyrrole monomer and 0.96 g sodium p-toluenesulfonate (*pTS* Na) were dispersed in distilled water. Then an oxidizing agent iron chloride ($FeCl_3$) aqueous solution was added drop wise to initiate the polymerization. The PPy was achieved after stirring for 12 h, as indicated when the suspension became black. The products were obtained by filtering and washing with deionized water, and then drying them under vacuum at 60 ˚C for 12 h.

The Ge nanoparticles were prepared by a one-step aqueous reaction. 0.26 g GeO_2 and 0.01 g polyvinylpyrrolidone (PVP) were dissolved completely in 10 mL 0.15 M NaOH solution, and then the pH of the solution was adjusted to 7 with 0.5 M HCl. Then, aqueous $NaBH_4$ solution was added under strong magnetic stirring in a water bath at 60 ˚C. After 3 h, a dark brown suspension was formed, and then the resultant powders were obtained by centrifugation, washed with deionized water several times and dried in a vacuum for 12 h. For the preparation of Ge-PPy composite, the as-prepared PPy powders (50 mg) were dispersed in the solution before reaction.

4.2.2 Material characterization

X-ray diffraction (XRD) analysis was carried out using a GBC MMA generator and diffractometer with Cu Kα radiation and a graphite monochromator. Raman spectroscopy was conducted to characterize the as-prepared PPy and the PPy in the composite, using a JOBIN YVON HR800 Confocal Raman system with 632.8 nm diode laser excitation on

300 lines mm^{-1} grating at room temperature. Thermogravimetric analysis (TGA) was performed using a SETARAM analyzer (France) in air from 50 ℃ to 700 ℃ to determine the amount of PPy in the sample. The morphology and electrochemical properties of the samples were investigated using a JEOL 7500 field emission scanning electron microscope (SEM) with a JEOL energy dispersive spectroscopy (EDS) system. Transmission electron microscopy (TEM) was conducted on a JEOL2011 analytical instrument. The Raman characteristics of samples were investigated using a JOBIN YVON HR800 confocal Raman system with 632.8 nm laser diode excitation on 300 lines/mm grating at room temperature.

4.2.3 Electrochemical measurements

The electrodes were prepared using 80 wt. % active materials, 10 wt. % carbon black, and 10 wt. % sodium carboxymethyl cellulose (CMC) in distilled water to form homogeneous slurry. The slurry was spread onto pieces of copper foil. The coated electrodes were dried in a vacuum oven at 100 ℃ for 24 h, and then compressed at a rate of 300 kPa. The electrodes were assembled into CR 2032 coin-type cells in an Ar-filled glove box, using lithium metal as the counter electrode and 1 M LiPF$_6$ in ethylene carbonate/dimethyl carbonate (EC/DMC, 1/1 by volume) as the electrolyte. The cells were cycled between 1.50 V and 0.01 V at a constant current density of 320 mA g^{-1} (0.2 C) on a Land battery tester at 25 ℃. Different current rates, ranging from 160 mA g^{-1} (0.1 C) to 6400 mA g^{-1} (4.0 C), were also used to measure the electrochemical response. Electrochemical impedance spectroscopy (EIS) and cyclic voltammetry were carried out using a CHI 660B electrochemical workstation.

4.3 Results and discussion

4.3.1 Physicochemical characterization

X-ray diffraction (XRD) patterns obtained from the pristine nano-Ge and Ge-PPy are shown in Fig. 6.1(a). The two broad diffraction peaks obtained from the samples are readily indexed to diamond-like cubic Ge (JCPDS card No. 65-0333), which means that the samples present a disordered (amorphous) structure. This result is similar to those reported by Wu et al. for Ge nanoparticle synthesis [199]. The diffraction pattern of the Ge-PPy matches well with the pristine Ge, indicating the presence of Ge and that no impurity was introduced into the composite.

Fig 4.1(b) displays the in situ Raman spectra of the bare Ge, PPy and Ge-PPy composite, using laser excitation at 632.8 nm. The Raman peak of the Ge around 293 cm^{-1} in both the pristine material and the composite is asymmetric and has an extended tail at low frequencies, which means that the diameters of the Ge particles should be less than 28 nm [200]. The peaks of the bare PPy located between 800 cm^{-1} and 1700 cm^{-1} are in good agreement with the typical Raman modes of PPy [201]. In this range, the 988 cm^{-1} benzoid band indicates that certain sites of the PPy chain are in the reduced state, whereas the vibrational mode at 931 cm^{-1}, assigned to a C-H out-of-plane deformation of the quinoid form, is related to the oxidize sites [202]. For the intermediate phase in the as-prepared bare PPy, where different vibrational modes assigned to the reduced and the oxidised forms coexist, the polaron is the dominant species. After coating with Ge nanoparticles, the 932 cm^{-1} band remains sharp, while the intensity of the benzoid band at 986 cm^{-1} increases slightly. Simultaneously, the Raman spectrum of the Ge-PPy composite displays the low intensity of the benzoic bands of νC=C at 1531 cm^{-1}, and a significant sharp quinoid form

band of νC=C is observed at 1602 cm^{-1}, which is characteristic of the oxidized state of PPy [202, 203]. Even after stirring in NaBH$_4$ solution for 3 h, these spectral features indicate that most PPy chains are still at intermediary oxidation levels. Compared with the PPy in reduced state, oxidized PPy is considered as a more effective additive for the LIB, due to its electrical repulsion between positive charges present on neighbouring sites, which allows the opening of channels and the penetration of counter-ions [204].

For quantifying the amount of Ge in the composite, thermogravimetic analysis (TGA) was carried out in air. The samples were heated from 50°C to 700°C at a rate of 10 °C min^{-1}. Fig. 4.1(c) presents the TGA curve of the Ge-PPy composite along with that of pure PPy. As can be seen, the PPy content was totally burned out during the heating process, while the Ge in the composite was oxidized into GeO$_2$ with increasing temperature. The equation is presented below:

Ge+O$_2$ (heated to 700 °C) $\rightarrow$ GeO$_2$ (4.1)

So the final product is entirely converted to GeO$_2$, from which the content of Ge can be calculated. Through using this method, it was estimated that the amount of Ge in the Ge-PPy was about 69.0 wt. %.

The morphologies of the samples were characterized by scanning and transmission electron microscopy (SEM and TEM). The SEM image of the PPy (Fig. 4.2(a)) shows micrometer-sized particles consisting of ~200 nm PPy particles. Fig. 4.2(b) reveals that the pristine Ge particle size is extremely small and that these primary particles have clustered into large agglomerates. After coating with Ge nanoparticles, the particles become spherical, and the diameters are increased to about 400 nm (Fig. 4.2(c)). With a further increase in magnification, it can be clearly observed that the surfaces of the composite particles (Fig. 4.2(d)) have become rough and have some small particles

attached. These small particles could be Ge nanoparticles. Another important feature of the composite is that serious agglomeration of Ge nanoparticles is relieved, because the PPy can act as a barrier to reduce the gathering of Ge nanoparticles during the Ge-PPy synthesis.
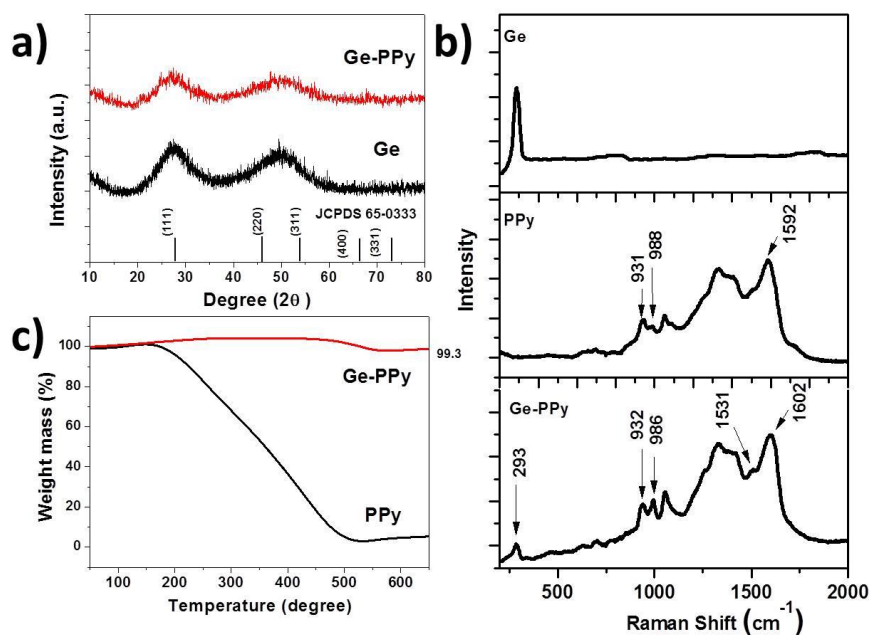
Figure 4.1 (a) XRD patterns obtained from the as-prepared Ge particles and Ge-PPy composite. (b) Raman spectra of PPy, Ge and Ge-PPy composite. (c) TGA curves of PPy and Ge-PPy.

To further investigate the distribution of the Ge in the particles, energy dispersive spectroscopy (EDS) mapping was performed, and the results are shown in Fig. 4.2(e). The element N is associated with PPy, and the bright regions indicate that the Ge and N are distributed uniformly throughout the sample, which means that the Ge nanoparticles have uniformly coated the surfaces of the PPy.

More highly magnified TEM images of the pristine Ge and Ge-PPy samples are shown in Fig. 4.3. TEM combined with selected area electron diffraction (SAED: Fig 4.3(a) and (c)

64
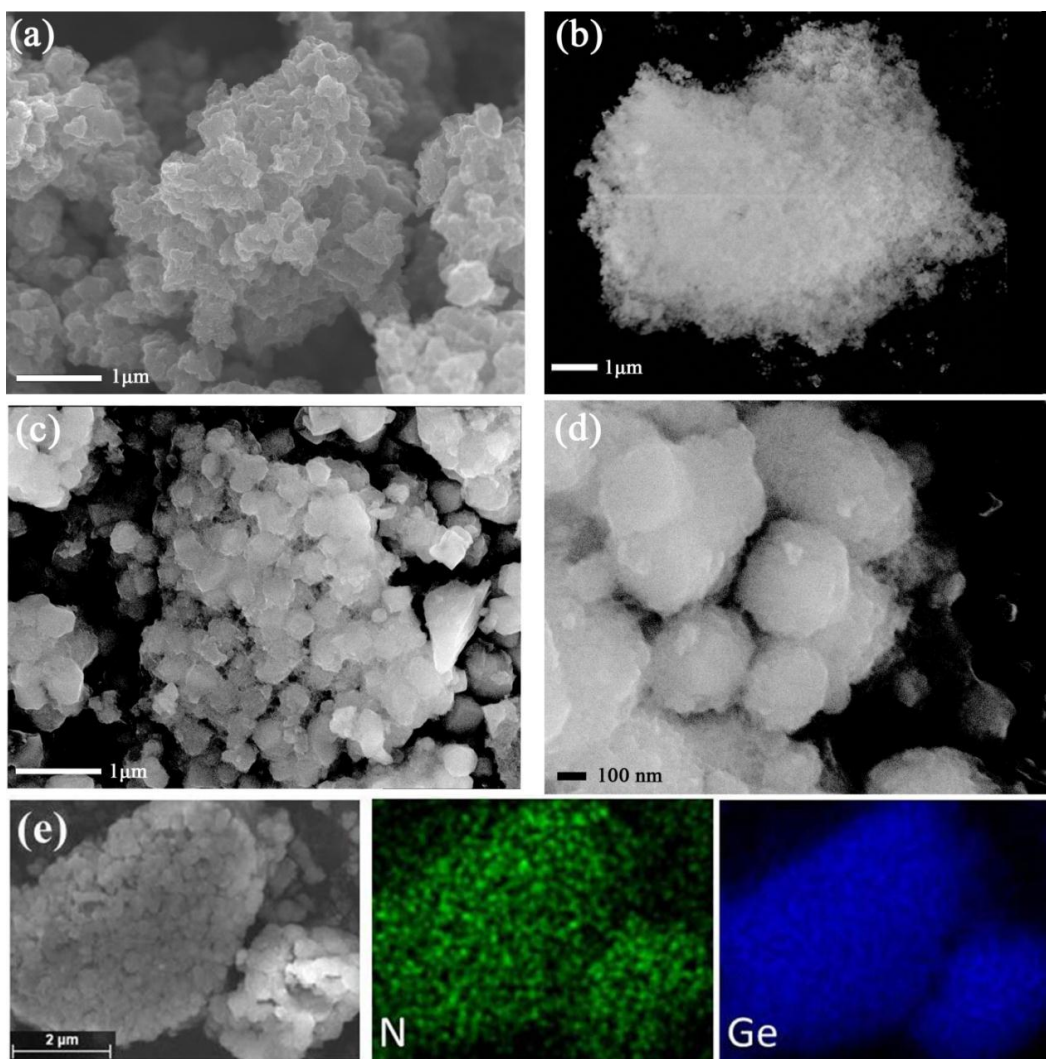
Figure 4.2 SEM images of (a) PPy, (b) Ge nanoparticle, (c, d) Ge-PPy composite, and (e) energy dispersive X-ray mapping of the Ge-PPy composite for the elements Ge and N.

inset images) confirmed that both the pristine nano-Ge and the Ge in the composite are, in fact, amorphous. Examination of the pristine amorphous Ge at high magnification (Fig 4.3b) indicates that the individual Ge particles are around 5-20 nm in diameter and have clustered into larger agglomerates, as is consistent with the SEM results. TEM examination also revealed that the PPy particles connect individual nanosized Ge particles in the Ge-PPy composite (Fig. 4.3c). A high resolution image of the edges of the PPy particles (Fig. 4.3d) demonstrates that the amorphous Ge nanoparticles completely

cover the individual PPy regions and form porous structure. Brunauer-Emmett-Teller (BET) gas adsorption/desorption demonstrated that the composite has much higher surface area compared to the bare Ge, which is 38.5 m^2g^{-1} and 25.8 m^2g^{-1} for the bare and Ge-PPy samples, respectively.
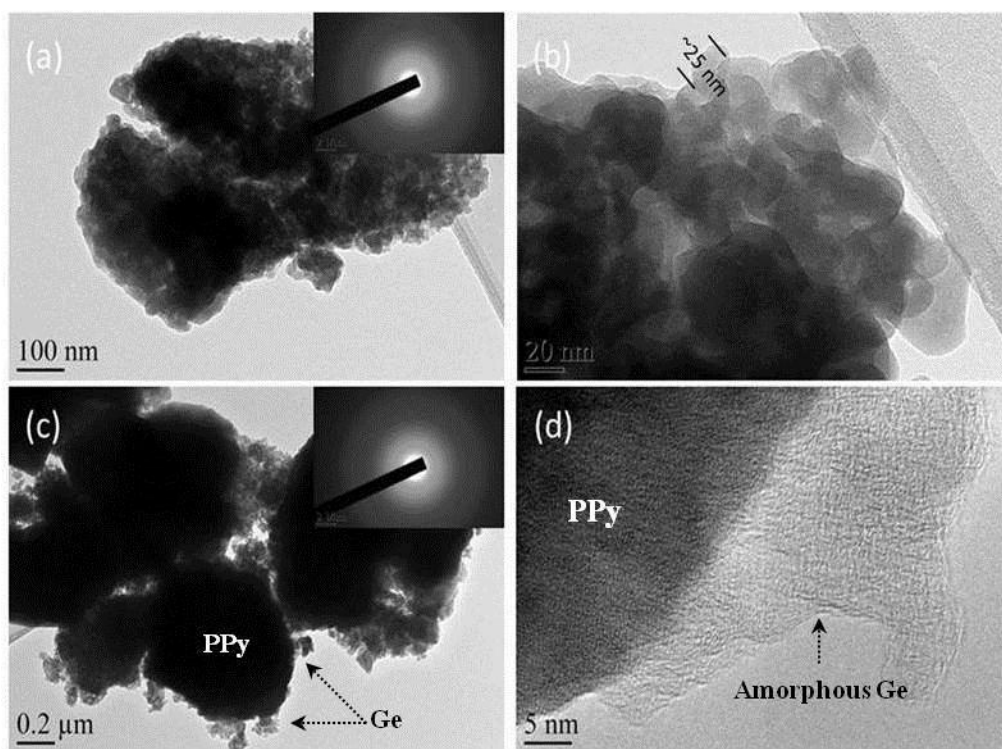
Figure 4.3 TEM images obtained from the pristine Ge (a, b) and the Ge-PPy composite (c, d). The insets in (a) and (c) are the corresponding SAED patterns.

4.3.2 Electrochemical properties

Galvanostatic discharge-charge testing between 0-1.5 V at 0.2 C was carried out to investigate the electrical reactivity of the samples. For the PPy electrode, the cell fails during the first discharge period. Therefore, we calculated the specific capacity based on the weight of Ge in the Ge/PPy composite separately to understand the performance of the Ge particles. The 1st, 2nd, and 50th cycle charge-discharge curves of the Ge-PPy that

were collected are shown in Fig. 4.4(a). The voltage profile and differential capacity data corresponding to the charge and discharge curves are also presented in Fig. 4.4(b). Several cathodic peaks can be observed in the cycling, which represent the stepwise lithium alloying reaction to form Li_xGe alloys. After 50 cycles, the cathodic peaks at 0.18 V and 0.32 V remain sharp and similar to those in the 2nd cycle, suggesting stability in the reversibility and kinetic activities for Li^+ insertion/extraction of the electrode made from Ge-PPy. To identify all the electrochemical reactions, the electrochemical response was also measured for the Ge-PPy composite by cyclic voltammetry at 0.1 mV s^{-1}. The typical cyclic voltammograms of the Ge-PPy nanocomposite for the 1st, 2nd and 5th cycles, which are shown in Fig. 4.4(c), are in accordance with previous reports for Ge electrode[180, 205]. The broad peaks at around 0.49 V and 0.32 V in the second cathodic curve can be attributed to the conversion from Ge to Li_9Ge_4. The small peak at 0.14 V is likely to be related to the formation of Li_7Ge_2. As the potential approaches 0 V, a big peak starts to appear, indicating the formation of $Li_{15}Ge_4$ and $Li_{22}Ge_5$. The whole discharge (lithiation) reaction can be expressed as a three-step process based on the following reactions:

$$Ge \rightarrow Li_9Ge_4 \rightarrow Li_7Ge_2 \rightarrow Li_{15}Ge_4 + Li_{22}Ge_5 \tag{4.2}$$

During Li-ion extraction from Li_xGe, only one single broad peak response around 0.46 V is observed, which agrees with what has been reported in the literature [180, 188]. In addition, no additional peaks are detected in the cyclic voltammetery curves of Ge-PPy. This confirms that the PPy is not involved in electrochemical reactions during Li-ion intercalation/deintercalation processes and is only providing paths for electrical conduction[54, 55, 198].

The battery performances of the samples were tested at various current densities. Initially, the galvanostatic discharge and charge capacities of pristine Ge and Ge-PPy were measured in the voltage range of 0.01-1.50 V with a current density of 320 mA g^{-1} (Fig.

4.5a) and their coulombic efficiencies are also presented in Fig. 4.5(b). The first discharge capacity of the pure Ge electrode was 1506 mAh g^{-1}, corresponding to an initial coulombic efficiency of 59.3 %. This particularly high irreversible discharge capacity mainly comes from the huge formation of solid electrolyte interphase (SEI) [18]. The nano-sized morphology of the particles also plays a significant role, with the utilization of small particles being enhanced by their larger surface area and shorter diffusion length for the lithium intercalation process[183], although the advantages of particle size do not for
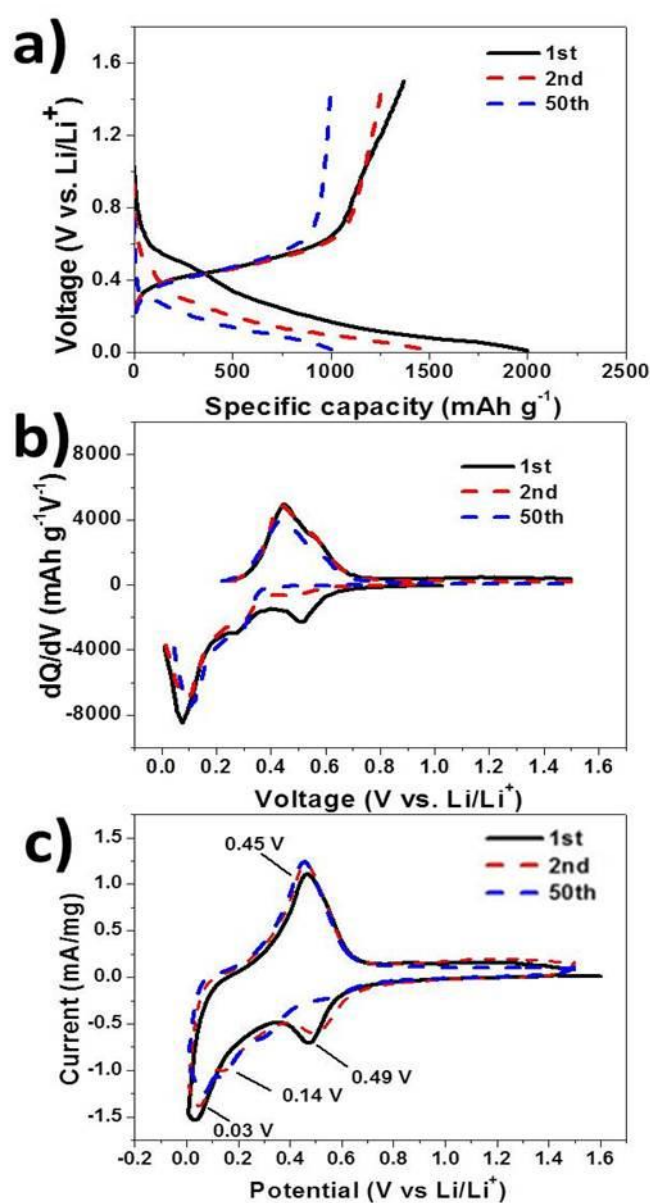
Figure 4.4 Charge-discharge curves of Ge-PPy composite for selected cycles (a), dQ/dV plots of Ge-PPy (b), and cyclic voltammograms of Ge-PPy (c); Scanning rate: 0.1 mV s^{-1}.

long periods of time. As mentioned above, nano-germanium particles would be likely to aggregate severely during the Li$^+$ insertion, thus leading to poor coulmbic efficiency in the first cycle. Furthermore, as the cycle number increases, the mechanical stresses induced by the volume changes would result in pulverization and delamination of the electrode structure, leading to low coulmbic efficiency and poor cycling life [181]. Therefore, the discharge capacity of pristine Ge decreases rapidly and continuously, declining to only 437 mAh g^{-1} over 50 cycles, which is only approximately 29 % of the initial capacity. On the other hand, it can be seen that the Ge-PPy composite electrode shows great enhancement of the capacity retention, based on both the composite and the calculated contribution of the pure Ge. The initial capacity of the Ge nanoparticle contribution calculated for the Ge-PPy composite electrode reaches up to 2024 mAh g^{-1}, with a relatively high coulombic efficiency of 68.6 %, and after 5 cycles, the coulombic efficiency retains a steady value between 89 and 99 %. The difference in the initial coulombic efficiency is mainly due to the PPy, which suppress solid electrolyte interphase (SEI) formation in the first cycle[180, 205]. Simultaneously, the Ge nanoparticles are electrical connected with the porous PPy so that more Ge nanoparticles will contribute to the capacity and the electronic transport can be enhanced. Thus, the discharge capacity of Ge in Ge-PPy composite is sustained at around 1029 mAh g^{-1} after 50 cycles at 0.2 C, corresponding to capacity retention of 50.8 %. These results demonstrate that the added PPy allows a greater utilization in capacity of the Ge nanoparticles and enhances the cycling performance. Compared to some carbon-supported Ge materials in previous reports, with capacities of around 600 mAh g^{-1} under similar testing conditions [188, 206], it can be speculated that the PPy plays a more important role in that enhanced

69

electrochemical activity, although its capacity contribution is negligible in negative electrode for the LIB.

A comparison of the performances at higher power rates for both samples (with and without PPy) is also presented in Fig 4.5(b). The electrode capacities were measured after 5 cycles at various current densities of 0.1 C, 0.5 C, 1 C, 2 C, and 4 C (1 C=1600 mA g^{-1}) in an ascending order, and back to 0.2 C in 35 cycles. The discharge capacities calculated for the Ge nanoparticles in the composite were measured to be 1420 mAh g^{-1} at 0.5 C, 1300 mAh g^{-1} at 1 C, 865 mAh g^{-1} at 2 C, and 406 mAh g^{-1} at 4 C. When the cycling rate was returned back to 0.1 C after 30 cycles at different rates, the composite electrode still could deliver 1360 mAh g^{-1}. In contrast, strikingly poor high-rate capability is observed for the pristine Ge electrode. It should be pointed out that the rate capability of Ge-PPy is still not as good as for some Ge-based materials recently reported, such as Ge-carbon nanocomposite with 600 mAh g^{-1} at 40 C [178], or Ge thin film electrode with 800 mAh g^{-1} at 1000 C [180]. Nevertheless, the enhanced high-rate performance is comparable to the most research on Ge electrodes combined with graphene [188], mesocarbon microbeads [206], or other carbonaceous materials [207].
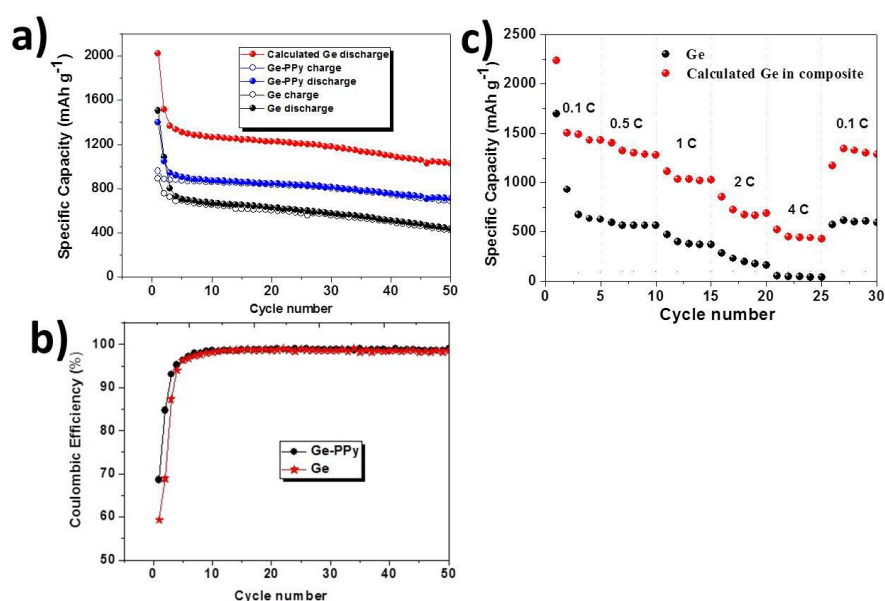
Figure 4.5 (a) Discharge capacity and charge capacity of Ge and Ge-PPy composite electrodes at 320mA g^{-1} (0.2 C). (b) Coulombic efficiency of Ge and Ge-PPy composite electrodes at 320mA g^{-1}. (c) Rate capability of Ge and Ge-PPy composite at various current densities between 0.01 V and 1.50 V vs. Li/Li^{+}.

In order to further verify that the PPy is responsible for the good conductivity of the cells with the Ge-PPy electrodes, electrochemical impedance measurements were conducted on working electrodes in the fully discharged state. The Nyquist plots obtained for the pure Ge and Ge-PPy before and after 50 cycles were compared and are presented in Fig. 4.6 (A). It is found that the cells present one small semicircle before cycling, and the impedance is 23 Ω and 49 Ω for Ge-PPy composite and pristine Ge, respectively. In addition, two compressed semicircles are shown in the enlarged high-frequency impedance curves after cycling (Fig. 4.6(B)), indicating increased impedances. The high-frequency intercept of the high frequency semicircle reflects the uncompensated resistance, R$_e$, which is the solution resistance between the working and reference electrode. The film resistance associated with the higher frequency semicircle, R$_{film}$, is assigned to lithium-ion diffusion through surface films. The semicircle in the middle frequency range indicates the charge-transfer resistance (R$_{ct}$), relating to charge transfer through the electrode/electrolyte interface. The values for the electrodes after cycling calculated from the diameters of the semicircles in the Nyquist plots are summarized in table 4.1. The uncompensated resistance (R$_e$) of Ge-PPy is smaller than that of the Ge electrode due to the decreased resistance between the active material and the electrolyte from the introduction of PPy. From comparison the diameters of the semicircles, the values of R$_{film}$ and R$_{ct}$ of the composite electrode are both lower than those for the pristine Ge electrode, indicating that the conducting PPy can significantly increase electrical conductivity for the Ge nanoparticles. This is because the conjugation of the single and

double bonds alternating within the oxidized PPy macromolecular architecture allow the extra electrons in a conjugated system free to be roamed or move through the polymer chain, which could induce electrical conductivity. Through *p*-doping, the electrical conductivity of PPy can even reach the level of a few tenths of 1 S cm^{-1} [71, 208], even though it is only around 1×10^{-2} S cm^{-1} for crystalline germanium. Accordingly, the introduction of PPy can decrease the charge transfer resistance for the electrode.
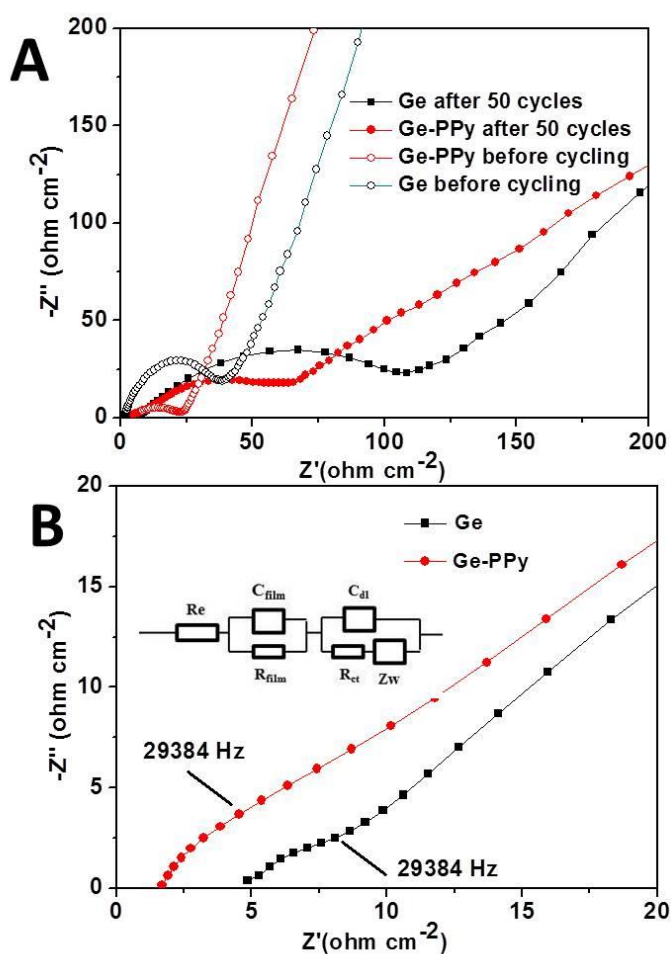
Figure 4.6 (A) Nyquist impedance plots of the Ge and Ge-PPy composite electrodes before and after 50 cycles. (B) Enlargement of (A) in the high frequency range of the electrodes after 50 cycles. The inset in (B) is the equivalent circuit used.

Table 4.1 Values of R_e, R_{film} and R_{ct} from Nyquist plots for the Ge and Ge-PPy electrodes after 50 cycles.

	R_e (ohm cm^2)	R_{film} (ohm cm^2)	R_{ct} (ohm cm^2)
Ge	4.844	5.438	98.45
Ge-PPy	1.801	4.851	65.23

To confirm that the Ge-PPy electrode still retained robust mechanical and electrical support after cycling, SEM images of the electrodes fabricated from the Ge and Ge-PPy composite were collected before and after cycling to directly analyse any changes in the microstructure or morphology of the particles during cycling. The surfaces of both electrodes before cycling are similar (Fig. 4.7(a, b)). After 50 cycles, however, there are large agglomerations of particles 10 μm in size and clearly visible cracks in the bare Ge electrode (Fig. 4.7(c)). From Fig. 4.7(d), it can be observed that PPy can protect the electrode from pulverization, but there are still some clearly visible cracks on the surface of the electrode. It can be deduced that PPy not only act as a conductive host matrix, but also work as a binder to prevent the pulverization and delamination of the active material on the surface of the electrode during lithium alloying and de-alloying. We need to point out that PPy core still cannot protect the Ge nanoparticles from cracking. This is because the Ge nanoparticles are only attached on the surface of the PPy, so the PPy core cannot relieve the huge volume change by Ge agglomeration.

73
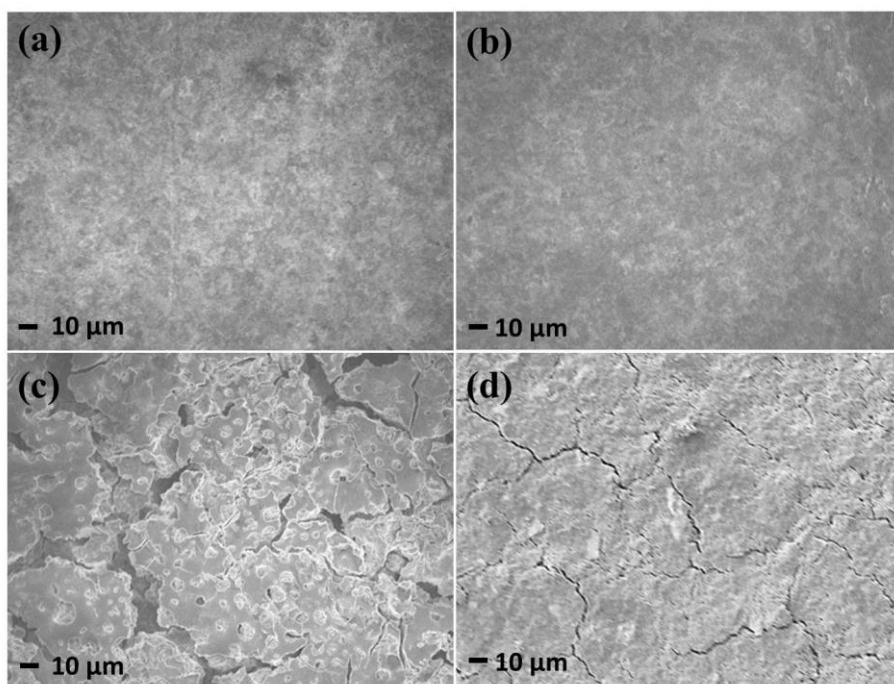
Figure 4.7 SEM images of the surfaces of Ge (a, c) and Ge-PPy (b, d) electrodes before (a, b) and after 50 cycles (c, d).

4.4 Summary

A novel nanostructured Ge-PPy composite has been successfully fabricated by a simple chemical reduction method and demonstrated to be a promising anode material for LIBs. After amorphous Ge nanoparticles were coated on the PPy surface, improved cycling performance and high rate capacity were achieved. The enhanced electrochemical performance can be attributed to the conductive PPy core, which not only can provide efficient electronic pathways for Ge nanoparticles, but also buffers the pulverization and delamination of the electrode caused by the huge volume changes of Ge nanoparticles during lithium alloying and de-alloying. We also expect our strategy to also be useful for fabricating metal nanoparticles on conducting polymer surface structures, which will be of general interest and have influence in other fields.

Chapter 5   Porous Ni$_{0.5}$Zn$_{0.5}$Fe$_2$O$_4$ Nanospheres:

Synthesis, Characterization, and Application

for Lithium Storage

5.1 Introduction

Hollow or porous-structured transition metal oxides are of great interest in many applications, such as catalysts, batteries, super capacitors, solar cells, and fuel cells [209-211], owing to their large specific surface areas. The Li-ion battery is the most important energy storage device in our daily life for portable devices and potentially for electric vehicles. As possible substitutes for commercial graphite materials (theoretical specific capacity of 372 mAh g^{-1}), transition metal oxides have attracted considerable attention from researchers around the world, who are interested in their potential as high capacity anode materials for lithium ion batteries (LIBs) [125, 212]. Nevertheless, finding electrode materials with high energy density and excellent cycling stability is still a great challenge for LIBs [8, 28].

Compared with the various simple transition metal oxides, such as NiO, ZnO, Fe$_2$O$_3$, Co$_3$O$_4$, Cr$_2$O$_3$, and CuO [213-215], nanostructured spinel ferrites with the general formula AFe$_2$O$_4$ (A = Ni, Zn, Co, Cu) [144, 216] are of great interest because of their high initial discharge capacity (over 1000 mAh g^{-1}). Ding et al. [217] prepared ZnFe$_2$O$_4$ by the polymer pyrolysis method (PPM), and the ferrite samples prepared via this method show superior capacities and cycling stabilities, with an initial specific capacity as high as 1419.6 mAh

g^{-1} that is maintained at over 800 mAh g^{-1} even after 50 cycles. Zhao et al. [218] have reported that the initial discharge capacity of nanosized $NiFe_2O_4$ could reach as high as 1314 mAh g^{-1}, which is attributed to the large surface area and short diffusion length of the nanostructure. The discharge capacity, however, decreased to 790.8 mAh g^{-1} after 2 cycles and to 709.0 mAh g^{-1} after 3 cycles at a current density of 0.2 mA cm^{-2}. Liu and co-workers [219] reported that $NiFe_2O_4$ showed the highest reported initial discharge capacity of 1400 mAh g^{-1}, which was due to its nanoscale particle size and better crystallinity, although this material demonstrated relatively poor capacity retention. Zhao's group [220] found that $ZnFe_2O_4$ prepared by the hydrothermal method exhibited the initial discharge capacity of 1287.5 mAh g^{-1}, although the discharge capacity of these nanoparticles declined to 746 mAh g^{-1} after 2 cycles.

The reaction route, particle size, and morphology of spinel ferrite can play very important roles in the electrochemical performance of LIBs [221]. It was found that the capacity retention of metal oxides can be improved by fabricating materials in hollow or mesoporous nanostructures, which could accommodate volume changes and shorten the lithium diffusion length [144, 217]. Hollow $ZnFe_2O_4$ nanospheres with a diameter of 1 μm were synthesized by Guo et al. [152] via hydrothermal reaction followed by annealing at 600 °C in air, and the hollow spherical structure significantly increased the specific capacity and improved capacity retention, although the process required a high reaction temperature, which resulted in agglomeration of the hollow spheres. Deng et al. [222] prepared $ZnFe_2O_4$ hollow spheres of a suitable size with a carbon template. Although the resulting composites showed a high specific capacity of 911 mAh g^{-1}, the synthetic steps are complicated with templates involved. Very recently, Wang et al. [223] successfully synthesized the MFe_2O_4 (M = Zn, Co, Ni) nanorods by a template-engaged reaction. The merits of one-dimensional (1D) nanostructure and its high reversible capacity make the

spine ferrite very prospective candidates as anodes for LIBs.

Cherian et al. [224] studied the effects of zinc-doped nickel ferrite and the consequent cation redistribution on the Li-cycling behavior. An enhancement in the capacity with increasing Zn concentration is observed for $x = 0.4$ and 0.6. In addition, in the case of $Zn_{1-x}Ni_xFe_2O_4$ ferrite [153], it was found that for x greater than 0.5, Fe^{3+} moments in A and B sites have a collinear arrangement, whereas for x less than 0.5, Fe^{3+} moments in the B sites have a non-collinear arrangement. Therefore, it is necessary to further study the electrochemical properties of $Ni_{0.5}Zn_{0.5}Fe_2O_4$ nanospheres.

To avoid the problems mentioned above and obtain high capacity with good capacity retention, we synthesized mesoporous $Ni_{0.5}Zn_{0.5}Fe_2O_4$ (NZFO) nanospheres via the solvothermal method and investigated the effects of the morphology on the electrochemical performance. To the best of our knowledge, no group has reported the electrochemical performance of hollow or mesoporous structured NZFO prepared by a one-step solvothermal method. The as-prepared mesoporous NZFO nanospheres showed excellent electrochemical performance with high initial discharge capacity and good capacity retention.

5.2. Experimental

All reagents were analytical grade and were used without further purification. In order to synthesize NZFO, stoichiometric amounts of nickel nitrate, zinc nitrate, and iron nitrate were dissolved in 30 ml ethylene glycol (EG) under magnetic stirring. After stirring for 60 min, a suitable amount of urea was slowly added to the mixed nitrate solution. The mixture was stirred for 2 h to obtain a clear solution. Subsequently, the solution was

sealed in a Teflon-lined autoclave (50 ml capacity) and maintained at 180 °C for 24 h. Then, the mixture was cooled to room temperature naturally. The resultant products were washed with deionized water and ethanol several times, and then dried in a vacuum oven at 80 °C overnight. For simplicity, the NZFO powders obtained under the same reaction conditions of temperature and reaction time, but with different reactant concentrations, are denoted as NZFO-A, where A represents the mole number of the as-prepared NZFO powders, respectively. For example, NZFO-200 indicates that 0.002 mol NZFO powders were prepared at 180 °C with 24 h reaction time. In order to investigate the influence of the reactant concentrations on the final products, the molar ratio of $Ni(NO_3)_2•6H_2O$, $Zn(NO_3)_2•6H_2O$, $Fe(NO_3)_3•9H_2O$, and urea was kept constant (1:1:4:16), and the volume of EG was fixed at 30 ml.

X-ray diffraction (XRD) patterns of the as-prepared products were collected on a Philips X'pert PRO X-ray diffractometer with Cu Kα radiation. Field emission scanning electron microscopy (FESEM, FEI Sirion 200) and transmission electron microscopy (TEM, JEM-2010) were used to show the surface morphology and particle size distribution. The surface area of the samples was determined by nitrogen adsorption (Autosorb-iQ-Cx).

To test the electrochemical performance, as-prepared samples were mixed with acetylene black and a binder, sodium carboxymethyl cellulose (CMC, average Mw: ~250 000, Aldrich), in a weight ratio of 80:10:10 in deionized water. The slurry was uniformly pasted onto pieces of Cu mesh with an area of 1 cm^2. Such prepared electrode sheets were dried at 90 °C in a vacuum oven for 12 h. The electrodes were not pressed for electrochemical testing. The electrochemical cells (CR 2032 coin-type cells) contained the composite on Cu mesh as the working electrode, Li foil as the counter electrode and reference electrode, a porous polypropylene film as separator, and 1 M $LiPF_6$ in a 1:2

(v/v) mixture of ethylene carbonate (EC) and diethyl carbonate (DEC) as the electrolyte. The cells were assembled in an Ar-filled glove box. The cells were cycled at a current density of 50 mA g^{-1} between 0.01 and 3.0 V using a computer-controlled charger system manufactured by Land Battery Testers. The specific capacity is based on the weight of NZFO. The loading mass of NZFO is 3-5 mg cm^{-2}. Electrochemical impedance spectroscopy (EIS) was conducted using a Biologic VMP-3 electrochemical workstation.

5.3. Results and discussion

5.3.1. Structure and morphology

Figure 5.1 shows the XRD patterns of the Ni-Zn ferrites prepared using different reactant concentrations. All reflection peaks match with the standard JCPDS card of Ni-Zn ferrite (card no. 08-0234), and no other phase is detectable. The lattice constant (*a*) values, obtained by Rietveld refinement and listed in Table 5.1, are larger than that of Fe$_3$O$_4$ (8.36 Å) [225]. The Rietveld refined XRD pattern of the typical NZFO-300 sample is shown in the inset of Fig. 5.1. In Fig. 5.1, the corresponding diffraction peaks become narrower and sharper with increasing concentration, indicating better crystalline and growth in crystallite size. The crystallite size (*D*) was calculated by the Williamson-Hall plots equation[226]:

$$\beta \cos\theta = \varepsilon(4\sin\theta) + \lambda/D, \tag{5.1}$$

where β is the measured full width at half maximum (FWHM) for XRD corresponding to different crystal planes, θ is the Bragg angle, ε is the strain and D is the crystallite size. The crystallite size increased from 22 to 35 nm as the reaction concentration increased.
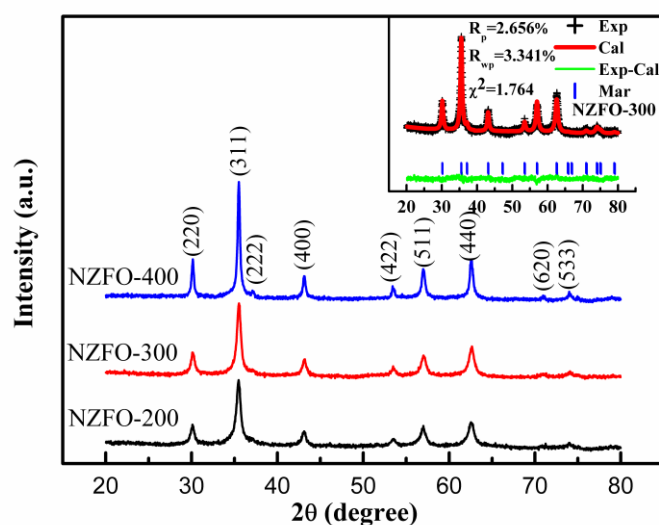
Figure 5.1 XRD patterns of NZFO samples with different reactant concentrations; the inset shows the Rietveld refinement results for NZFO-300.

Table 5.1 Lattice constant a (Å), crystallite size (nm), and nanosphere size (nm) of the NZFO samples as a function of the reactant concentration.

sample	Lattice constant (Å)	Crystallite size (nm)	Nanosphere size (nm)
NZFO-200	8.3796	22	145
NZFO-300	8.3811	23	125
NZFO-400	8.3865	35	62

Figure 5.2 shows the morphology and corresponding size distribution graphs of all the NZFO samples. All the particles show a spherical shape with a rather homogeneous nanosphere size. The size distribution of the nanospheres was estimated by taking the average of 200 nanospheres and fitting the resultant histogram by a Gaussian function (solid line), as shown in the insets of Fig. 5.2. The average nanosphere sizes are listed in

Table 5.1. The centre of the size distribution curves was shifted from 145 to 62 nm as the concentration of the reaction solution was increased from 2 to 4 mM, showing the significant influence of the reactant concentration on the nanosphere size. This can be explained by the classical theories of crystal heterogeneous nucleation [227]. In our experiment, the urea can provide centers of heterogeneous nucleation. Therefore, increasing the concentration will lead to a decrease in the average particle size. Open pores and some broken spheres can also be seen in Fig. 5.2(d), as marked by the arrows, indicating the presence of hollow spheres in the NZFO-300 sample.
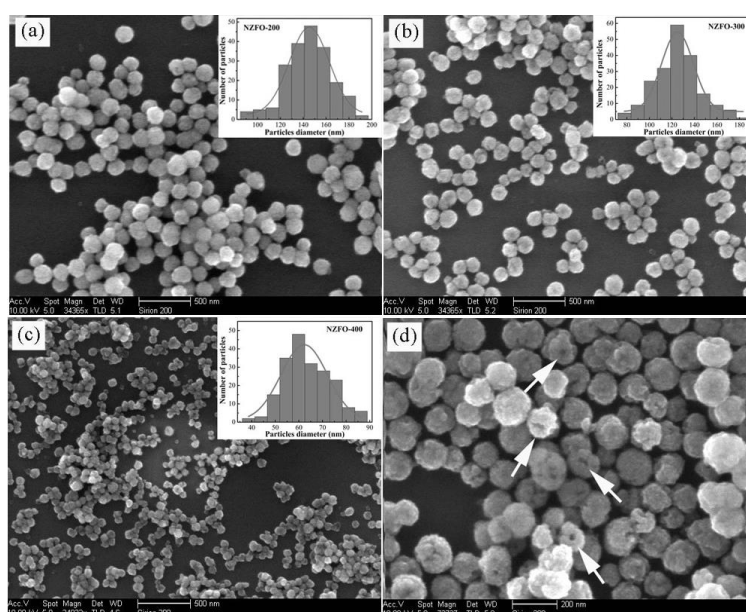
Figure 5.2 FESEM images of NZFO ferrite produced with different reactant concentrations, with the insets showing the corresponding particle size distribution graphs: (a) NZFO-200, (b) NZFO-300, (c) NZFO-400; and (d) a high-magnification FESEM image of NZFO-300. The arrows in (d) indicate broken nanospheres, showing their hollow nature.

Transmission electron microscopy (TEM) was used to further confirm the structure of the

nanospheres. Fig. 5.3 shows TEM images of the NZFO-200, NZFO-300 and NZFO-400 samples. Uniform and monodisperse nanospheres are observed. Fig. 5.3(a), (b), and (c) clearly reveal that the spherical shells are packed with numerous NZFO nanoparticles. In Fig. 5.3(b), the contrast between the dark edge and the pale center indicates the hollow interior structure of the NZFO-300 nanospheres. High-resolution TEM (HRTEM) analysis was employed to determine the crystal facets and orientation. As shown in Fig. 3(d), (e) and (f), the lattice fringe spacings of d = 0.30 nm and d = 0.25 nm agree well with the (220) and (311) lattice planes of the XRD patterns of cubic NZFO, respectively. The different contrast in Fig. 5.3(d) and (e) indicates that NZFO-200 and NZFO-300 may have a porous structure with pore size smaller than 5 nm.
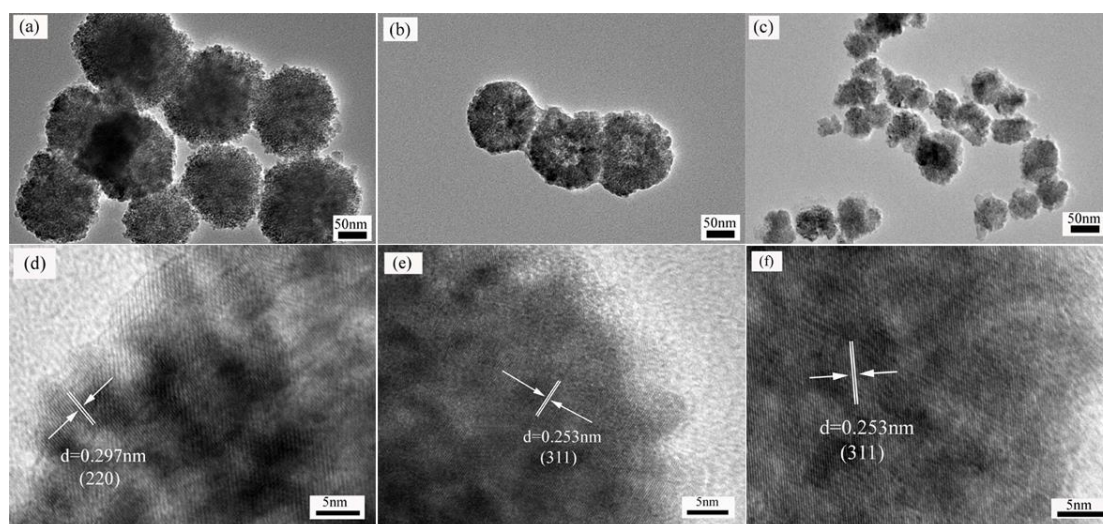
Figure 5.3 TEM images of NZFO ferrite synthesized with different reactant concentrations: (a) NZFO-200, (b) NZFO-300, (c) NZFO-400; high magnification TEM images: (d) NZFO-200, (e) NZFO-300, (f) NZFO-400.

Fig. 5.4 presents the N_2 adsorption-desorption isotherms of the samples and the corresponding Barret-Joyner-Halenda pore size distribution curves. The measured Brunauer-Emmett-Teller (BET) surface area (S_{BET}) for NZFO-200 and NZFO-300 is about 101.3 and 77.2 m^2 g^{-1}, respectively. It can be seen that the S_{BET} decreases from

101.3 to 77.2 m^2 g^{-1} as the reaction concentration increases. The relatively high S_{BET} for NZFO-200 may be due to its narrow particle size distribution, as shown in Fig. 5.4(c). The isotherms in Fig. 5.4(a) and (b) are identified as type IV, which is characteristic of mesoporous (2-50 nm) materials. The NZFO-200 sample has sharp peaks at 2 and 31 nm, indicating the presence of mesopores.

The formation of the hollow NZFO nanospheres could be explained by the Ostwald ripening process[222]. In the sealed solvothermal reaction system, CO_2 bubbles resulting from the thermal decomposition of urea can serve as soft templates to induce the hollow/porous nanostructure. The gas bubbles provide the nucleation centers for NZFO nanoparticles to aggregate around the gas-liquid interface. As the reaction proceeds, hollow NZFO nanospheres are formed.
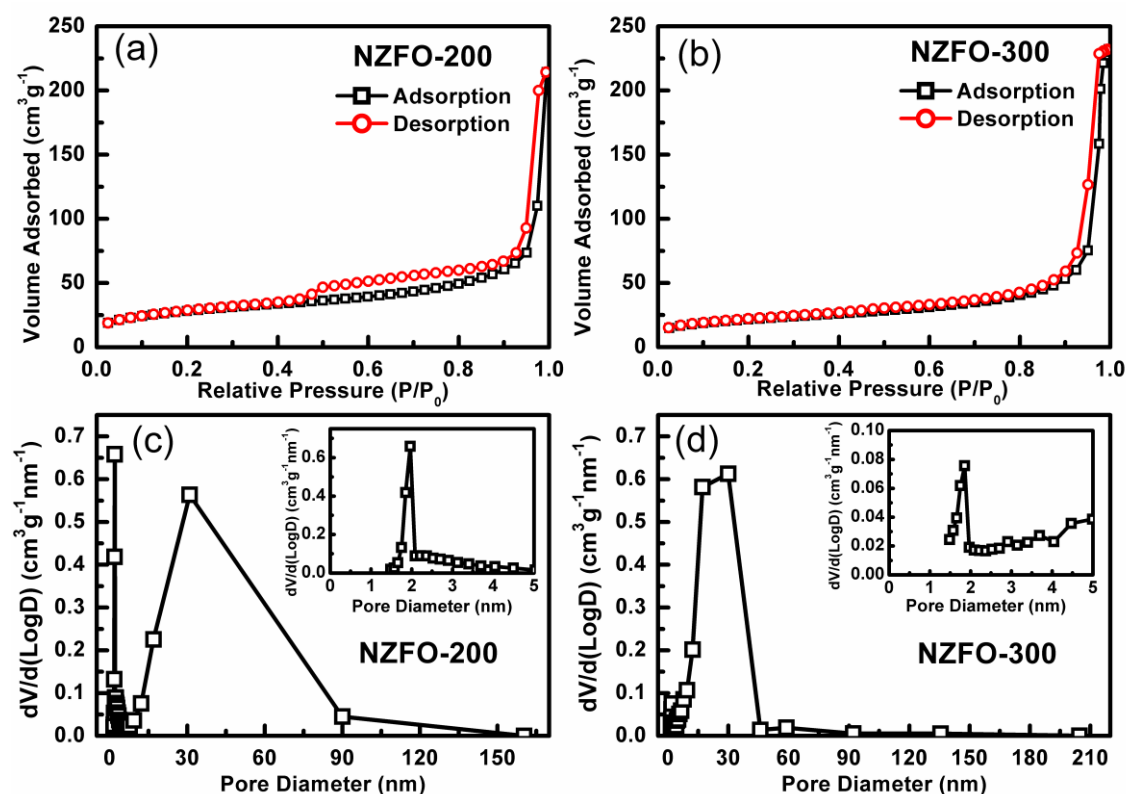
Figure 5.4 Nitrogen adsorption-desorption isotherms of (a) NZFO-200, (b)NZFO-300; and pore size distributions of (c) NZFO-200, (d) NZFO-300 (insets: magnified 0-5 nm

regions).

Fig. 5.5 contains a schematic illustration of the formation mechanism of the hollow/mesoporous nanospheres. Based on the above analysis, when the reactant concentration is relatively low, the size of the bubbles generated from the decomposition of urea is too small to accelerate the Ostwald ripening because the gas is trapped between the interfaces, resulting in mesoporous spheres. Therefore, the urea only has a positive effect on the reduction capability of ethylene glycol, but there is not enough gas for the bubbles to act as soft templates, so that porous-structured nanospheres are only partially formed. As the reactant concentration increases, more gas bubbles are produced, thus accelerating the Ostwald ripening process, which results in the formation of hollow nanospheres. According to the formation of crystals[228], the rate of the generation or the quantity of the gas bubbles plays an important role in controlling the particle size. In the same volume of the EG, as urea increases to a higher amount, the more bubbles are produced, and the quantity of $Ni_{0.5}Zn_{0.5}Fe_2O_4$ aggregation in each bubble will be reduced, resulting in the decrease of the nanosphere size.
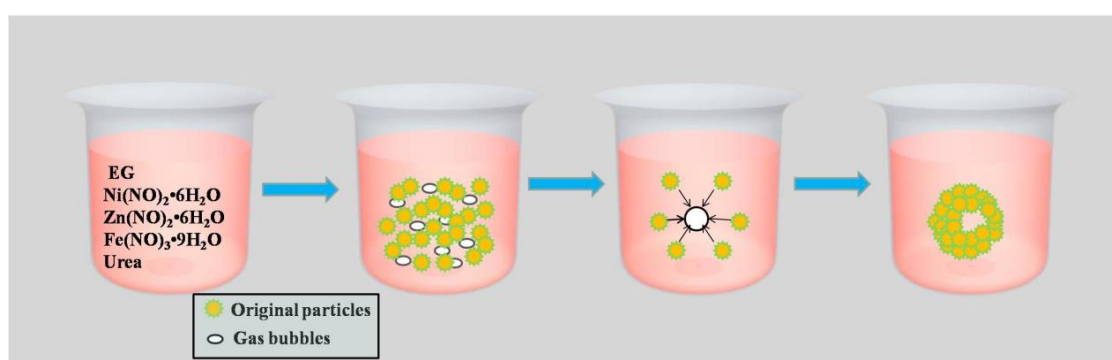
Figure 5.5 Schematic illustration of the formation mechanism of hollow magnetic nanospheres.

5.3.2. Electrochemical characterizations

Figure 5.6 shows the charge-discharge curves of selected cycles for the first 50 cycles of NZFO-200, NZFO-300, and NZFO-400 electrodes in coin test cells using lithium as the counter and reference electrode between 0.01 and 3.0 V (vs. Li^+/Li). All the charge-discharge curves in Fig. 6 show similar features to those of transition metal oxide electrodes reported previously in the literature [215, 218, 219]. The first discharge curves all show a plateau at 0.75 V. The initial discharge specific capacity is in the order of NZFO-200 > NZFO-300 > NZFO-400.

The theoretical capacity of NZFO from the reduction reactions of Ni (II), Zn (II), and Fe (III) to Ni (0), Zn (0), and Fe (0), respectively, is 902 mAh g^{-1}, corresponding to maximum lithium uptake of 8 Li per NZFO. The equation is as follows:

$$2 \, Ni_{0.5}Zn_{0.5}Fe_2O_4 + 16 \, Li^+ + 16 \, e^- \rightarrow 4 \, Fe + Zn + Ni + 16 \, Li_2O \qquad (5.2)$$
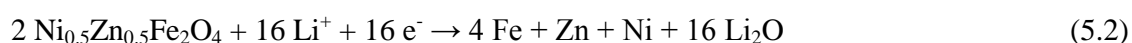
The initial discharge capacity is always higher than the theoretical capacity, which is due to the decomposition of electrolyte and the formation of the solid electrolyte interphase (SEI). The possible reaction between Zn and Li would be another contribution to the high capacity[229].

$$Zn + Li^+ + e \leftrightarrow LiZn \qquad (5.3)$$

The highest surface area sample, NZFO-200, shows the highest initial discharge capacity of 1480 mAh g^{-1}. The reversible capacity is due to the reversible reaction of Li_2O and the transition metals:

$$4Fe + Zn + Ni + 8 \, Li_2O \leftrightarrow 2 \, Fe_2O_3 + ZnO + NiO + 16 \, Li^+ + 16 \, e^- \qquad (5.4)$$

The highest reversible capacities were also observed for the NZFO-200 sample, up to 1100 mAh g^{-1}.
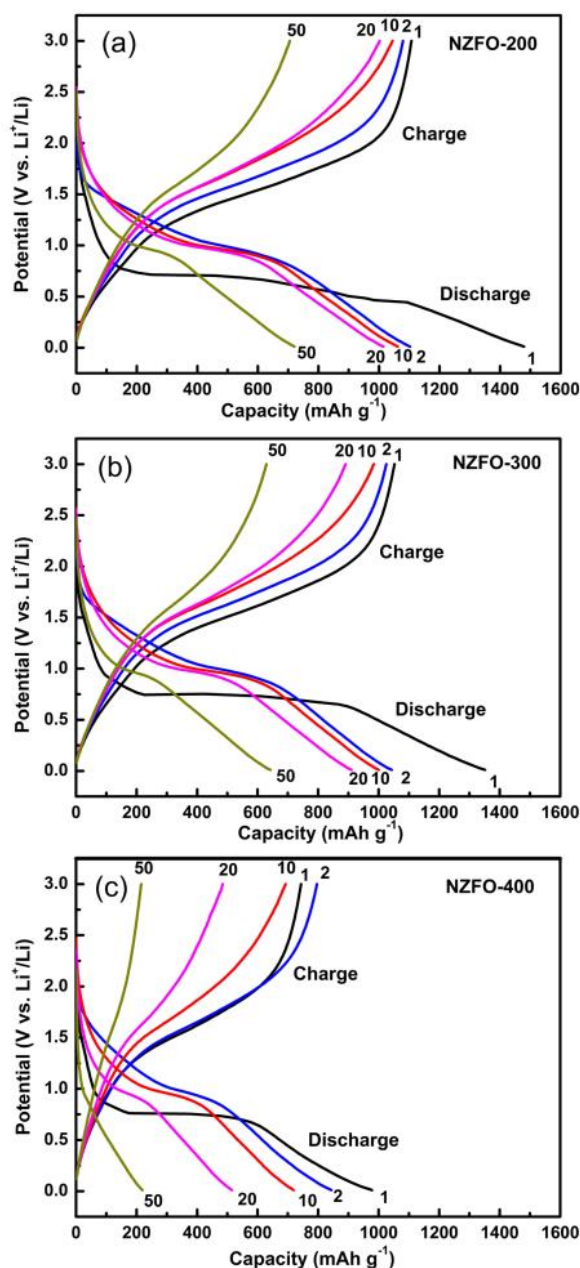
Figure 5.6 Charge and discharge curves for selected cycles of NZFO-200 (a), NZFO-300 (b), and NZFO-400 (c) electrodes.

The *dQ/dV* results are also plotted in Fig. 5.7. In the 1st cycle [Fig. 5.7(a)], an additional peak can be found at 0.46 and 0.66 V for the NZFO-200 and NZFO-300 samples, respectively. This may be due to the further lithiation of ZnO to give a Li–Zn alloy, as a similar peak between 0.2 and 0.5 V was observed in the literature [230]. The high intensity of the 0.46 V peak of the NZFO-200 sample indicates the highly reversible reaction of Zn

and lithium, which can be attributed to the mesoporous structure with small crystallite size and high surface area. Fig. 5.7(b) presents the *dQ/dV* curves of the 50th cycle. One pair of redox peaks can be found at 1.0 V and 1.6 V for the NZFO-200 and NZFO-300 samples. The higher intensity of NZFO-200 indicates higher capacity. The NZFO-400 sample shows small reversible peaks, indicating the lowest reversible capacity.
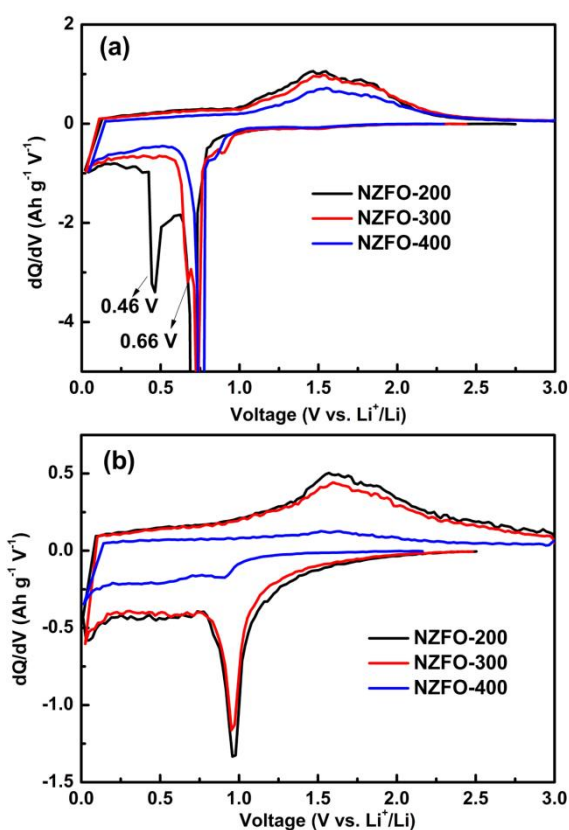
Figure 5.7 *dQ/dV* curves of NZFO-200, NZFO-300, and NZFO-400 electrodes at the 1st cycle (a) and the 50th cycle (b).

The cycle life and coulombic efficiency of samples are presented in Fig. 5.8. The capacity retention is in the same order as the surface area. The best capacity retention that can be obtained here is for the NZFO-200 sample with 700 mAh g^{-1} up to 50 cycles. Our results show that the performance of the mesoporous nanosphere electrode (NZFO-200) with high surface area is better than that of the hollow/porous nanosphere electrode (NZFO-300) with low surface area in terms of reversible capacity and cycle life. It is also worth

mentioning that there is a large deviation in potential between the charge and discharge profiles, owing to the large polarization related to ion transfer during the cycling process. This phenomenon is often observed in many metal oxide anodes due to poor electrical conductivity [231-233]. We also compare the coulombic efficiency for the samples (Fig. 5.8 (b)). The coulombic efficiency is 71 % for the first cycle and 80-95 % for cycles 3-12. In contrast, NZFO-200 and NZFO-300 show dramatic improvement of coulombic efficiency (~ 75 % for the first cycle, 98.4-99 % for the following cycles), which provide strong evidence that there is little fatigue in NZFO during cycling.
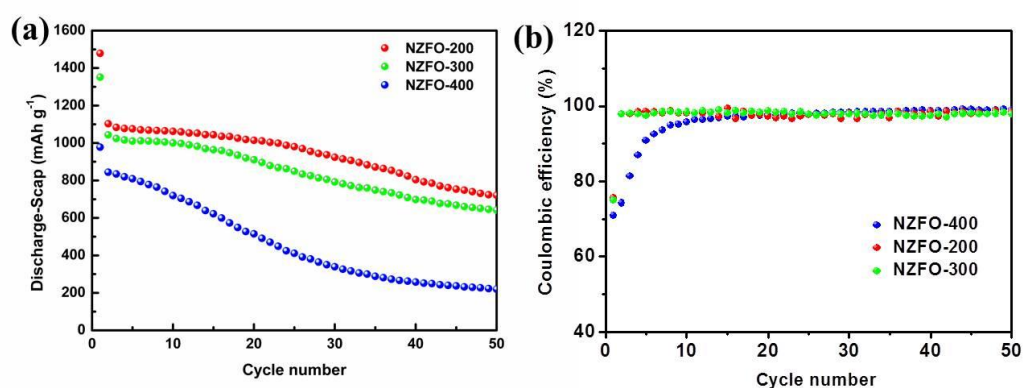
Figure 5.8 Cycle life (a) and coulombic efficiency (b) of NZFO-200 (red), NZFO-300 (green), and NZFO-400(blue) electrodes.

The rate performance was also investigated to characterize the stability of the NZFO-200 and NZFO-400 electrodes, as shown in Fig. 5.9 (a). The NZFO-200 electrode shows the highest specific capacity of 508 mAh g^{-1} at a current density of 1 A g^{-1}. The capacity retention rates at 500 mA g^{-1} and 1 A g^{-1} are 75.5 % and 56.1 % compared to the 100 mA g^{-1} capacity, respectively. In comparison, the NZFO-400 electrode shows relatively poor high rate capability, with less than 15% capacity retention at current density of 1 A g^{-1}. A comparison of coulombic efficiencies also has been provided in Fig. 5.9(b). Obviously, NZFO-200 has much higher coulombic efficiency than NZFO-400 as the current density is changed, which mainly due to the relatively high electrical conductivity of NZFO-200

compared to NZFO-400. The high rate capability can be attributed to the high surface area and mesoporous structure, which can enhance contact between the electrode and electrolyte, and shorten the lithium diffusion length.
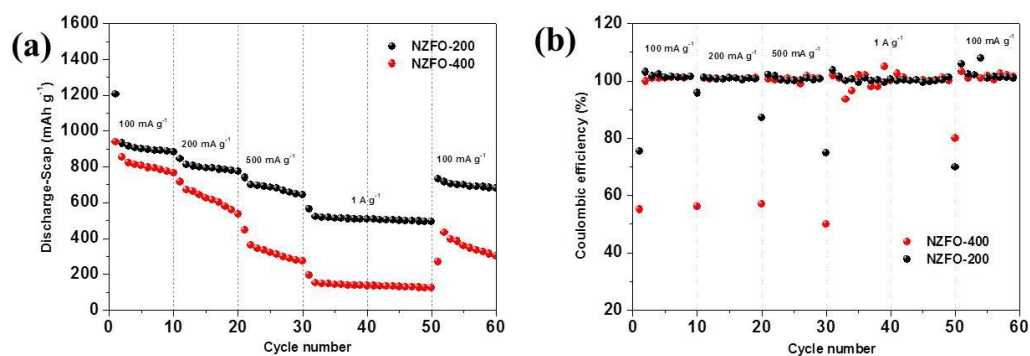
Figure 5.9 Rate performances (a) and coulombic efficiency (b) of NZFO-200 and NZFO-400 electrodes at different current density rates from 100 mA g^{-1} to 1000 mA g^{-1} and back to 100 mA g^{-1} between 0.01 and 3.0 V.

To investigate the reasons for the enhanced capacity retention in NZFO-200, the electrodes were washed and dried after cycling, and the changes in morphology were examined by SEM. SEM images of the surfaces of the electrodes before and after cycling are shown in Fig. 5.10. The top SEM images show the electrode surfaces before cycling, while the bottom ones show the surfaces after 50 cycles. The electrodes before cycling show a similar smooth surface, while after cycling, the electrode morphology shows big differences. The surface of the NZFO-200 electrode after cycling shows a porous morphology, while the NZFO-400 electrode shows morphology that features big cracks. The growth of the big cracks will produce high resistance and cause contact between the active materials to be lost, resulting in poor capacity retention. The difference in the electrode morphology could be related to the differences in the morphology and surface area of the active materials. Since the formation of the solid electrolyte interphase (SEI) layer plays a very important role in the cycling stability of the active materials, the higher

89

surface area and mesoporous structure of NZFO-200 could be of benefit for the formation of more stable SEI compared with NZFO-400.
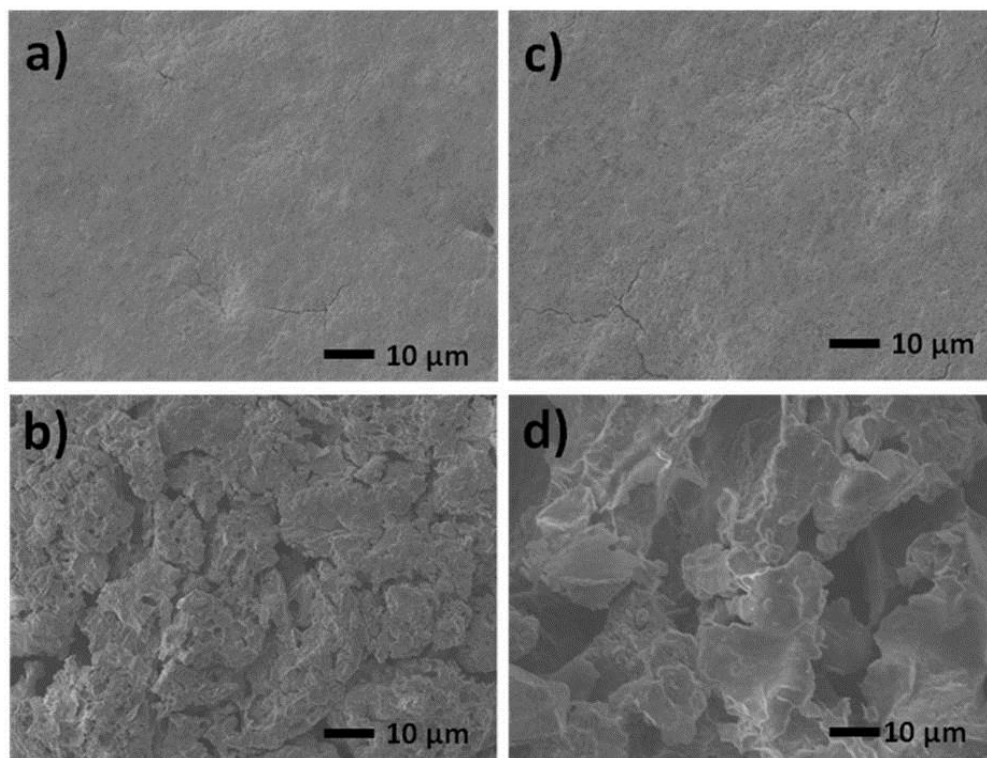
Figure 5.10 SEM images of the electrode surface of NZFO-200 electrode (a, b) and NZFO-400 electrode (c, d), before (a, c) and after (b, d) 50 cycles.

Electrochemical impedance spectroscopy (EIS) was used to explain the reasons for the enhanced rate capability and capacity retention of the NZFO-200 electrode. The Nyquist plots (Figure 5.11) show a semicircle in the high to medium frequency range, which describes the charge-transfer resistance (R_{ct}) for both electrodes. The intercept value is considered to represent the total electrical resistance offered by the electrolyte (R_s). The inclined line represents the Warburg impedance (Z_w) at low frequency, which indicates the diffusion of Li^+ in the solid matrix. The impedance plots were fitted using the equivalent circuit model shown in the inset. As shown in table 5.1, the R_{ct} of the NZFO-200 after 5 cycles (140 Ω) and after 50 cycles (254 Ω) is much smaller than those of the

NZFO-400 after 5 cycles (188 Ω) and after 50 cycles (560 Ω), respectively, giving evidence that the high surface area of the NZFO-200 improved the battery performance over extended cycling. However, the capacity still gradually decreases for all samples. Further work can be done to improve the capacity retention via making carbon composite materials.
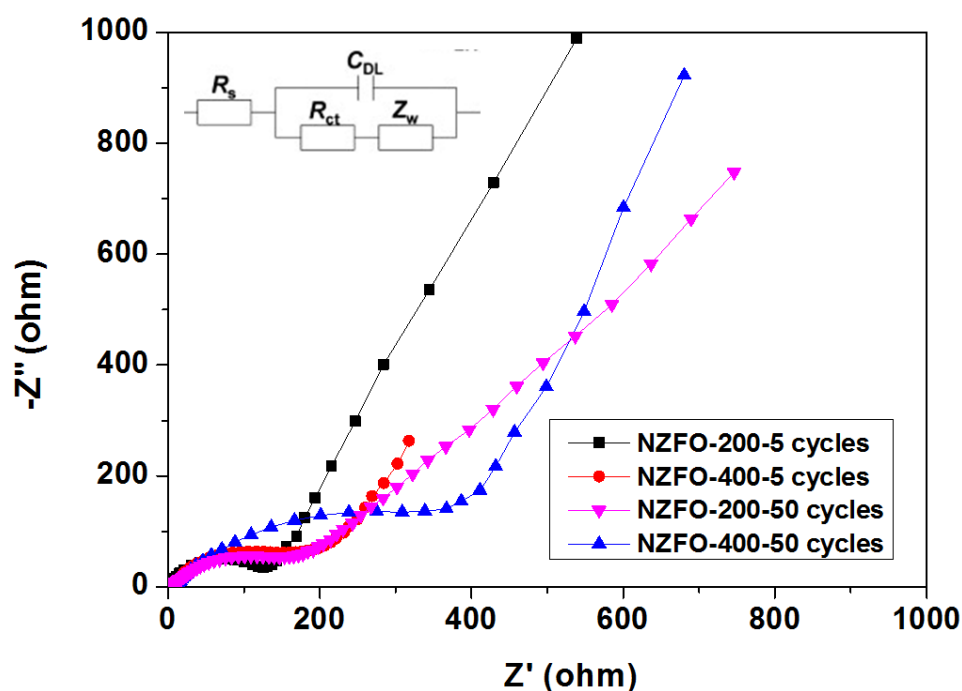
Figure 5.11 Nyquist plots of NZFO-200 electrode and NZFO-400 electrode, after cycling over 5 and 50 cycles at a discharge potential of 0.7 V vs. Li/Li$^+$ at 25 °C at frequencies from 100 kHz to 20 mHz. The inset is the equivalent circuit used.

Table 5.2 Measured EIS data on NZFO-200 and NZFO-400 electrode after various cycles.

	R_s (Ω)	R_{ct} (Ω)
NZFO-200 (5 cycles)	1.5	140
NZFO-200 (50 cycles)	3.6	254
NZFO-400 (5 cycles)	2.1	188
NZFO-400 (50 cycles)	5.9	560

5.4. Summary

In summary, monodisperse mesoporous $Ni_{0.5}Zn_{0.5}Fe_2O_4$ nanospheres have been synthesized via a one-step solvothermal method. Nanospheres with different morphologies, crystallite sizes, and diameters can be tuned by adjusting the reactant concentration, which has been confirmed by the XRD, FESEM, and TEM observations. The formation mechanisms of the mesoporous and/or hollow nanospheres have been discussed based on the Ostwald ripening process. The mesoporous $Ni_{0.5}Zn_{0.5}Fe_2O_4$ nanospheres with small crystallite size and high surface area show high reversible specific capacity and better capacity retention, suggesting that mesoporous $Ni_{0.5}Zn_{0.5}Fe_2O_4$ nanospheres can have promising applications in lithium ion batteries.

Chapter 6   Synthesis and Electrochemical

Performance of LiV$_3$O$_8$/polyaniline as

Cathode Material for the Lithium-ion Battery

6.1 Introduction

The layered lithium vanadium oxide, LiV$_3$O$_8$ has received considerable attention as cathode material in rechargeable lithium batteries due to its excellent electrochemical performances: high specific energy density, high working voltage, high discharge capacity, good chemical stability in air, ease of fabrication and low cost [234-237]. It is well understood that the electrochemical properties of lithium vanadium oxide are largely depend on the preparation method. Therefore, many preparation methods have been studied to LiV$_3$O$_8$ with an aim to improve its electrochemical performance, such as spray pyrolysis method [238], sol-gel method [239-241], microwave-assisted synthesis [52], ultrasonic treatment [237] and hydrothermal synthesis [47]. Recently, Liu et al. [242] employed home-made VO$_2$ nanorods as the vanadium precursor to prepare the LiV$_3$O$_8$ cathode materials. The as-obtained single-crystalline LiV$_3$O$_8$ nanorods with high crystallinity greatly improved the stability of the crystallographic structure during cycling. It exhibited high initial discharge capacity of more than 300 mAh g^{-1} at current densities of 20 mA g^{-1}. Up to now, however, this kind of material was still suffer from the phase transformation and dissolution of small quantity of LiV$_3$O$_8$ in the electrolyte [243], which lead to low high-rate capacity and fast capacity fading with cycling.

Recently, coating with conducting polymers has been studied as an effective method to improve the electrical performance of cathode and anode materials in LIBs. Conductive polymers are attractive additive materials for LIBs, owing to their special electrochemical properties: (a) they can be charged and discharged by a redox reaction involving lithium ions or counter anions of the electrolyte; (b) they have an influence on the overall phase-change rate; and (c) they can connect isolated crystalline particles, preventing their agglomeration on the surface of electrodes. Moreover, conducting polymers can suppress the dissolution of active materials into the $LiPF_6$ electrolyte [244-246]. Up to now, many electrode materials combined with polymers, for example, SnO_2/polypyrrol [191], sulphur/polypyrrole[247], $LiMn_2O_4$/polypyrrole [245], $LiFePO_4$/polypyrrole [79, 248], $LiFePO_4$/polyaniline [249], V_2O_5/polyaniline [250], and LiV_3O_8/polypyrrole [55, 198] have been synthesised and have shown improved cycling performance in lithium cells. In our previous work, polypyrrole coated LiV_3O_8 exhibited improved cycling stability [55, 198]. The rate capability, however, was not discussed in these studies. In this study, we have tried to investigate the effects of a conducting polymer on the high rate capability of LiV_3O_8 and to explore a possible new conducting polymer to improve the electrochemical performance of LiV_3O_8 cathode.

Among the various conductive polymers, polyaniline (PAn) has been used extensively because it can be easily produced with the desired morphology and structure by chemical reaction. It can promote electrolyte permeation into the surface of the active particles, and hence enhance Li^+ insertion/extraction during the charge/discharge process [249]. It is also superior to polypyrrole and polythiophene in energy density and durability [251]. In addition, polyaniline is electrochemically active in the range of 2.0-3.8 V [85], which overlaps the operative redox couple of LiV_3O_8. Therefore, polyaniline not only serves as a conductive binder-like carbon powder for LiV_3O_8 electrodes, but also participates as an

active material. Herein, the LiV_3O_8 nanorods were coated with polyaniline via simple chemical oxidative polymerization directed by the anionic surfactant sodium dodecyl benzene sulfate (SDBS). The electrochemical properties of LiV_3O_8-PAn as cathode material were systematically investigated.

6.2 Experimental

6.2.1 Materials synthesis

LiV_3O_8 nanorods were synthesized by the hydrothermal reaction method, combined with a convenient solid-state reaction, as reported elsewhere [242]. In a typical experiment, the VO_2 nanorod precursor was prepared by the hydrothermal method. 0.365 g V_2O_5 powder, 10 ml 1-butanol, and 30 ml H_2O were mixed under vigorous magnetic stirring at room temperature for 4 h. The resultant mixture was then transferred into an autoclave and kept in an oven at 180 °C for 48 h. The products were washed with anhydrous ethanol and cyclohexane several times. The produced VO_2 was dried at 80 °C in a vacuum oven for 12 h. The crystalline VO_2 nanorods were obtained by annealing the dried VO_2 precursor at 250 °C for 10 h under vacuum.

The above-obtained crystalline VO_2 precursor and $LiOH·H_2O$ (V/Li = 3/1.05, mol mol^{-1}) were mixed in methanol under magnetic stirring for 12 h. The mixture was heated to 50 °C to evaporate methanol. The produced powder was dried at 150 °C for 12 h in a vacuum oven, and finally annealed at 450 °C for 10 h in air. Then single-crystalline LiV_3O_8 nanorods were obtained.

Polyaniline was prepared by chemical oxidation polymerization. In a typical procedure, 1.67 g aniline monomer was suspended in 50 ml distilled H_2O and stirred for 10 min to become well dispersed. Then 4.10 g ammonium persulfate (APS) in 20 ml distilled H_2O solution was slowly added to the suspension mixture. The polymerization was achieved after standing for 5 h in an iced bath, at which point the suspension becomes dark green. The products were obtained by filtering and washing the suspension with ethanol and deionized water, and then drying it under vacuum at 60 °C for 12 h.

100 mg as-prepared LiV_3O_8 nanorods were dispersed in 15 ml sodium dodecyl benzene sulfonate (SDBS) solution. Then, aniline monomer (100 mg, 200 mg, 300 mg) was added into the solution and ultrasonicated for 10 min to become well dispersed. The APS solution was then added dropwise with constant stirring to initiate the polyreaction. The reaction was carried out in an iced bath over 5 h. The final products were then filtered, washed with distilled water, and dried at 70 °C in a vacuum oven for 12 h.

6.2.2 Materials characterization

The PAn content in the composites was determined by thermogravimetric analysis (TGA) via a Setaram 92 instrument. Phase analysis was performed by powder X-ray diffraction (XRD) using a GBC MMA X-ray generator and diffractometer with Cu Kα radiation. PAn was confirmed by using a JOBIN YVON HR800 confocal Raman system with 632.8 nm diode laser excitation on a 300 lines/mm grating at room temperature. The morphologies of the samples were investigated by a field emission scanning electron microscope (SEM: JEOL JSM-7500FA).

6.2.3 Electrochemical measurements

Electrochemical measurements of the synthesized LiV_3O_8-PAn and bare LiV_3O_8 were accomplished by assembling CR2032 coin cells. The electrodes were prepared by mixing 80 wt % active materials with 10 wt. % carbon black and 10 wt. % sodium carboxymethyl cellulose (CMC) in distilled water. The slurry was uniformly pasted on to pieces of aluminium foil with an area of 1 cm^2. Such prepared electrode sheets were dried at 90 ˚C in a vacuum oven for 12 h. Then, the electrodes were compressed at a rate of about 300 KPa. Coin cells were assembled in an argon filled glove box where the counter electrode was Li metal and the electrolyte was 1 M $LiPF_6$ in a mixture of ethylene carbonate (EC) and diethyl carbonate (DEC) (EC/DEC = 1:2, v/v). The cells were cycled between 1.5 and 4.0 V at a constant current density of 0.1 C (1 C = 280 mAh g^{-1}) at room temperature to measure the electrochemical response. AC-impedance measurements and cyclic voltammetry were carried out utilizing a CHI 660B electrochemical workstation. The specific capacity is based on the weight of the LiV_3O_8 or LiV_3O_8-PAn composite material.

6.3. Results and Discussion

6.3.1 Structure and morphologies

The amounts of PAn in the LiV_3O_8-PAn composites were measured by thermogravimetric analysis (TGA). The samples were heated from 60 ˚C to 700 ˚C at the rate of 5 ˚C min^{-1}. As shown in Fig. 6.1, bare LiV_3O_8 maintains a constant weight as the temperature increases, while PAn begins to decompose around 300 ˚C and completely disintegrates at 650 ˚C. Therefore, for the composites, the main loss from 350 to 600 ˚C is

assigned to the degradation of PAn, and we can calculate that the weight contents of PAn in the composites are 5 wt. %, 12 wt. % and 23 wt. %, respectively.
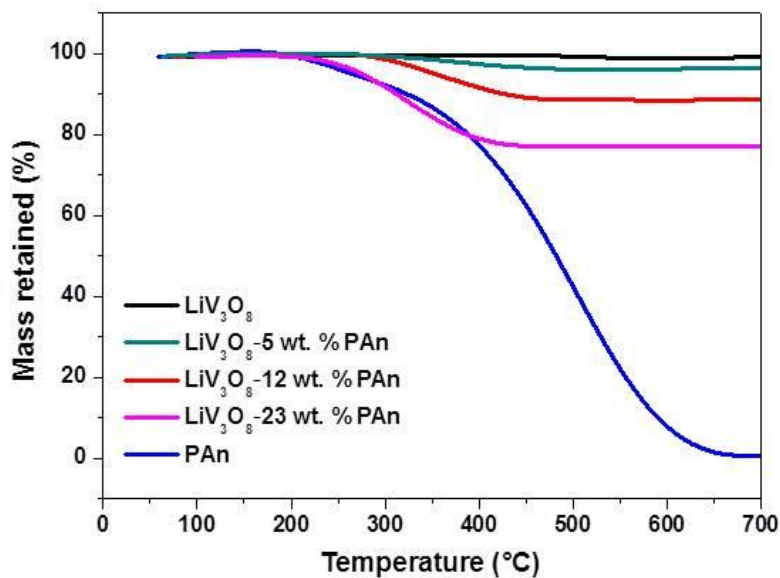
Figure 6.1 TGA curves of the PAn powder, the bare LiV_3O_8 and the LiV_3O_8-PAn composites
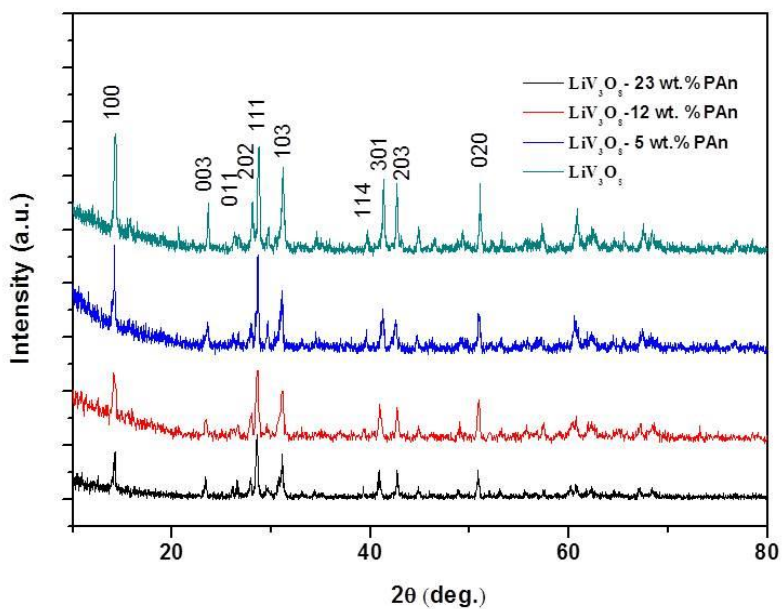
Figure 6.2 X-ray diffraction patterns of the as-prepared bare LiV_3O_8 and PAn-LiV_3O_8 composites

The X-ray diffraction (XRD) patterns of the LiV_3O_8 nanorods and the LiV_3O_8-PAn composites are shown in Fig. 6.2. All reflections of LiV_3O_8 nanostructured materials were in excellent accordance with the rutile structure (JCPDS No. 72-1193), which belongs to space group P21/m (11). The sharp and intense XRD peaks of the as-obtained LiV_3O_8 nanorods indicate their good degree of cystallinity. The peak at about 14° is assigned to diffraction at the (100) planes, indicating the layered structure of LiV_3O_8. These layers are composed of VO_6 octahedra and VO_5 trigonal bipyramids, which are corner sharing with the octahedral [252]. In addition, there was no notable peak shifting or intensity change after the introduction of PAn.
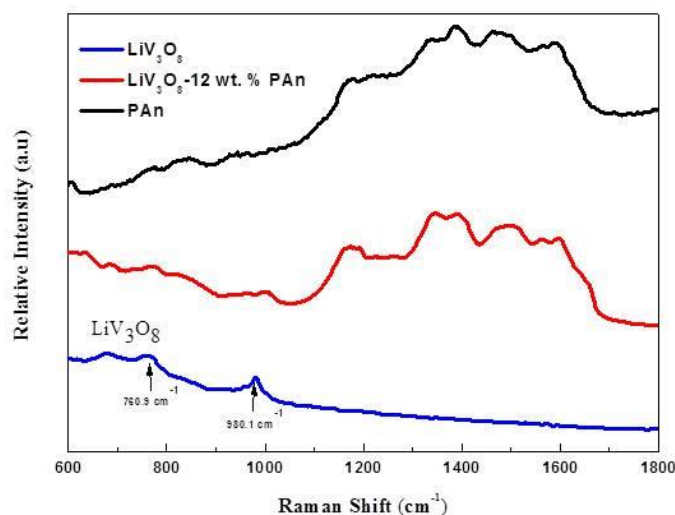
Figure 6.3 Raman spectra of the PAn, LiV_3O_8 and LiV_3O_8-12 wt. % PAn composite.

Raman spectroscopy was used to confirm the presence of PAn in the composite. Fig. 6.3 presents Raman spectra of the composites with 632.8 nm diode laser excitation on a 300 line/mm grating at room temperature. The Raman bands of LiV_3O_8 and the composites at 980.1 cm^{-1} can be assigned to the V=O stretching vibrations of VO_5 pyramids, and the band at 760.9 cm^{-1} is likely to be related to the atomic motions of corner-sharing oxygen atoms among the VO_6, VO_5, and LiO_6 polyhedra [253]. The peaks of PAn are located

between 1000 cm^{-1} and 1800 cm^{-1}, which matches up with the Raman spectrum of bare PAn [254]. This demonstrates that the LiV$_3$O$_8$ particles were combined with the PAn. No additional peaks are obvious in the Raman spectrum of LiV$_3$O$_8$-PAn, indicating that no chemical reaction between PAn and LiV$_3$O$_8$ occurred during preparation.

Typical scanning electron microscope (SEM) images of the LiV$_3$O$_8$ nanorods and the LiV$_3$O$_8$-12 wt. % PAn composite are shown in Fig. 6.4. The LiV$_3$O$_8$ nanorods are homogeneous with widths of 100-200 nm and lengths of 5.0-6.0 μm, and they have sharp edges. Figure 6.4 (b) demonstrates that the surfaces of the rods are smooth and flat, indicating complete growth of the nanorods under the experimental conditions. After the introduction of polyaniline, the LiV$_3$O$_8$-PAn composite presents a distinct contrast in the morphology. Its surface becomes rough, and the nanorod diameters increase to 200-300 nm, which confirms that the PAn is coated on the surface of the LiV$_3$O$_8$. An individual nanorod was chosen for scanning at high magnification. As seen in Fig. 6.4(e), the PAn layer provides good coverage of rod surfaces.
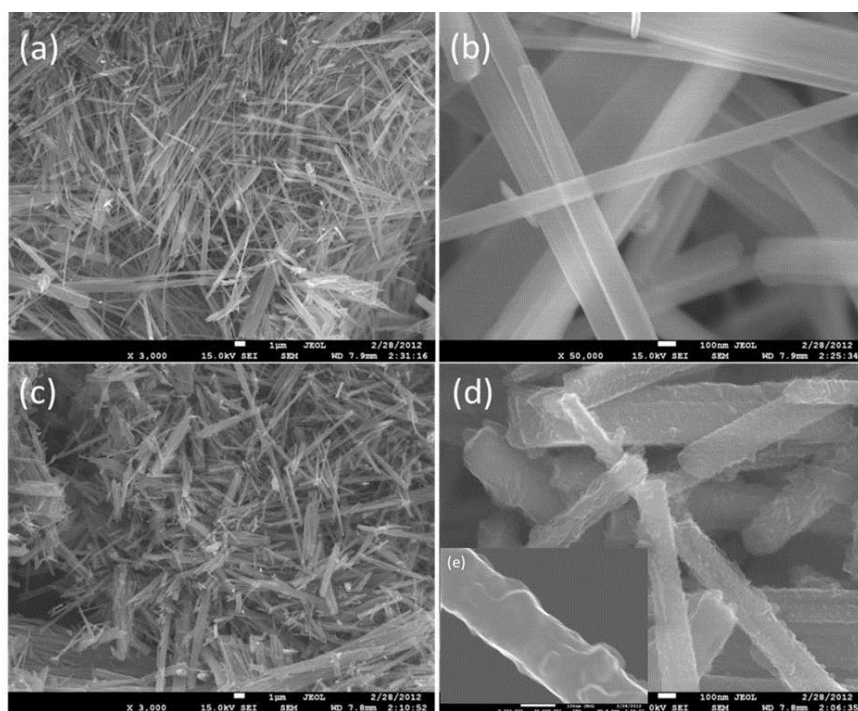
Figure 6.4 SEM images of bare LiV$_3$O$_8$ (a, b), and LiV$_3$O$_8$ - 12 wt. % PAn composite (c, d, e)

Scanning electron microscopy and energy dispersive spectroscopy (SEM/EDS) mapping of the different elements were conducted to analyse the distribution of the species within the particles (Fig. 6.5). The bright spots correspond to the presence of the elements N, V, and O, respectively, in which N is the element found only in PAn. Element N is distributed uniformly throughout the whole area, which indicates that the PAn has uniformly coated the surfaces of the LiV_3O_8 nanorods.
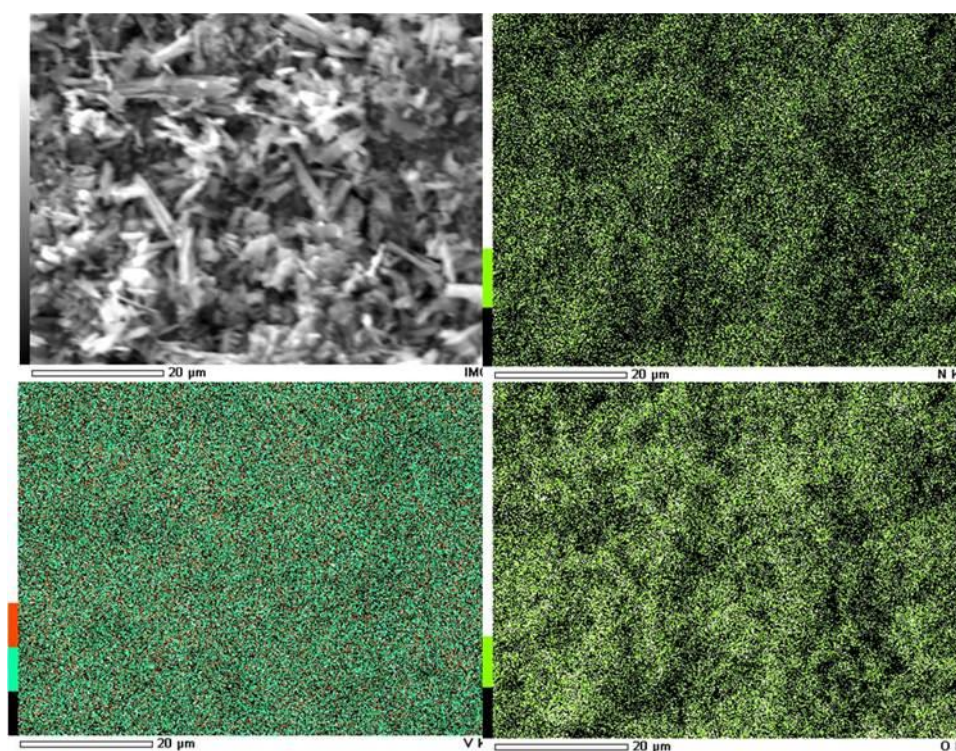
Figure 6.5 SEM image (upper left) and chemical maps of N, V, and O for the 12 wt. % PAn-LiV_3O_8 composite powder.

6.3.2 Electrochemical characterization

The 1st, 2nd, 5th, 50th, and 100th cycle voltage vs. specific capacity curves for the LiV_3O_8 and LiV_3O_8-12 wt. % PAn cells are presented in Fig. 6.6. From the charge-discharge curves of the samples, it can be seen that LiV_3O_8-PAn composite has higher capacity and

superior stability in comparison with the bare LiV_3O_8 over 100 cycles. The pure LiV_3O_8 shows multistep processes in its charge and discharge curves, which are the same as those in previous reports [55, 198, 255]. The first specific discharge capacity of the composite is lower than in subsequent cycles, which is probably due to the activation of PAn in the charge-discharge process. This phenomenon will be discussed below.
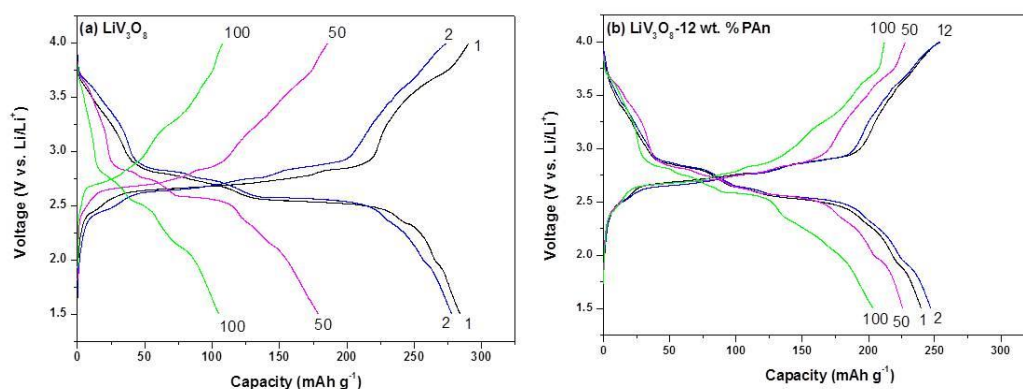
Figure 6.6 Charge-discharge curves for selected cycles of LiV_3O_8 (a) and LiV_3O_8-12 wt. % PAn (b) at 0.1 C.

Cyclic voltammograms of electrodes made from LiV_3O_8, composite and PAn are shown in Fig. 6.7. The first cycle voltammograms are rather different from the rest, indicating that some structural modifications have probably taken place during the first charge and discharge operations. There are four anodic peaks at 2.48 V, 2.79 V, 2.85 V, and 3.69 V for the bare LiV_3O_8 electrode, which is related to the deinsertion of Li^+. The main cathodic peaks of the bare LiV_3O_8 are at 1.90 V, 2.50 V, 2.74 V, 2.81 V and 3.63 V. The cathodic peak observed around 2.50 V could be attributed, based on the literature, to the two-phase transformation of $Li_3V_3O_8/Li_4V_3O_8$ [252, 256, 257], while the other peaks correspond to individual phase transformations [22, 23]. After the introduction of PAn, the two anodic peaks at 2.81 V and 2.74 V cannot be separated anymore, the two peaks were merged into one broad peak at 2.82 V as a broad oxidation peak exists in PAn between 2.5 and 3.4 V

102

(see Fig. 6.7C). In addition, the anodic peak at 2.48 V becomes broader and appears as a shoulder in the foot of peak at 2.82 V.
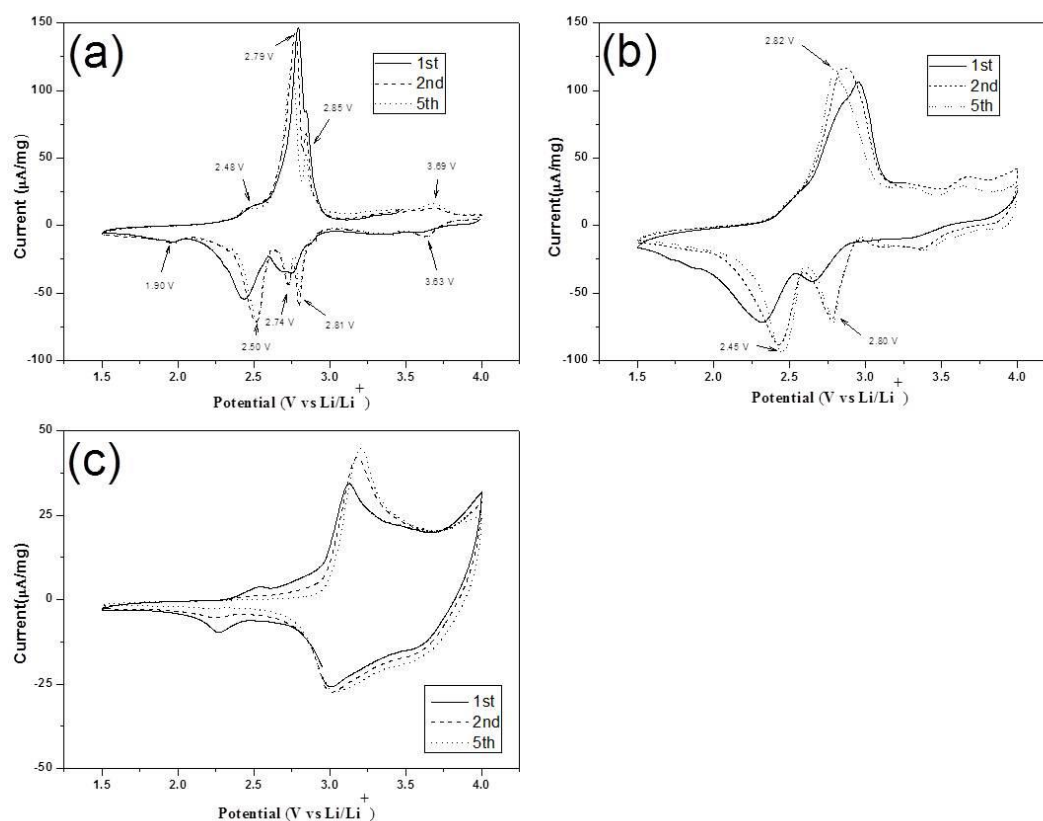
Figure 6.7 Cyclic voltammorgrams for selected cycles of the electrodes made from: (a) bare LiV$_3$O$_8$, (b) LiV$_3$O$_8$-12 wt. % PAn, (c) bare PAn. Scanning rate: 0.1 mV s^{-1}

Figure 6.8(a) presents the specific discharge capacity of the electrodes prepared from LiV$_3$O$_8$/PAn composites, bare LiV$_3$O$_8$, and PAn, with cycling at 0.1 C. The first specific discharge capacity of PAn powder is lower than for subsequent cycles, which is probably due to its gradual activation in the first discharge process [85]. After that, the capacity of PAn becomes steady and is maintained at 62 mAh g^{-1} over 100 cycles, indicating that it is electroactive in the range of 1.5-4.0 V. The bare LiV$_3$O$_8$ electrode shows an initial capacity of 283 mAh g^{-1}. This is higher than the initial capacities of the composite electrodes, which are 186 mAh g^{-1} for LiV$_3$O$_8$-23 wt. % PAn, 243 mAh g^{-1} for LiV$_3$O$_8$-12

wt. % PAn and 260 mAh g^{-1} for LiV$_3$O$_8$-5 wt. % PAn. However, the capacity of bare LiV$_3$O$_8$ continuously decreases and declines to 108 mAh g^{-1} over 100 cycles, which is only about 38 % of the initial capacity, indicating poor cycling performance. Interestingly, the discharge capacities of all the composites first increase and then reach a maximum capacity at the fifth cycle, which should be attributed to the activation of PAn. The capacity of LiV$_3$O$_8$-5 wt. % PAn reaches 130 mAh g^{-1} after 100 cycles. The composite with 12 wt. % polyaniline presents the best cycling stability, showing a specific discharge capacity of 204 mA g^{-1} after 100 cycles. This excellent electrochemical performance is comparable what was reported for LiV$_3$O$_8$/polypyrrole (183 mAh g^{-1} after 100 cycles) [198]. Further increase of PAn content in the composite would reduce the specific capacity of the composite electrode because the practical capacity of PAn is only 60 mAh g^{-1}, which is much lower than that of LiV$_3$O$_8$. The first cycle coulombic efficiency of bare LiV$_3$O$_8$ is 90.9 % and that for the following cycles around 95 %. After 16 cycles, the coulombic efficiency reaches 98.0 %. The LiV$_3$O$_8$-12 wt. % PAn electrode showed a higher first cycle efficiency of 91.0 %, and maintained a steady value of 98 % after the first 8 cycles. We believe that the low coulombic efficiency of bare LiV$_3$O$_8$ in the first few cycles is mainly due to its low conductivity.

The composite with 12 wt. % PAn was chosen to test the cycling performance at different charge/discharge rates in comparison with bare LiV$_3$O$_8$. The electrode capacities were measured after 5 cycles at each rate from 0.2 C to 4 C in an ascending order, followed by a return to 0.2 C. The results are shown in Figure 6.8 (c). The composite presents excellent cycling stability at each rate, and the capacities are measured to be 230 mAh g^{-1} at 0.5 C, 201 mAh g^{-1} at 1C, 180 mAh g^{-1} at 2 C, and 152 mAh g^{-1} at 4 C. On returning to 0.2 C, the composite electrode delivers 250 mAh g^{-1}, which is much better than the performance of the bare LiV$_3$O$_8$ electrode (184 mAh g^{-1}). The high-rate performance is

even better than that of LiV_3O_8/carbon nanosheets (110 mAh g^{-1} at 5 C and 173 mAh g^{-1} at 0.5 C) [54].
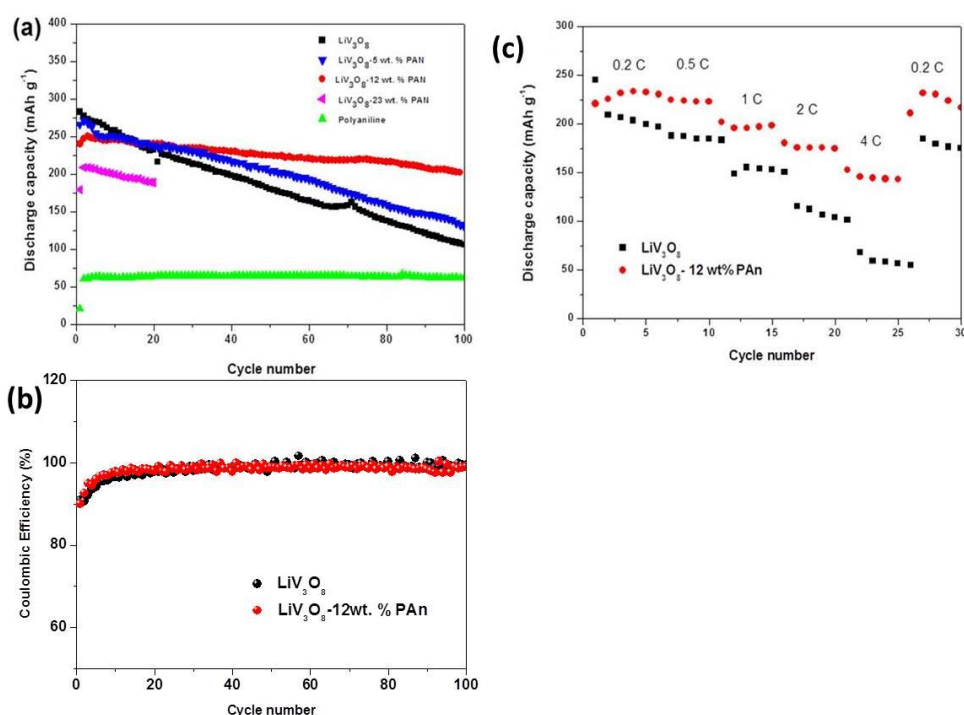
Figure 6.8 (a) Cycle life of as-prepared LiV_3O_8 nanorods and LiV_3O_8-PAn composites at 0.1 C (1 C = 280 mAh g^{-1}). (b) Coulombic efficiency of LiV_3O_8 and LiV_3O_8-12 wt. % PAn composite at 0.1 C. (c) Rate capabilities of LiV_3O_8 and LiV_3O_8-12 wt. % PAn composite with changing current densities from 0.2 C to 4 C and back to 0.2 C between 1.5 V and 4.0 V vs. Li/Li$^+$.

In order to explore the reasons for the good cycling performance of the composites, electrochemical impedance spectroscopy (EIS) was performed on the electrodes made from the as-obtained materials in the fully discharged state, and the results are presented in Fig. 6.9. The impedance curves show one compressed semicircle in the medium-frequency region, which could be assigned to charge transfer resistance (R_{ct}), and inclined line in the low-frequency range which could be considered as Warburg impedance. The values of R_{ct} for the LiV_3O_8 and the composite electrodes are 301 and 504 Ω,

respectively, indicating that the PAn coating can significantly increase the electrical conductivity between LiV_3O_8 nanorods.

A morphological study of the electrodes before cycling and after 100 cycles was also conducted (Fig. 6.10). Fig. 6.10 (b) is a SEM image showing the surface of the LiV_3O_8 after 100 cycles, where big cracks can be clearly observed on the surface of the electrode. For the LiV_3O_8-PAn composite electrode (Fig. 6.9(d)), however, the cracks are not obvious, the integrity of the electrode is retained, and the cell just shows slight
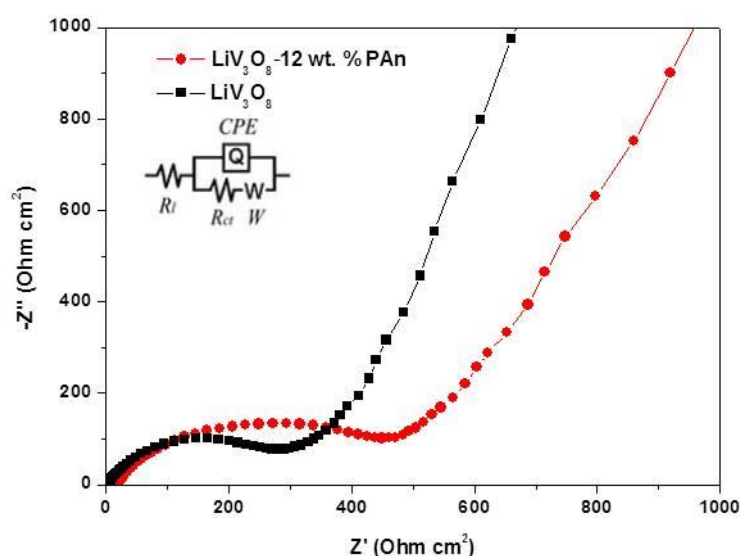
Figure 6.9 Nyquist impedance plots of the bare LiV_3O_8 and the LiV_3O_8-12 wt. % PAn composite electrodes after 100 cycles. The inset shows the equivalent circuit.

Table 6.1 Fitting result for EIS data on pristine LiV_3O_8 and LiV_3O_8-12 wt. % PAn composite electrodes after cycling.

	R_l (Ω)	R_{ct} (Ω)
LiV_3O_8	1.3	301
LiV_3O_8-12 wt. % PAn	5.6	504
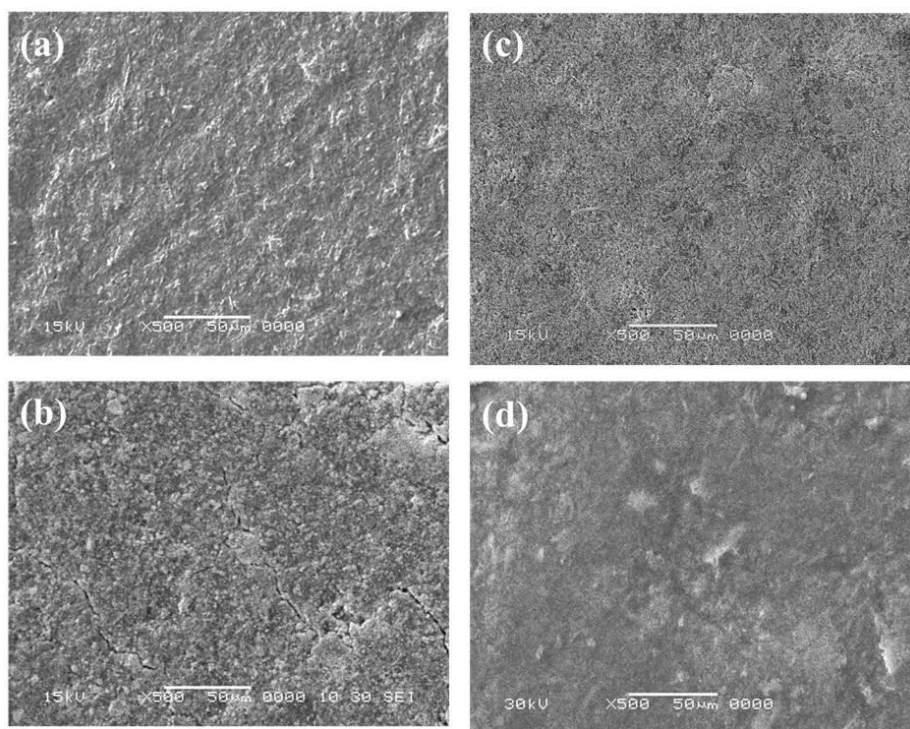
Figure 6.10 SEM images of electrode surfaces of LiV_3O_8 (a, b) and LiV_3O_8- 12 wt % PAn composite (c, d) before (a, c) and after (b, d) 100 cycles.

agglomeration compared to the electrode before cycling (Figure 6.10 (a, c)), suggesting good structural stability of the composite electrode. This excellent stability of theelectrode may be attributed to the presence of the well-dispersed PAn coating on the LiV_3O_8 powders. The LiV_3O_8 structural changes during charging/discharging could be buffered by the presence of PAn. Moreover, PAn could prevent cracking and pulverization of the LiV_3O_8 electrode. At the same time, PAn can also acts as a conductive element by contributing its electroactivity, resulting in an increase in the storage capacity. Therefore, by coating with PAn, enhanced cycling stability and good high rate performance can be achieved.
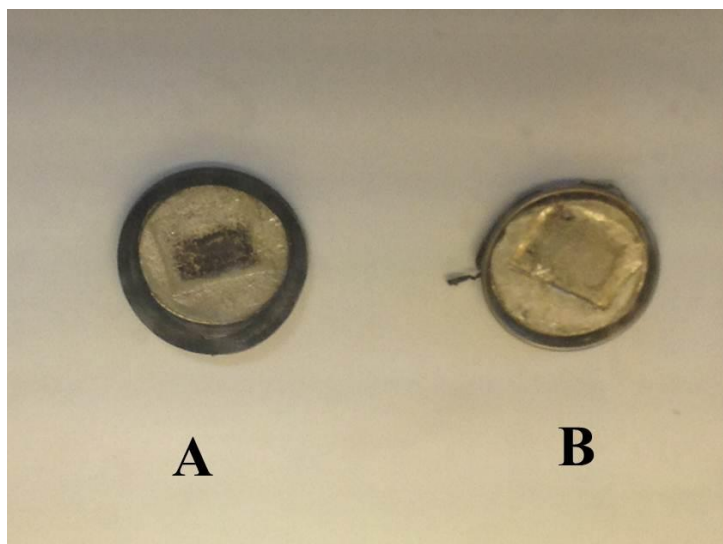
Figure 6.11 The lithium anode in the cells of LiV_3O_8 (A) and LiV_3O_8- 12 wt. % PAn (B) after 100 cycles.

The cells were opened after 100 cycles to observe any differences on the lithium anode surface. Some black material was found on the surface of the lithium metal in the bare LiV_3O_8 cells (Fig. 6.11). This is due to dissolution of the LiV_3O_8 particles into the electrolyte, which then migrated to the lithium anode through the separator via the electrolyte, where the reduction of vanadium ions took place. In this regard, it is expected that the dissolved vanadium complexes would be deposited on the surface of the lithium anode, which would induce a dramatic impedance rise in the cells. In contrast, the lithium foil in the composite material cell shows no such change, indicating that a uniform PAn coating on the surface of the LiV_3O_8 is an effective way to improve the cycling stability by preventing the vanadium dissolution.

6.4 Summary

LiV_3O_8 nanorods coated with conducting polyaniline are prepared by a simple chemical method. With 12 wt. % PAn coating, although a high initial discharge capacity could not

be obtained, improved cycling performance and substantially improved high rate capacity have been demonstrated. This excellent electrochemical performance can be attributed to the buffering action of PAn, preventing the dissolution of active material in the electrolyte and promoting good electrical conductivity compared to bare LiV_3O_8.

Chapter 7   Improving the Electrochemical Performance of LiNi0.5Mn1.5O4 Spinel by Polypyrrole Coating as Cathode Material for Lithium-ion Battery

7.1 Introduction

Recently, Rechargeable LIBs have been intensively pursued for hybrid electric vehicle (HEV) and electric vehicle (EV) application [8, 174]. Unfortunately, the conventional LIBs based on graphite anode and $LiCoO_2$ cathode only provide an energy density of 400 Wh kg^{-1} [258], which can hardly meet the requirements of high energy storage for EVs. One effective way to enhance the energy and power densities of the LIB is to increase its operating voltage. As a consequence, extensive research has been conducted on developing novel cathode materials with high cutoff voltage to replace commercial $LiCoO_2$ (~ 3.7 V). $LiMn_2O_4$ has been reported as a very promising cathode candidate due to its economic and environmental advantages [259]. In particular, the addition of partial cation replacement of Mn by a transition metal, M (M = Cr, Co, Fe, Ni, and Cu), in the spinel oxides $LiMn_{2-x}M_xO_4$ can further increase the cell operating voltage and provide stability for the crystal structure [260, 261]. Among these elements, since the redox couples of Ni^{4+} to Ni^{2+} are located at ~ 4.75 V in the spinel $LiNi_{0.5}Mn_{1.5}O_4$ (LNMO), the energy density of this material can reach a very high value of 658 Wh kg^{-1}, which considerably exceeds that for pristine $LiMn_2O_4$ (440 Wh kg^{-1}) [262, 263]. In this regard, LNMO is currently

considered as one of the most promising high voltage cathodes for future LIBs to meet the demands of electric vehicle applications.

Despite the promise of the LNMO cathode material, there still exist multiple fundamental material challenges that prevent its commercialization. Firstly, the major charge/discharge reactions of LNMO take place up to ~ 4.7 V (vs. Li/Li$^+$), which would be an advantage if it were not beyond the stability potential (~ 4.5 V) of conventional electrolyte [264]. The electrolyte is not stable against oxidation at such high potential, which may result in the formation of the formation of a detrimental solid electrolyte interphase (SEI) layer, hindering the insertion/extraction of Li$^+$ ions, which leads to capacity fade and poor cycle life. In addition, the common impurity Mn^{3+} in LNMO is inclined to form Mn^{2+} during cycling due to its Jahn-Teller distortion[265]. The Mn^{2+} ion is reported to have a tendency to dissolve into the electrolyte and be further deposited on the surface of the anode, with the deposition subsequently increasing the impedance of the battery and causing potential energy losses [266]. Recently, Benedek and Thackeray proposed that trace amounts of HF in the electrolyte may also cause Mn dissolution[267]. In the LNMO spinel, the Mn and Ni dissolution reaction in the presence of HF can be proposed as follows:

$$2LiNi_{0.5}Mn_{1.5}O_4 + 4H^+ + 4F^- \rightarrow 3Ni_{0.25}Mn_{0.75}O_2 + 0.25NiF_2 + 0.75MnF_2 + 2LiF + 2H_2O$$

$$(7.1)$$
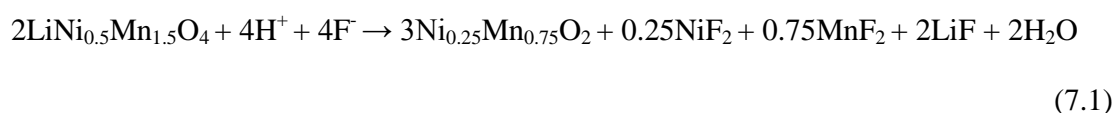
At elevated temperature, these undesirable processes are accelerated, which significantly limits the practical application of LNMO as cathode material in the LIB[268, 269].

In order to overcome these obstacles, surface modification of the LNMO with a protective layer has been proved to be an effective approach. Previously, the effects of some metal oxides used for the coating, such as ZnO [270, 271], Al$_2$O$_3$ [272], Bi$_2$O$_3$ [273], Co$_3$O$_4$ [274] and TiO$_2$ [266], have been investigated and were found to have enhanced the electrochemical

performance at both room and elevated temperature. These metal oxide layers can provide a protective skin to control interfacial side reactions and decrease the amounts of Ni and Mn dissolution. Meanwhile, coating with some cathode materials, $Co_2O_3/LiCoO_2$ [274], $LiFePO_4$ [275] and $FePO_4$ [276], has also yielded great improvement in the cycling stability of LNMO. Unfortunately, because the conductivity of these inorganic materials is relatively low, there is no dramatic change in Li^+ diffusivity, and these coatings even make the high-rate performance of the composite worse than that before the coating [277]. In addition, the metal oxides tend to be discontinuously deposited onto the LNMO, which leads to the limited coverage of the LNMO surface. Conductive carbon coating is reported as another strategy[278, 279], but this approach is still difficult to apply to LNMO since a reducing atmosphere is needed for a carbon source to carbonize at high temperature, and the Mn^{4+} in LNMO is easily reduced to Mn^{3+} by carbon. In this regard, it is important to find another novel coating material which can act as both a protective and conductive layer for LNMO.

In recent years, conducting polymers have been considered as another type of potential additive to improve cycling stability and rate performance in lithium ion batteries. Conducting polymers have been reported to be a stable wrapping layer during the charge-discharge process for some promising cathode materials, such as $LiFePO_4$ [79], LiV_3O_8 [280], $LiMn_2O_4$ [281, 282] and $LiCoO_2$ [283]. Cho et. al. [284] demonstrated that polyimide (PI) coating, deposited on the surface of LNMO by thermally curing 4-component polyamic acid, featured a highly continuous surface coverage with nanometre thickness. The PI wrapping layer acted as a novel ion-conductive protective skin to buffer the unwanted side reactions occurring on the LNMO surface, as well as Mn dissolution in the electrolyte. Nevertheless, the composite still presented a low discharge capacity at very high current densities, such as 5 C and 10 C, which was attributed to the additional electronic

112

resistance caused by introducing PI layer at high discharge current densities. Therefore, it is still worthwhile to explore the use of new polymers to increase the conductivity of LNMO. Among various conductive polymers, polypyrrole (PPy) has been used extensively because it is less toxic compared with other conducting polymers and can be easily produced with the desired morphology by chemical reaction. Through *p*-doping, the electrical conductivity of PPy can reach the level of a few tenths of S/cm [71, 208]. In our previous study, PPy has been proved to not only be able to protect the surface of the electrode, but also serve as a conductive matrix for the active material [112, 124, 190]. Herein, we have prepared submicron-sized LNMO with PPy coating via simple chemical oxidative polymerization in an aqueous solution. The electrochemical properties of LNMO-PPy as cathode material in Li-ion batteries were systematically investigated.

7.2 Experimental

7.2.1 Material synthesis

Synthesis of $MnCO_3$ microspheres: In a typical reaction, $MnSO_4 \cdot H_2O$ (14 mmol) and NH_4HCO_3 (140 mmol) were separately dissolved in water (100 mL). 20 mL of ethanol was then added into the above $MnSO_4$ solution under stirring and cooled down to 4 ˚C. After complete dispersion, the NH_4HCO_3 solution was quickly added into the mixture and then a white precipitate could be observed. The mixture was continued then kept at 4 ˚C for 2 h. Then, the white precipitate was collected by filtration, washed with water and anhydrous ethanol three times, and dried at 80 ˚C under vacuum for 12 h.

Synthesis of bare LNMO: Stoichiometric proportions of as-prepared porous $MnCO_3$ microspheres, $Ni(NO_3)_2 \cdot 6H_2O$, and the eutectic molten-salt[285] of 0.62:0.38 (mol/mol)

LiNO$_3$ and LiOH·H$_2$O were dispersed in ethanol under continuous stirring. After evaporation at 50 ˚C for 1 h, the mixture was put into a muffle furnace for calcination at 230 ˚C for 3 h, and then the temperature was raised to 800 ℃ for 20 h to obtain the product.

Synthesis of LNMO-PPy composite: 100 mg of the as-prepared LNMO material was dispersed in 10 mL aqueous solution. Then, a 3:1 (mol/mol) mixture of pyrrole monomer (5mg, 7 mg, 10 mg) and p-toluenesulfonyl sodium were added into the solution and ultrasonicated for 10 min to become well dispersed. FeCl$_3$ solution (100 mg in 10 mL water) was then added dropwise under constant stirring to initiate the polyreaction. The reaction was carried out in an iced bath over 12 h. The final products were then filtered, washed with distilled water, and dried at 60 ℃ in a vacuum oven for 12 h.

7.2.2 Materials characterization

Thermogravimetric analysis (TGA) was carried out on a METTLER TGA system via a Setaram 92 instrument to determine the PPy content. The phase of the samples were investigated by on powder X-ray diffraction (XRD) using a GBC MMA X-ray generator and diffracto-meter with Cu Kα radiation. The morphologies of the samples were observed using scanning electron microscopy (SEM, JEOL JSM-7500FA, equipped with a JEOL energy dispersive spectroscopy (EDS) system). Transmission electron microscopy (TEM) analysis was performed on a JEOL 2100 analytical instrument, operating at 200 keV. The presence of PPy was confirmed by using a JOBIN YVON HR800 confocal Raman system with 632.8 nm diode laser excitation on a 300 lines/mm grating at room temperature. The specific surface areas were determined by the Brunauer-Emmett-Teller technique (BET, Quanta Chrome Nova 1000).

7.2.3 Electrochemical characterization

The electrochemical experiments were performed on CR2032 cells. Lithium sheets were used both as counter electrode. A fleece separator was soaked with 1 M $LiPF_6$ in 3:7 ethylene carbonate: diethyl carbonate (v/v). The cells were assembled in an argon-filled glove box where both moisture and oxygen levels were kept below 1 ppm. They were cycled in the voltage range between 3.5 V and 4.9 V in various current densities at room and elevated temperature. AC-impedance measurements were carried out utilizing a CHI 660B electrochemical workstation. The specific capacity is based on the weight of the LNMO or LNMO-PPy composite material.

7.3 Results and Discussion

7.3.1 Physicochemical characterization

The PPy content in the composite was determined by thermo gravimetric analysis. The samples were heated from 50 ˚C to 600 ˚C at a rate of 10 ˚C min^{-1}. As shown in Fig. 7.1(a), the PPy powder begins to decompose around 200 ºC and completely disintegrates at 500 ºC. The enlargement of the bare LNMO and LNMO-PPy composites over the range from 90% to 100% retained mass is the inset in Fig. 7.1(a), which indicates that the bare LNMO maintains a constant weight as the temperature increases. Therefore, the PPy contents in the composites are calculated to be 3 wt. %, 5 wt. %, and 8 wt. %, respectively.
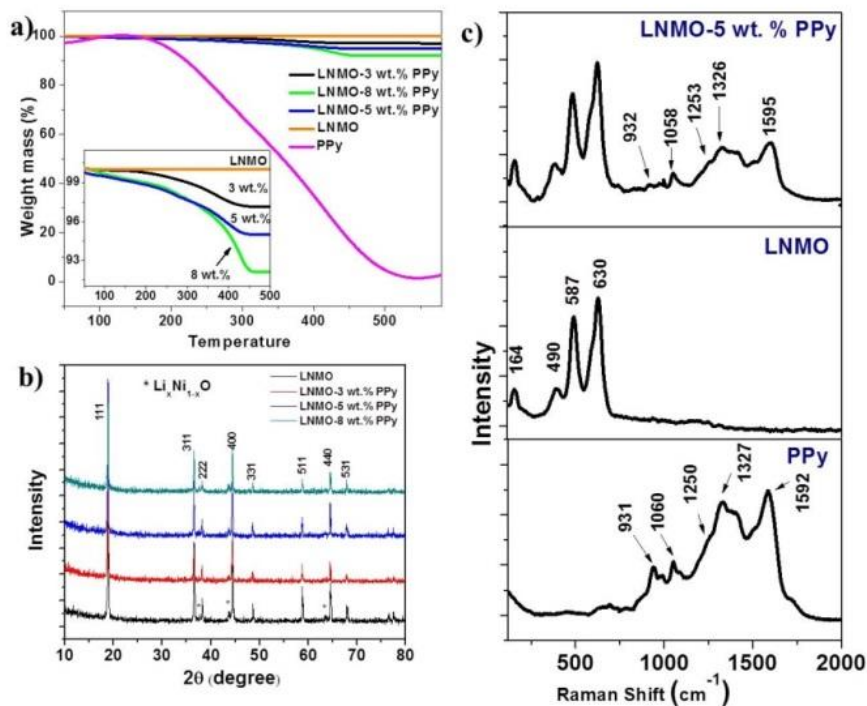
Figure 7.1 TGA curves, with the inset showing an enlargement of the indicated region (a) X-ray diffraction patterns (b), and Raman spectra (c) of the samples.

The X-ray diffraction (XRD) patterns obtained from the bare LNMO and the LNMO-PPy composites are displayed in Fig. 7.1(b). The pattern of the bare LNMO corresponds to the cubic spinel structure (space group = Fd3m, JCPDS #32-0581). Very weak peaks, corresponding to $LiNi_{1-x}O_2$, are detected on the left shoulders of the peaks for the (400), (222) and (440) planes. This impurity is believed to originate from the oxygen loss in the samples at high annealing temperatures above 750 ˚C [286]. No substantial difference in the XRD patterns between the bare and PPy-coated LNMO composites was observed, demonstrating that the introduction of the PPy wrapping layer does not degrade the spinel crystalline structure of LNMO.

Raman spectroscopy confirmed the presence of PPy in the LNMO composites [Fig. 7.1(c)]. The bare LNMO exhibits characteristic bands located at 630 cm^{-1}, 498 cm^{-1}, and

164 cm^{-1} in the Raman spectrum[24]. The Raman spectrum of the as-prepared PPy displays the vibrational band characteristic of the oxidized state at 1592 cm^{-1}, related to a mixed vC=C and inter-ring vC-C vibration of short conjugation lengths, while the bands at 1327, 1253, 1060 cm^{-1}, are assigned to the ring deformation mode (δ_{ring}) and the 931 cm^{-1} band is related to C-H out-of-the-plane deformation [202]. The presence of similar oxidized PPy bands in the Raman spectra of LNMO-5 wt. % PPy composite indicates that no chemical reaction between PPy and LNMO occurred during preparation.
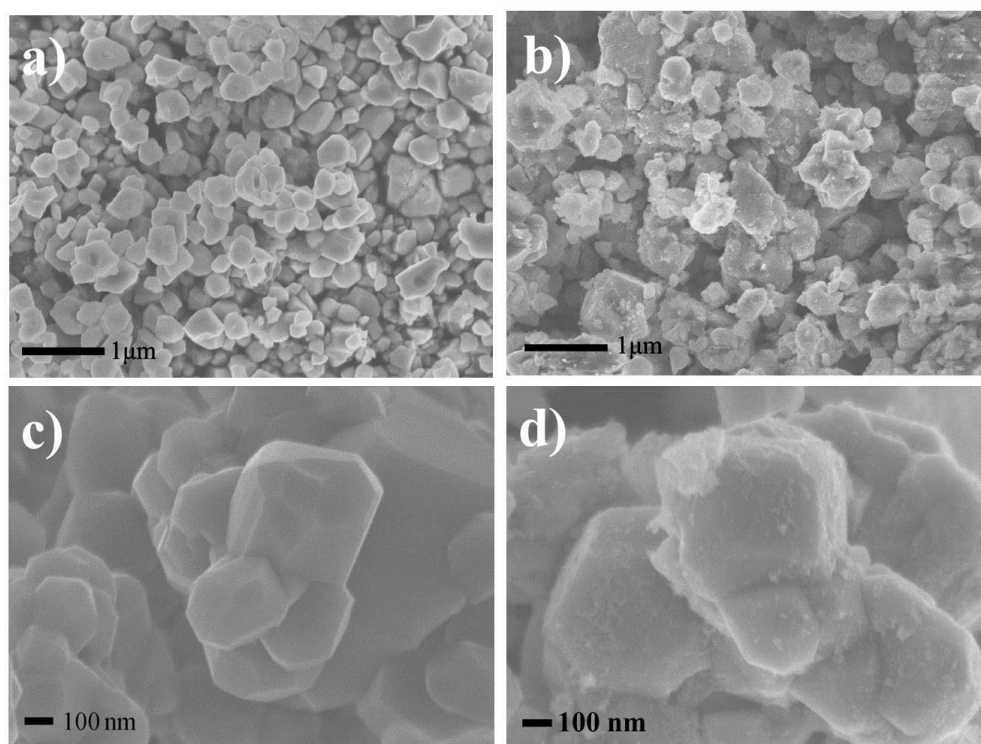
Figure 7.2 FESEM images of bare LNMO (a, c) and LNMO-5 wt. % PPy (b, d) at various magnifications

The morphologies of the bare LNMO and LNMO-5 wt. % PPy were characterized by field emission scanning electron microscopy (FESEM). The low-magnification SEM image [Fig. 7.2(a)] reveals that the size of the LNMO particles is around 200-500 nm. A very clean and smooth surface of the bare LNMO can be seen in Fig. 7.2(c) at high magnification. In comparison, a relatively rough surface for the LNMO-5 wt. % PPy

composite was observed [Fig. 7.3(d)]. This indicates that a relatively uniform PPy layer had been coated successfully onto the outer surface of the LNMO.
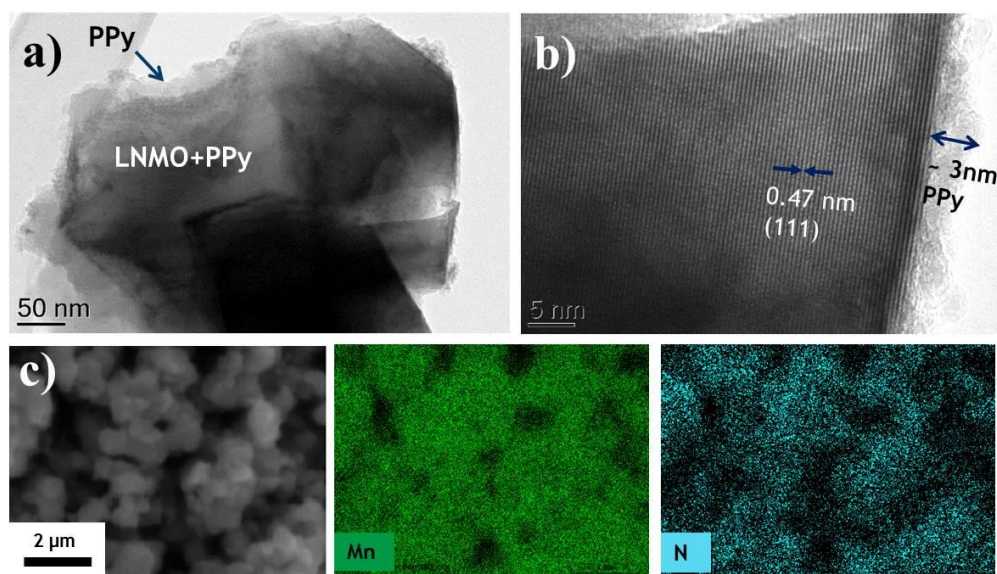
Figure 7.3 TEM (a) and high resolution TEM (b) images of LNMO-5 wt. % PPy. SEM image and elements maps (c) of Mn and N for the LNMO-5 wt. % PPy composite.

Examination by transmission electron microscopy of LNMO-5 wt. % PPy [Fig. 7.3(a, b)] confirmed the presence of a uniform PPy coating on all particles [Fig. 7.3(a)]. The crystal plane spacing of 0.47 nm indicated in the high resolution image, Fig. 7.3(b), is consistent with the LNMO (111) plane. The TEM data in Fig. 7.3(b) also demonstrates that the porous PPy layer is around 3 nm in thickness, which may resulted in high surface area for the composite. This is demonstrated by the high surface area determined by Brunauer-Emmett-Teller (BET) gas adsorption/desorption of the PPy-coated composites. The surface areas are 25, 30, 32 and 35 m^2g^{-1} for the bare, 3 %, 5 % and 8 wt. % PPy coated samples, respectively.

Fig. 7.3(c) presents the energy dispersive X-ray spectroscopy (EDX) mapping of LNMO-5 wt. % PPy under SEM (with the SEM image on the bottom left side showing the mapping area). Within the resolution limit, EDS mapping of positions of the element N,

which corresponds to PPy, appears uniform, with the N close to the positions of the element Mn. This again confirms that the LNMO particles were uniformly wrapped up in the PPy layer.

7.3.2 Electrochemical properties

Figure 7.4 1st, 100th and 200th cycle charge/discharge curves of LNMO (a), LNMO-3 wt. % PPy (b), LNMO-5 wt. % (c), and LNMO-8 wt. % PPy (d) at 1.0 C and room temperature (25 °C).

The electrochemical performances of the as-prepared samples were examined in the voltage range between 3.5 V and 4.9 V vs. Li/Li^+ at the rate of 1.0 C (1 C=140 mA/g) up to 100 cycles at room temperature (25 °C). Figure 7.4(a) shows the voltage profiles of the electrochemical cells in the range between 3.5 V and 4.9 V at a rate of 1.0 C. The first, 100th, and 200th charge-discharge curves of bare and surface modified LNMO with various contents of PPy are shown in Fig. 7.4(a). Two high-voltage plateaus were

119

observed at 4.70 V and 4.75 V, which can be associate with the $Ni^{3+/2+}$ and $Ni^{4+/3+}$ formal couples in LNMO [284, 286]. There is a small cathodic plateau located at 4.1 V, which is attributed to the $Mn^{3+/4+}$ couple [262]. No other peak is observed in Fig. 7.4(a), indicating that PPy does not lead to extra redox reactions in the tested voltage range, which means the PPy remains stable during cycling and does not contribute to the discharge capacity. We also noticed that as the content of PPy coating increases, the polarization gap in the initial cycle becomes more apparent. This is probably because the thicker PPy layer would separate the active material from the electrolyte, but as the cycle number increases, better wetting of the active material by the electrolyte is achieved. Accordingly, the discharge capacities of the composites increase in the first few cycles.
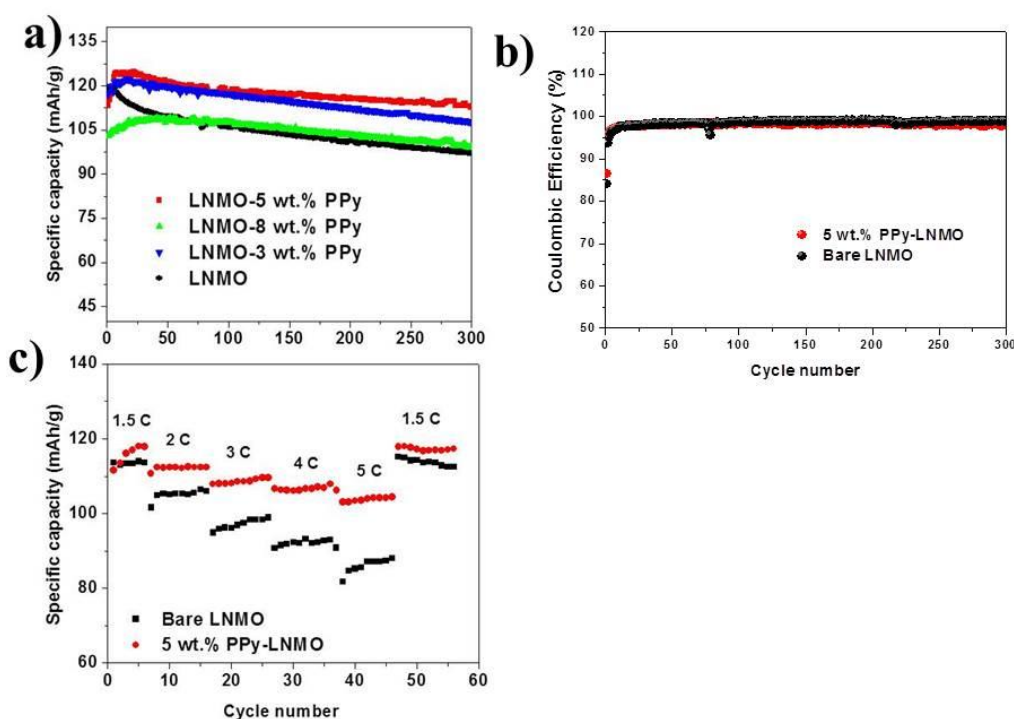
Figure 7.5 Electrochemical performance of bare LNMO and LNMO-PPy composite electrodes cycled between 3.5 V and 4.9 V at room temperature vs. Li/Li$^+$ (25 ℃): a) cycle life of LNMO and LNMO composites at the 1.0 C rate; b) coulombic efficiency of LNMO and LNMO-5wt.% PPy at the 1.0 C rate; c) rate capabilities of LNMO and LNMO-5wt. % PPy electrodes.

Figure 7.5(a) compares the cycling performances of the bare LNMO and LNMO-PPy electrodes at the 1 C rate and room temperature (25 ˚C). The bare LNMO delivers a discharge capacity of 116 mAh g^{-1} at the first cycle. After that, the discharge capacity continuously decreases and drops to 94 mAh g^{-1} after 300 cycles, and only 76.7 % capacity retention is achieved. In contrast, reversible discharge capacities of 107.4, 112.9, and 99.1 mAh g^{-1} can be retained for composites with 3 %, 5 %, and 8 % PPy over 300 cycles at room temperature, corresponding to the respective capacity retentions of 83.2%, 91.0 % and 85.7 %. This confirms that the discharge capacities in the first few cycles of the LNMO-PPy electrodes are lower than for the bare LNMO electrode, which is probably due to an active process for the PPy-coated composites. This active process that occurs in the coated samples is attributed to the slow wetting of electrolyte as it infiltrated into the porous battery electrode, with the result that the active material not charge/discharge enough initially. The first cycle coulombic efficiencies are 84.1 % and 86.4 % for bare LNMO and LNMO-5 wt.% PPy respectively. Afterwards, the efficiencies increase rapidly to a high level during cycling (97 % for cycles 5-20, 98-99 % for cycles 21-300). This can be attributed to the fact that, although the PPy coating can improve the cycling performance, it still has no obvious effect towards increasing the coulombic efficiency of LNMO at room temperature.

The composite with 5 wt. % PPy was chosen to test the rate capability, and it showed high Li^{+} storage at high current density as well [Fig. 7.5(c)]. For testing, the cell was first discharged/charged at the current density of 1.5 C for 6 cycles, and then at various current densities from 2.0 C to 5.0 C for 10 cycles each, before finally returning to 1.5 C. The reversible capacities are 105, 98, 92, and 85 mAh g^{-1} at 2.0, 3.0, 4.0, and 5.0 C, respectively. When the rate returned to 1.5 C, the specific capacity can be recovered up to 117 mAh g^{-1}, indicating a very stable cycling performance. In comparison, the bare

LNMO shows relatively poor capability at large current densities. It is accepted that the electrochemical performance at high rate is largely dependent on the electrical conductivity of the active material. Therefore, this superior electrochemical performance of LNMO-PPy should be ascribed to the high conductivity of the PPy layer. Herein, we should point out the performance of our PPy coating sample compares favorably with some other reports in the literature. As mentioned above, some common inorganic materials, have been proved to only work as a protective layer on the surface of active material, but cannot enhance the rate capabilities for LNMO[266, 271]. On the other hand, carbon coating only leads to limited improvement [279], while other polymer coatings, such as polyimide [284], even made the battery performance worse than before at 5 C and 10 C.
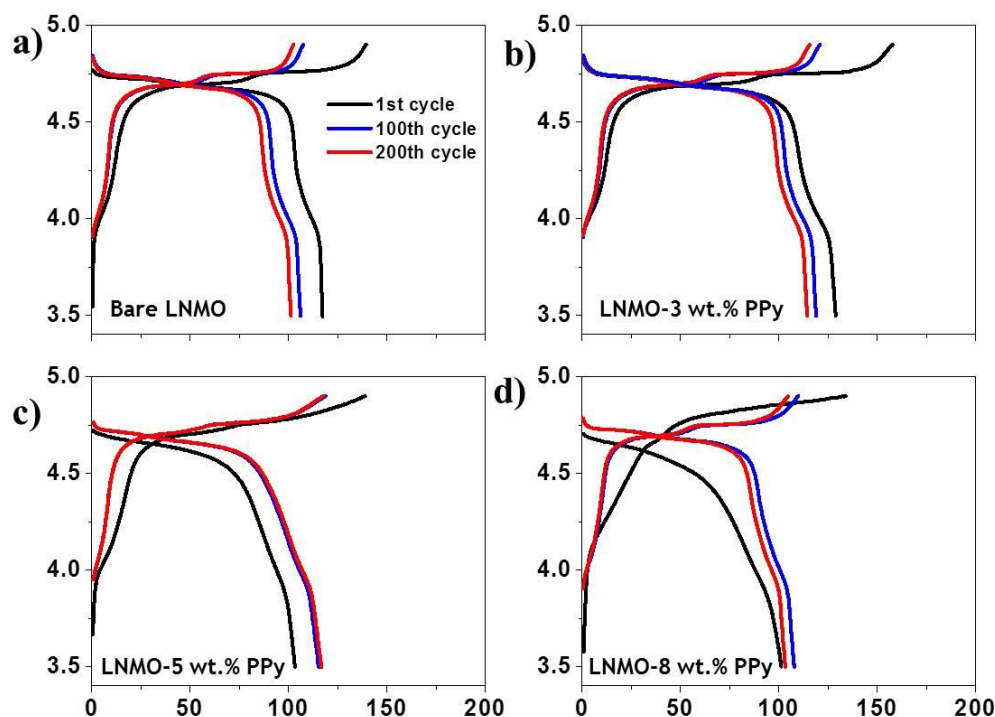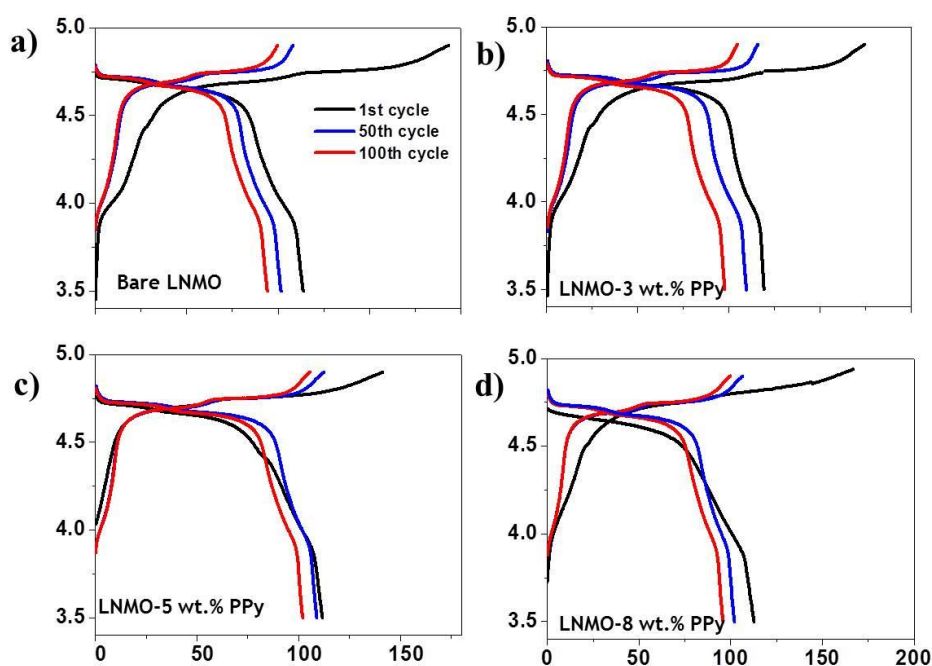

Figure 7.6 1st, 50th, and 100th cycle charge/discharge curves of LNMO (a), LNMO-3 wt. % PPy (b), LNMO-5 wt. % (c), and LNMO-8 wt. % PPy (d) at 1.0 C and elevated temperature (55 ℃).

The electrochemical properties of the obtained samples were further tested at elevated temperature (55 ℃). Before cycling, the cells were all stored in an oven for 10 h at 55 ˚C.

The first, 50th and 100th charge-discharge curves of bare and surface modified LNMO with various contents of PPy are shown in Fig. 7.6. The electrode made from bare LNMO displays initial discharge and charge capacities of 116 mAh g^{-1} and 193 mAh g^{-1}, respectively. Such huge charge consumption in the oxidation period can be ascribed to the formation of a large impedance [287]. Previous work has been reported that some undesirable interfacial reactions between LNMO and the liquid electrolyte are facilitated in storage at elevated temperature for a long time[263, 273]. The products from these harmful reactions are easy to deposit on the surface of the spinel cathode, resulting in the polarization resistance and large impedance. Furthermore, at the high operating voltage of 5 V, spinel cathodes would accelerate the formation of HF in the electrolyte. The increased concentration of HF would enhance the dissolution of Mn in the LNMO electrode material, causing poor electrochemical performance[263]. As shown in Fig. 7.6 (b, c, d), the electrolyte decomposition and concomitant film deposition on the PPy coated samples is significantly suppressed as the strong polarization gap disappears in the initial cycle. The initial coulombic efficiencies of LNMO-3 wt. % PPy, LNMO-5 wt. % PPy, and LNMO-8 wt. % are 67.5 %, 84.1 %, and 79.1 %, respectively. It should be noted that, although the higher temperature can promote the Li$^+$ transmission and accelerate the soaking of the electrolyte into the electrode, the thicker PPy layer may still interrupt electrode wetting. Therefore, the LNMO-5 wt. % PPy composite presents higher initial columbic efficiency than LNMO-8 wt. % PPy.

Figure 7.7(a) compares the cycling performances of the bare LNMO and LNMO-PPy composites at the 1 C rate and elevated temperature (55 ˚C). The bare LNMO delivers a discharge capacity of 94.5 mAh g^{-1} and exhibits capacity retention of only 81.4 % after 100 cycles. All the PPy-coated LNMO composites show better capacity retention than that of the bare sample. Among these cells, the LNMO-5 wt. % PPy has the best

electrochemical performance. After 100 cycles, it still retains a reversible capacity of 105.2 mAh g^{-1}, corresponding to capacity retention of 91 %. The capacity retentions of LNMO-3 wt. % PPy and LNMO-8 wt. % PPy are 83 % and 86 % after 100 cycles, respectively. The substantially improved cycling performance should be ascribed to the suppression of the dissolution of manganese and the electrode polarization, with the effective protection of the LNMO surface by the nano-architectured of the PPy wrapping layer. To understand this behavior, AC impedance measurements and chemical analyses were performed on the electrodes after cycling, which will be discussed in detail later.
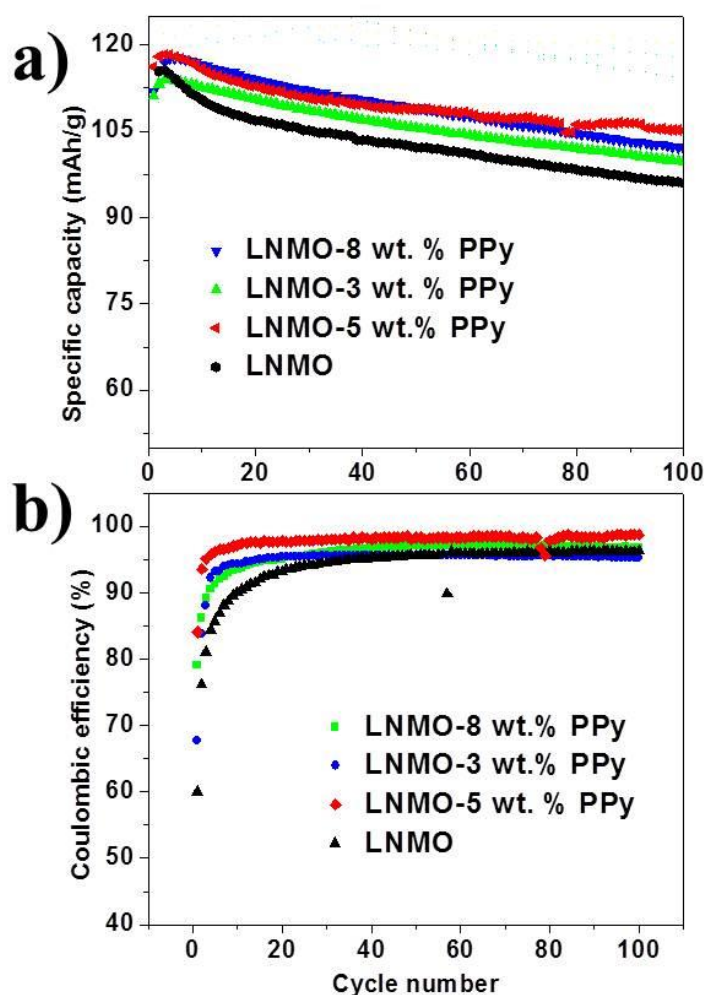
Figure 7.7 Cycling performance of LNMO, LNMO-3 wt. % PPy, LNMO-5 wt. %, and LNMO-8 wt. % PPy at 1.0 C and elevated temperature (55 °C): (a) specific capacity and (b) coulombic efficiency.

The coulombic efficiencies of the four samples are also summarized and compared in Fig. 7.6(b). Obviously, the coulombic efficiencies of all the composites cycled at elevated temperature are higher than those of the bare LNMO sample, which confirms that the PPy coating can effectively suppress the serious resistive effects of the surface film under harsh conditions: the highly oxidizing environment (> 4.5 V) and the elevated temperature [269]. This surface film causes thick solid electrolyte interphase (SEI) formation on the surface of the active material, thus leading to low coulombic efficiencies. After 5 cycles, however, the coulombic efficiencies of all the cells with PPy coating can reach 92%, while that for bare LNMO is only around 90 %.
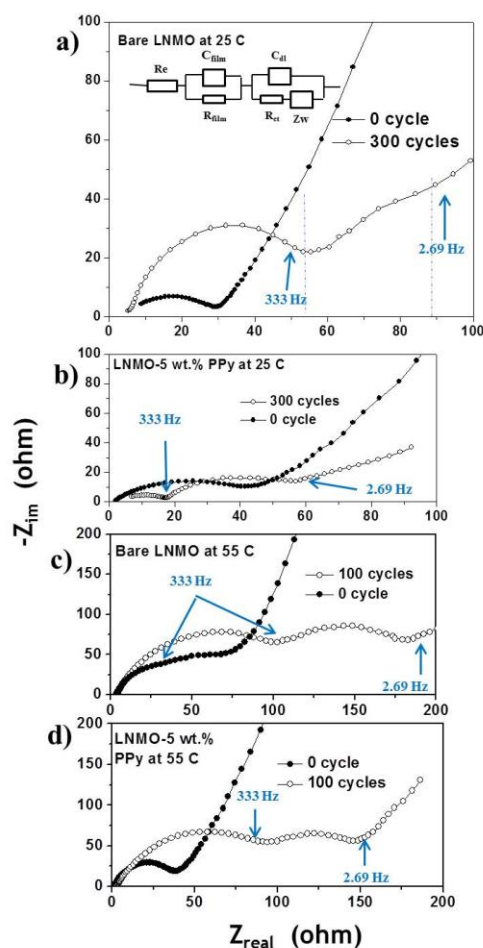
Figure 7.8 Nyquist plots of pristine LNMO and LNMO-5 wt. % PPy electrode before cycling and after cycling at 55 ˚C and 25 ˚C. The inset in (a) is the equivalent circuit used to interpret the data.

Table 7.1 Measured EIS data on pristine LNMO and LNMO-5wt. % PPy electrode after cycling.

	R_e (Ω)	R_{film} (Ω)	R_{ct} (Ω)
LNMO (25 ˚C)	7.41	63.16	124.79
LNMO-5 wt.% PPy (25 ˚C)	6.23	18.59	72.63
LNMO (55 ˚C)	2.25	132.87	203.58
LNMO-5 wt.% PPy (55 ˚C)	2.14	123.49	170.45

AC impedance analysis was conducted to explain the difference in performance shown in Fig. 7.8. The Nyquist plots before cycling consist of a semicircle and a straight line. The diameters of the semicircles for the bare LNMO cell and LNMO-5 wt. % PPy electrodes before cycling are 32 Ω and 45 Ω, respectively. After 300 cycles, two depressed semicircles were observed. The impedance data collected after cycling were fitted with the equivalent circuit shown in Fig. 7.9(a). In brief, they reflect three major constants: [288] R_e is the solution resistance due to electrolyte impedance and electrical contacts, which can be obtained from the intercept of the semicircle at high frequency with the x-axis. The semicircle in the high frequency region ($f > 300$ Hz), R_{film}, reflects the contact resistances between the active materials, the electrolyte and the current collector. The semicircle in the middle frequency range (0.1 Hz $< f <$ 10 Hz), R_{ct}, is attributed to the charge transfer resistance [269]. Their values calculated from the Nyquist plots are summarized in Table 7.1. The decrease in the resistance after cycling confirms that the incorporation of PPy is an effective method for enhancing the electron transport of LNMO, and consequently leads to a significant improvement in the electrochemical performance.

Interestingly, two condensed semicircles were observed in spectrum for the bare LNMO electrode at 55 ˚C before cycling, which means that a small portion of the electrolyte had been decomposed and directly deposited on the surface of the electrode after storage at high temperature for 8 h [273]. The electrolyte decomposition might have already formed a SEI layer on the active material before cycling, which is accordance with the electrochemical response of the electrode, which is discussed above. In contrast, the LNMO-5 wt. % PPy cell only shows one semicircle with 42 Ω, indicating a faster interfacial charge transfer.
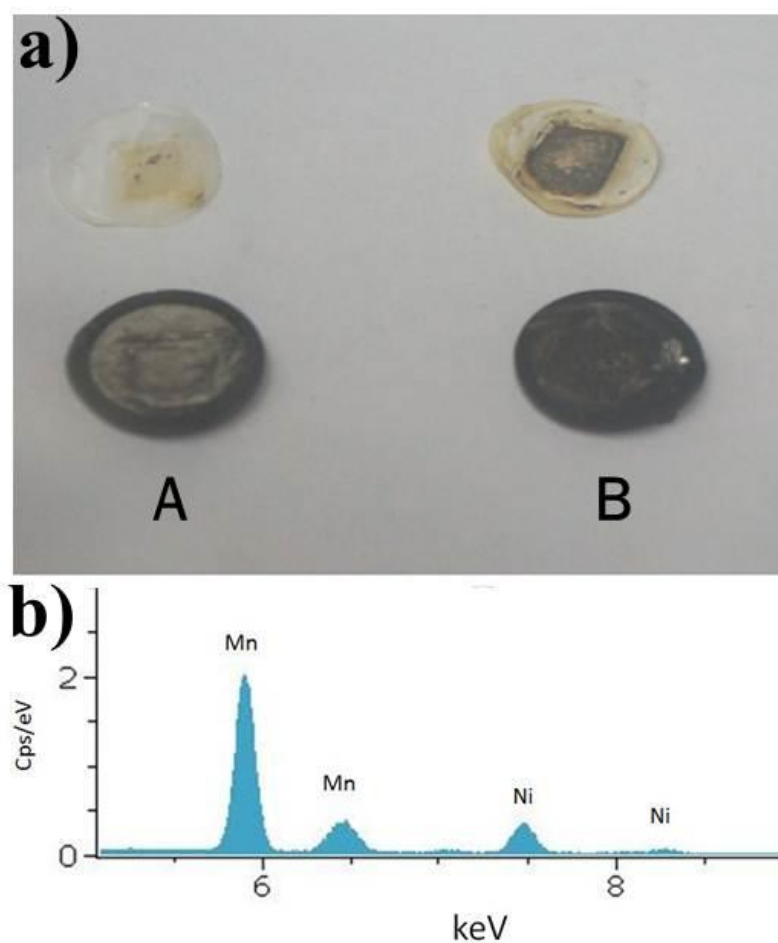
Figure 7.9 (a) Photographs of the lithium anodes [LNMO-5 wt. % (A) and bare LNMO (B)] and the corresponding separators, (b) EDX spectrum of the lithium anode in the coin cell of the bare LNMO sample after 100 cycles at 55 ˚C.

The cells after 100 cycles at 55 ℃ were opened up to observe the differences on the lithium anode surface. Much black material was found on the surface of the lithium metal and the separator in the bare LNMO cell [Fig. 7.9(a)], while the lithium foil in the LNMO-5 wt. % cell is clear. The Li anode in the cell with the bare LNMO was further analyzed by energy dispersive spectroscopy [Fig. 7.9(b)], and strong Mn and Ni peaks were clearly detected. This is believed to be due to dissolution of Mn^{2+} and Ni^{2+} in the active material into the electrolyte, which then migrates to and is deposited on the lithium anode. Therefore, we believe that a uniform PPy coating on the surface of LNMO not only can act an ion-conductive layer, but also acts to suppress the decomposition of Mn and Ni at elevated temperatures, as is demonstrated in Fig. 7.10.
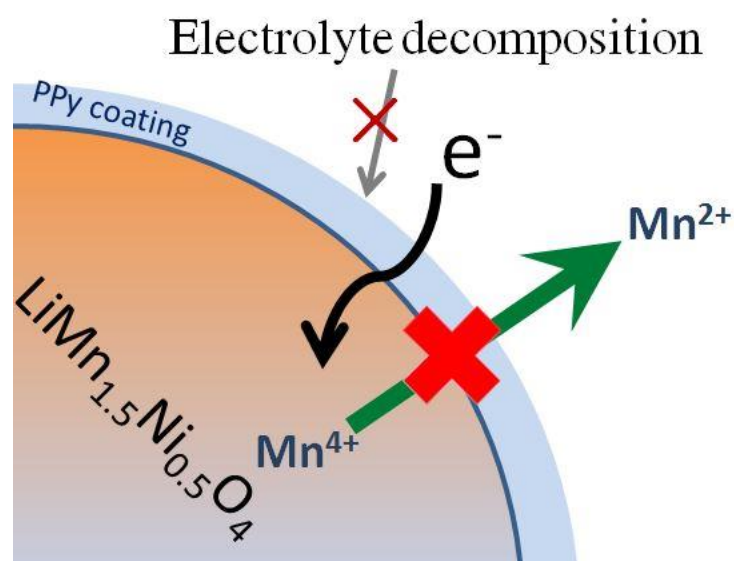
Figure 7.10 Schematic illustration of how the PPy layer acts as a conductive and protective layer suppresses the dissolution of Mn, as well as the unwanted electrolyte decomposition at elevated temperature.

Based on the discussions above, the PPy is demonstrated to be an effective additive for improving the electrochemical performance of the LNMO cathode material. The

promising electrochemical performance of LNMO/PPy can be ascribed to three reasons (demonstrated in Fig. 7.10): (1) PPy is a kind of conductive polymer and can work as a conductive additive, thus improving the conductivity of bare LNMO; (2) the dissolution of Mn^{2+} into the electrolyte can be suppressed by the PPy layer; and (3) the external PPy layer on the LNMO particles can further relieve the serious electrolyte decomposition for the active material, and thus improve the initial coulombic efficiency at elevated temperature.

7.4 Summary

An innovative way to improve the electrochemical performance of LNMO by depositing a conductive PPy coating has been demonstrated. It is suggested that the LNMO with 5 wt. % PPy coating shows the best cycle life and coulombic efficiency compared to those of the bare LNMO and LNMO with other PPy content. The results of chemical analyse is of the lithium foil anode after cycling confirm that the presence of the PPy coating layer is responsible for the suppression of manganese and nickel dissolution in the LNMO during Li^+ insertion/de-insertion processes. The PPy layer can also protect the electrode from the products which originate from the decomposition of the electrolyte at elevated temperature, and it thus leads to higher coulombic efficiencies. In addition, a uniform PPy layer is also proved to be an effective conductive agent for the electrode, leading to attractive lithium storage capability at a high charge/discharge rates. Adding into consideration the superior electrical performance with PPy, we believe the LNMO-PPy composite has potential for as a high-energy and high-power cathode material for the LIBs.

Chapter 8   LiNi$_{0.5}$Mn$_{1.5}$O$_4$ Spinel cathode using room temperature ionic liquid as electrolyte

8.1 Introduction

The search for cathode materials and electrolytes with high voltage capacity for LIBs has been intense in recent years, since the capacity of a LIB is normally limited by the cathode material due to the safety concerns. In recent years, LiNi$_{0.5}$Mn$_{1.5}$O$_4$ (LNMO) has attracted considerable attention from many research groups in the field of energy storage, owing to its high specific energy of 658 Wh kg^{-1} [289-291], which is much higher than commercially available cathode materials such as LiCoO$_2$ (518 Wh kg^{-1}), LiMn$_2$O$_4$ (400 Wh kg^{-1}), LiFePO$_4$ (495 Wh kg^{-1}), and LiCo$_{1/3}$Ni$_{1/3}$Mn$_{1/3}$O$_2$ (576 Wh kg^{-1}). The major charge/discharge reactions of LiNi$_{0.5}$Mn$_{1.5}$O$_4$ take place, however, at ~ 4.7 V (vs. Li/Li$^+$), which is beyond the stability potential (~4.5 V) of conventional electrolytes (LiPF$_6$ dissolved in carbonates, such as ethylene carbonate (EC), dimethyl carbonate (DMC)/diethyl carbonate (DEC)) [264]. The use of an unstable electrolyte in the high potential range of LNMO results in low coulombic efficiency, which is a major handicap for the commercial of LNMO. Therefore, it is worthwhile to search for highly stable electrolytes for LNMO to improve the coulombic efficiency.

Since Wilkes and Zaworotko reported on room temperature ionic liquids (RTILs) based on the 1-ethyl-3-methylimidazaolium cation and the tetrafluoroborate anion [292], several research groups have focused their work on the development of RTIL electrolyte for lithium batteries. RTILs have shown potential as safe electrolytes for use in lithium ion battery systems, due to their attractive properties, such as electrochemical stability (4.0-

5.7 V), thermal stability, and high ionic conductivity [163, 293, 294]. In addition, owing to the high reduction dissolution of the active material into conventional organic electrolytes, RTIL for electrolytes can obviously improve the performance of lithium batteries using certain cathode materials, such as S [295, 296], NiS-Ni$_7$S$_6$ [297], V$_2$O$_5$ [298], and LiV$_3$O$_8$ [299]. Among the various RTILs, electrolytes based on pyrrolidinium systems combined with a lithium salt can be considered as a good benchmark for ionic liquid-based electrolytes. This is because popular imidazolium salts show a window of stability of ~ 4 V, while pyrrolidinium salts, especially those based on imide anions, can show electrochemical stability as high as 6 V [293]. Meanwhile, it has been reported that lithium bis(trifluromethanesulfonyl) amide (LiNTf$_2$), had a beneficial effect on solid electrolyte interphase (SEI) formation on the lithium electrode surface, which plays a key role in terms of the lifetime and safety characteristics of lithium batteries [269]. In a previous work [300], the ionic liquid lithium bis(trifluoromethanesulfonyl) imide (LiNTf$_2$) in N-butyl-N-methylpyrrolidinium bis(trifluoromethanesulfonyle) imide (C$_4$mpyrNTf$_2$) exhibited relatively high conductivity and low viscosity with 0.5 mol kg^{-1} of LiNTFf$_2$. Furthermore, the LiNTf$_2$-C$_4$mpyrNTf$_2$ system can allow lithium to be cycled with a high degree of reversibility as well, while uniform lithium deposit morphology over many cycles could be achieved at moderate current densities and cycling efficiencies exceeding 99 % have been obtained [301].

In this study, LiNi$_{0.5}$Mn$_{1.5}$O$_4$ was prepared by via a rheological phase method. 1 M LiNTf$_2$ in C$_4$mpyrNTf$_2$ was used as a new electrolyte for Li/LiNi$_{0.5}$Mn$_{1.5}$O$_4$ cells without additives, and the relationship between the electrolyte characteristics and the performance of Li/LiNi$_{0.5}$Mn$_{1.5}$O$_4$ cells was studied in detail. The electrochemical performance shows that the LiNi$_{0.5}$Mn$_{1.5}$O$_4$ nanoparticles using 1 M LiNTf$_2$ in C$_4$mpyrNTf$_2$ as electrolyte

show comparable capacity to that with conventional electrolyte (1 M $LiPF_6$ in EC: DEC = 1:2 (v/v)), as well as significantly improved coulombic efficiency.

8.2 Experimental

8.2.1 Synthesis of $LiNi_{0.5}Mn_{1.5}O_4$

The starting materials were analytically pure LiOH, $Ni(CH_3COO)_2 \cdot 4H_2O$, $Mn(CH_3COO)_2 \cdot 4H_2O$, and citric acid. The LiOH, $Ni(CH_3COO)_2 \cdot 4H_2O$, $Mn(CH_3COO)_2 \cdot 4H_2O$, and citric acid were mechanically mixed in the molar ratio of 1:0.5:1.5:3.6 in an agate mortar. After the mixture was ground homogeneously, an appropriate amount of water was added to the powder to obtain a rheological phase state mixture. The mixture was then heated at 90 °C for 12 h, and a precursor was obtained. After that, the precursor was first sintered at 580 °C for 5 h and then was heated at 680 ºC, 750 ºC, and 820 °C for 8 h in air, respectively.

8.2.2 Materials characterization

Phase analysis of the $LiNi_{0.5}Mn_{1.5}O_4$ nanoparticles was conducted by X-ray diffraction (XRD; Philips PW1730). The morphology and structure of the $LiNi_{0.5}Mn_{1.5}O_4$ were examined by field emission scanning electron microscopy (FESEM) using a JEOL FESEM-7500 30 kV instrument and the specific surface areas were determined by the Brunauer-Emmett-Teller technique (BET, Quanta Chrome Nova 1000).

8.2.3 Electrochemical characterizations

To test their electrochemical performance, the $LiNi_{0.5}Mn_{1.5}O_4$ samples were mixed at a rate of 80 wt% active materials with 10 wt% carbon black and 10 wt% polyvinylidene fluoride (PVDF). The slurry was uniformly pasted onto pieces of Al foil with an area of 1 cm^2 and dried in a vacuum at 100 ºC for 24 h. Then, the electrodes were compressed before making the cells. Two kinds of electrolytes were used, including a home-made organic solvent-based electrolyte, consisting of 1 M lithium bis(trifluoromethanesulfonyl) amide ($LiNTf_2$) in N-butyl-N-methyl- pyrrolidinium bis(trifluoromethanesulfonyl) amide ($C_4mpyrNTf_2$), and a conventional organic solvent-based electrolyte consisting of 1 M $LiPF_6$ in a 1:2 (v/v) mixture of ethylene carbonate and diethyl carbonate. The coin-type cells (CR2032) were assembled with a lithium metal counter electrode in an argon-filled glove box. Galvanostatic charge/discharge cycling was conducted using Land Battery Testers in the potential range of 3.5-5.1 V at a current density of 0.1 C (1 C = 140 mA g^{-1}). Electrochemical impedance spectroscopy (EIS) was conducted using a Biologic VMP-3 electrochemical workstation for different potential and cycling states.

8.3 Results and Discussion

8.3.1 Structure and morphologies

Figure 8.1 presents the XRD patterns obtained from the LNMO powders. All the samples show diffraction peaks characteristic of the cubic spinel structure (space group = Fd3m, JCPDS #32-0581). For the sample annealed at 820 °C, very weak impurity peaks indexed to $Li_xNi_{1-x}O$ are detected at the left shoulders of the (400) and (222) peaks. This is an ordinary occurrence, as this impurity originates from the Ni content, and the oxygen loss in samples annealed at high temperature reduces the amount of Ni in the spinel phase [290, 302, 303]. The intensity ratio of (4,0,0)/(3,1,1) increased as the temperatures rise, indicating

presence of relatively extensive transition metal cation substitution in tetrahedral 8a sites of the spinel-type structure [304]. In previous research, Ohzuku et al. [305] have pointed out the occupancy of the 8a tetrahedral lithium sites by substituent ions will lead to some unfavourable electrochemical characteristics. For the sample annealed at 750 °C, the (4,0,0)/(3,1,1) intensity ratio is only 0.69, which is much smaller than for the others (0.89 at 680 °C and 0.97 at 820 °C). In this regard, the sample annealed at 750 °C is expected to show the best performance.
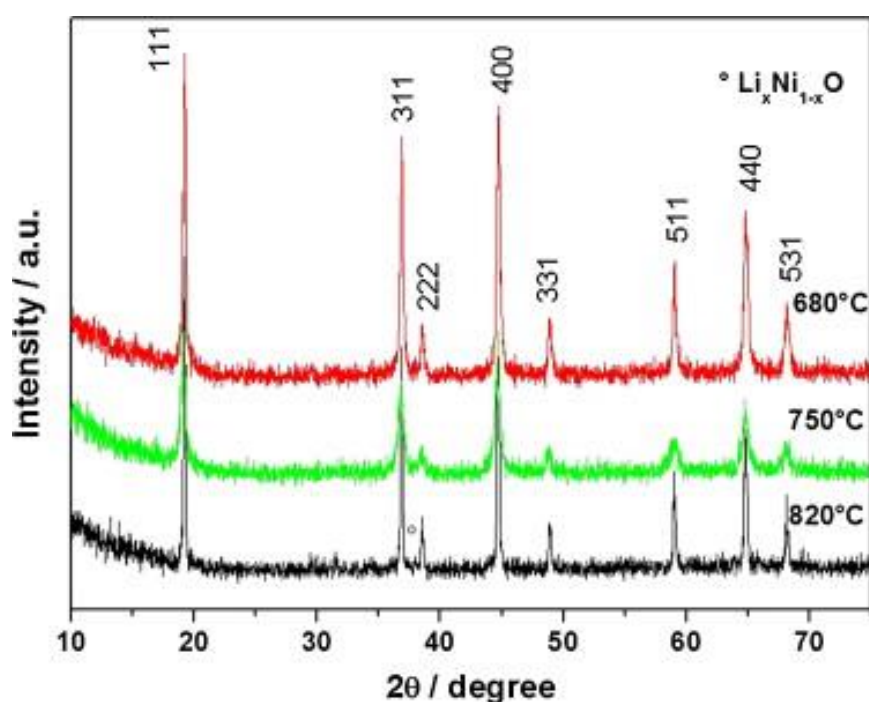
Figure 8.1 XRD patterns of the samples annealed at different temperatures: 680 °C, 750°C, and 820°C. (° indicates impurities.)

N_2 adsorption-desorption studies were also performed to determine the specific surface area of the LNMO. The Brunauer-Emmett-Teller (BET) surface areas were found to be 19.1, 16.5, and 5.5 m^2 g^{-1} for the samples annealed at 680 °C, 750 °C, and 820 °C, respectively. A further increase in the reaction temperature leads to a larger surface area of the sample.
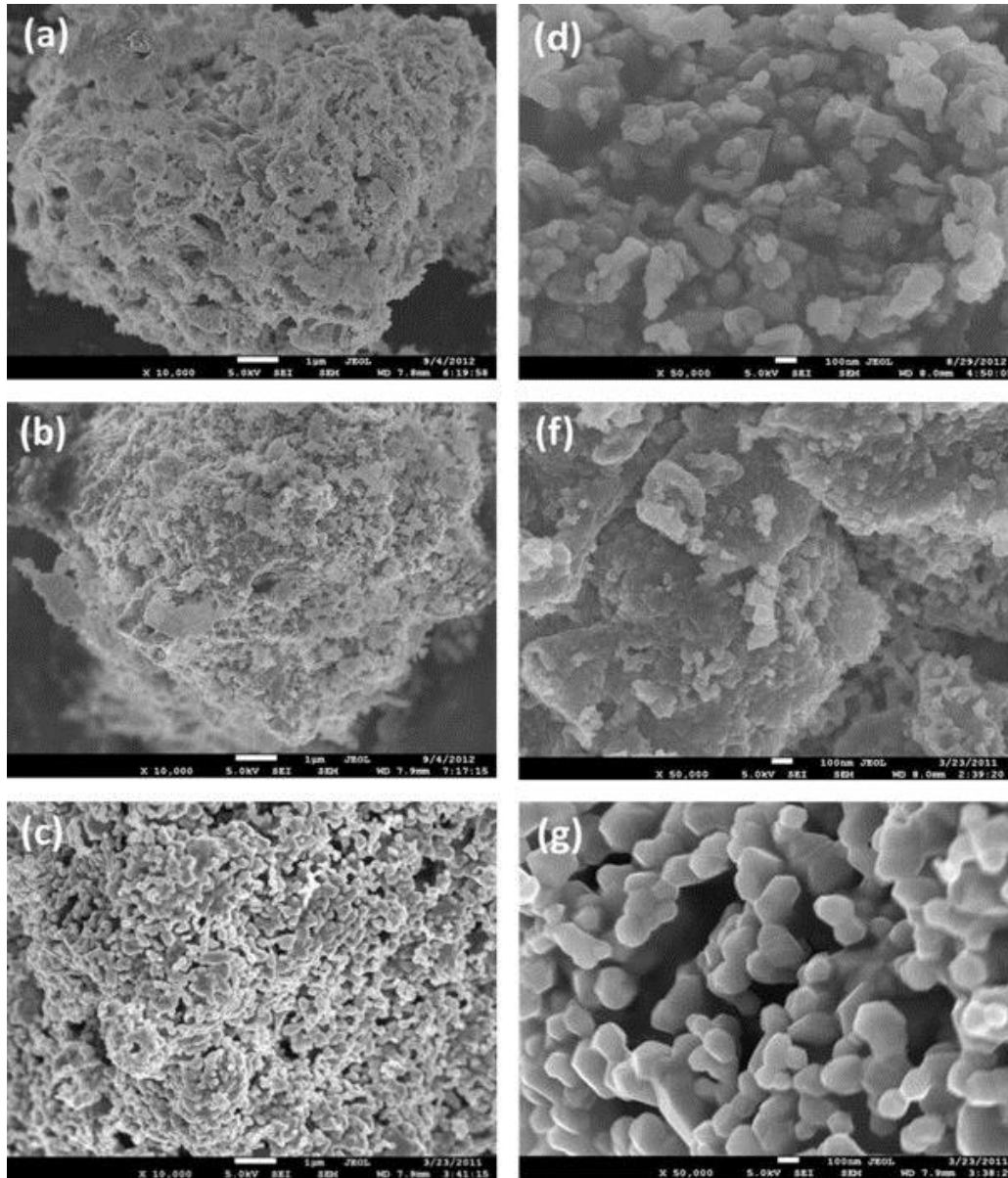
Figure 8.2 SEM images of samples annealed at different temperatures: 680 °C (a, d), 750 °C (b, f), and 820 °C (c, g).

Typical scanning electron microscope (SEM) images of the samples are presented in figure 8.2. Fig. 8.2a shows sample annealed at 680 °C was composed of big secondary particles with abnormal agglomeration and surface roughness compared to other samples in this study. From Fig. 8.2(d), it is noted that the primary particles were on 50-150 nm in diameter. The morphology of sample obtained at 750 °C was found to consist of more homogeneous LNMO particles with dimensions of approximately 100 nm. They are

agglomerated into large particle with the average diameter of 5 um (Fig. 8.2(b)). As shown in Fig. 8.2 (c, g), well-defined particles 200-300 nm in diameter could be obtained after annealing at 820 °C. Therefore, the sample annealed at lower temperature has a relatively smaller particle size, and the result is consistent with the above BET analysis. On the other hand, the higher temperature did not increase the phase purity, although it could lead to a better crystal shape.

8.3.2 Electrochemical characterization

Figure 8.3(a-c) compares the charge-discharge voltage profiles of the Li/LNMO cells for the three samples in EC/DEC electrolyte. Figure 8.3(d) shows charge-discharge curves for the sample annealed at 750 °C in RTIL electrolyte. It should be noted that the cells with conventional electrolyte exhibit potential fluctuation at potentials higher than 5 V vs. Li/Li$^+$ for the initial charge, which can be attributed to electrolyte oxidation. Initial charge-discharge capacities and coulombic efficiencies for all cells are summarized in Table 8.1. The cells containing RTIL showed comparable discharge capacities and much higher coulombic efficiency compared to the conventional organic electrolyte. The extra charge consumption in the charging (oxidation) period for the conventional electrolyte can be related to the electrolyte decomposition and concomitant film deposition. The cells were successfully cycled in following cycles, however, suggesting the formation of a fairly stable solid electrolyte interphase (SEI), which protects the electrolyte against further degradation [306, 307]. In contrast, the cell was successfully cycled in RTIL, indicating that the electrolyte decomposition and film deposition are not severe in RTIL electrolyte. For the sample annealed at 820 ˚C, the small plateau at 4.1 V is due to the Mn^{3+}/Mn^{4+} redox couple caused by excessively fast cooling and oxygen deficiency during cooling of the sample [290]. Indeed, X-ray diffraction of this sample shows the presence of

136
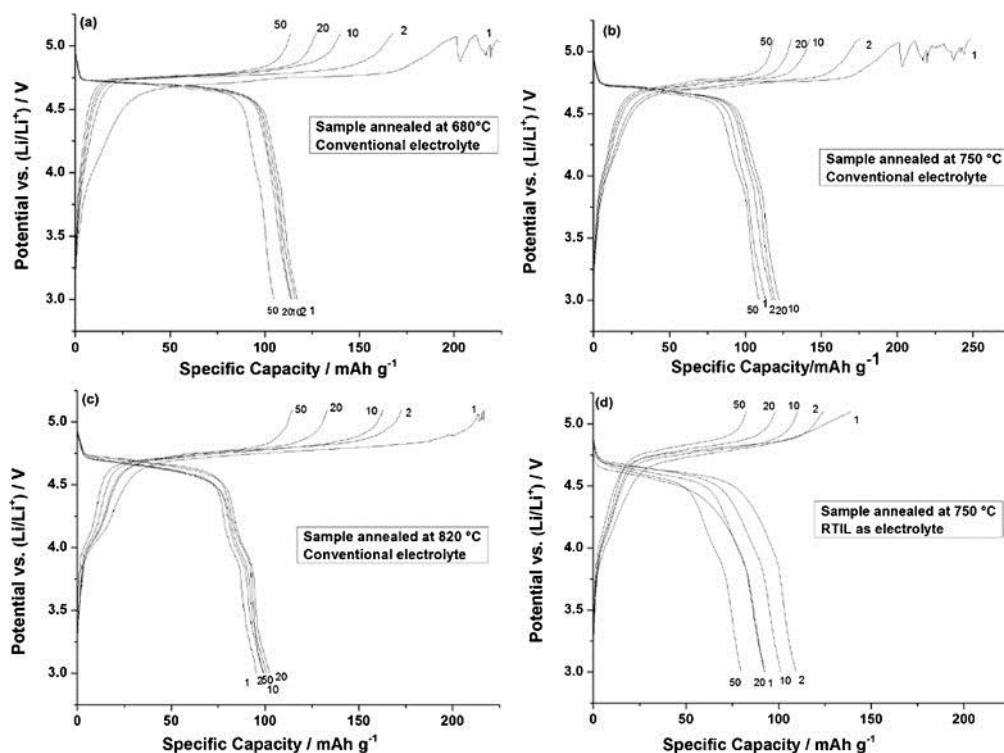
Figure 8.3 Charge-discharge curves for selected cycles for LiNi$_{0.5}$Mn$_{1.5}$O$_4$ electrodes made from samples sintered at different temperatures and used with conventional electrolyte or RTIL electrolyte.

Table 8.1 Initial charge-discharge capacities and coulombic efficiencies.

Electrolyte	Capacity (mAh g^{-1})		Coulombic efficiency (%)
	Charge	Discharge	
680 °C- Conventional	189.7	98.8	52.1
750 °C- Conventional	248.2	109.1	45.1
820 °C- Conventional	216.7	94.4	43.6
680 °C- RTIL	149.6	100.4	67.1
750 °C- RTIL	139.2	92.4	66.4
820 °C- RTIL	154.0	102.4	66.5

the impurity Li$_x$Ni$_{1-x}$O phase. The main charge plateau at 4.7 V is attributed to the Ni^{2+}/Ni^{4+} redox couple [308]. Furthermore, the potential corresponding to the transformation of Ni^{2+} to Ni^{4+} in the ionic-liquid-based electrolyte was lower than in the conventional

electrolyte due to the lower ionic conductivity of RTIL at room temperature. This phenomenon has been observed in previous work on ionic-liquid-based electrolyte for lithium batteries[295, 296].
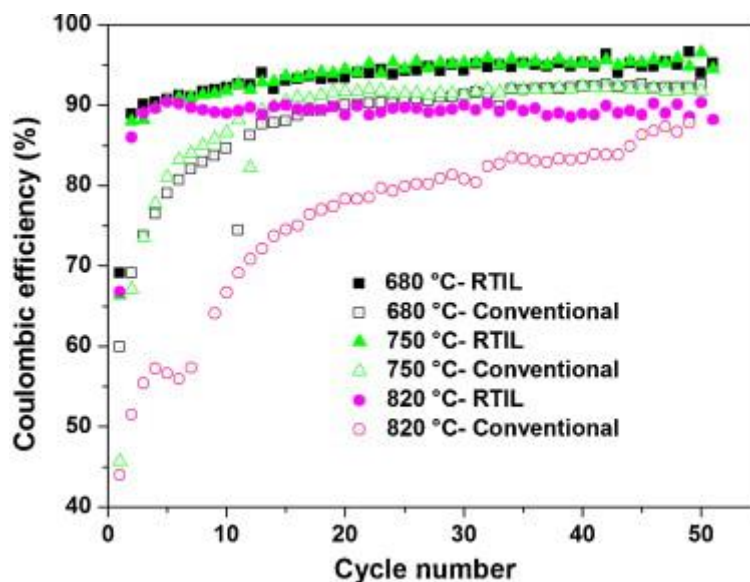
Figure 8.4 Coulombic efficiency of $LiNi_{0.5}Mn_{1.5}O_4$ electrodes with conventional and RTIL electrolytes.

Figure 8.4 presents the coulombic efficiency of the samples in the different electrolytes. In general, coulombic efficiency steadily increased and then stabilized with cycle number. It is clear that the cells with RTIL electrolyte show much better performance than those with conventional electrolyte. The sample annealed at 750 °C shows the best coulombic efficiency among the three samples examined under the present experimental conditions. With conventional electrolyte, its average efficiency for the first fifteen cycles is 75.9 %. In contrast, the cell using RTIL has 88.6 % coulombic efficiency for the first fifteen cycles, and after that, the coulombic efficiency averages over 95 %, which may be because the formation of a stable surface film on the electrode in RTIL is more desirable than in the conventional electrolyte [269]. This means that RTIL can improve the coulombic

efficiency of LNMO. These features will be evidenced in the following electrochemical impedance spectroscopy (EIS) section.

Figure 8.5 shows discharge capacity versus cycle number for cells based on the different samples in different electrolytes. The sample annealed at 750 °C has the highest capacity. The capacities of LNMO with conventional electrolyte were higher than for samples with ionic liquid-based electrolyte. Similar performance has also been observed for $LiFePO_4$ [165] and $LiCoO_2$ [309]. This can be explained by the dissolution of $[Li^+]$ $[NTf_2^-]$ salt in the $[C_4mpyr^+]$ $[NTf_2^-]$ ionic liquid, leading to a ternary system $[Li^+]_m[C_4mpyr^+]_n[NTf_2^-]_{(m+n)}$ with increased viscosity and lower conductivity, at the level of 1-2 mS cm^{-1} [171, 310]. The highly viscous electrolyte causes an increase in both electrolyte resistance and charge transfer resistance at the electrode/electrolyte interface. It leads to poor impregnation of the electrodes as well [311]. Meanwhile, as previously mentioned, the more stable SEI formed at the electrode surface contribute to the irreversible capacity and lower the initial coloumbic efficiency.
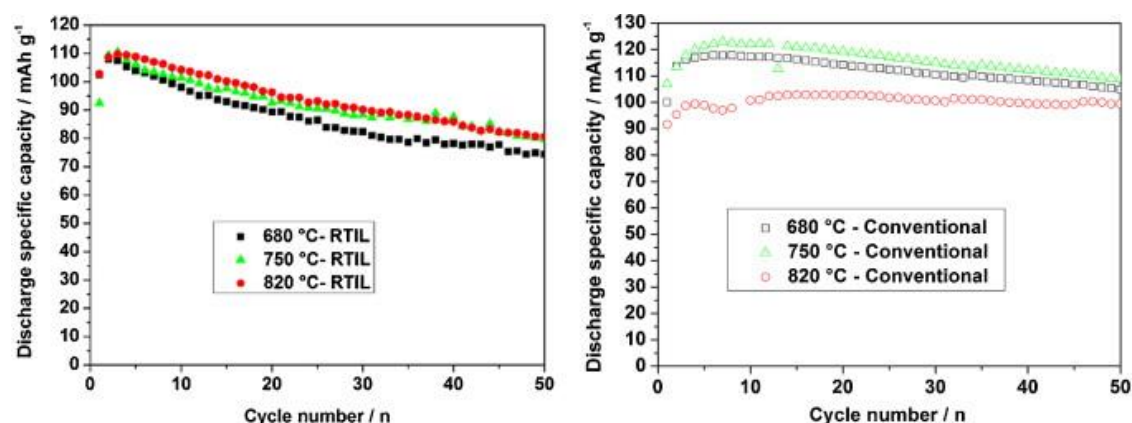
Figure 8.5 Cycle life of $LiNi_{0.5}Mn_{1.5}O_4$ annealed at different temperatures: (a) with RTIL electrolyte and (b) with conventional electrolyte.

In order to gain further understanding of the differences in the electrochemical performance between the conventional and the ionic liquid electrolytes, the sample annealed at 750 °C, which had the highest capacity, was selected for EIS testing in different electrolytes. Before the EIS measurements, all the samples were charged to various potentials and maintained at charged potentials of 4.7 V and 5.1 V for 2 h. Fig. 8.6 shows the EIS results for lithium cells in the charged state at the 1st and 6th cycles. The impedance spectra reflect several processes that take place in series: Li migration through surface films, charge transfer, solid-state diffusion, and finally, accumulation of Li in the bulk of the active mass. According to previous impedance spectroscopy studies, the resistance associated with the higher frequency semicircle (typically, 300 Hz < f), R_{film}, is assigned to lithium-ion diffusion through surface films, and the charge-transfer resistance associated with the lower-frequency semicircle (typically, 0.1 Hz < f < 10 Hz), R_{ct}, is related to Li ion transportation across the surface film active mass interface [312]. Their values calculated from the diameters of the high-frequency and the medium-to-low frequency semicircles in the Nyquist plots for the electrodes are summarized in the Table 8.2. Obviously, the results obtained using conventional and RTIL electrolytes are completely different. The impedance curves show one compressed semicircle related to the greatest frequency range of interest (high to low frequencies) instead of separation of the different features. It means the electrode with RTIL is thin enough and R_{ct} is low at the low frequencies, then the Nyquist plot becomes a steep line. On the other hand, it has been reported that in the $LiPF_6$ solution LiF is a major constituent on the electrode surface, due to the reaction of the active surface with trace HF, which is unavoidably present [313]. Whenever LiF films are formed on the electrodes, their impedance becomes very high because of the high resistivity of LiF films so far as Li ion transport is concerned[314]. Accordingly, the cell assembled with the conventional electrolyte is shown to have much higher overall resistance than the cell with RTIL. After 5 cycles, it should be noted that

140

the impedance in both types of electrolyte is reduced due to the stabilized SEI layer on the electrode surface.
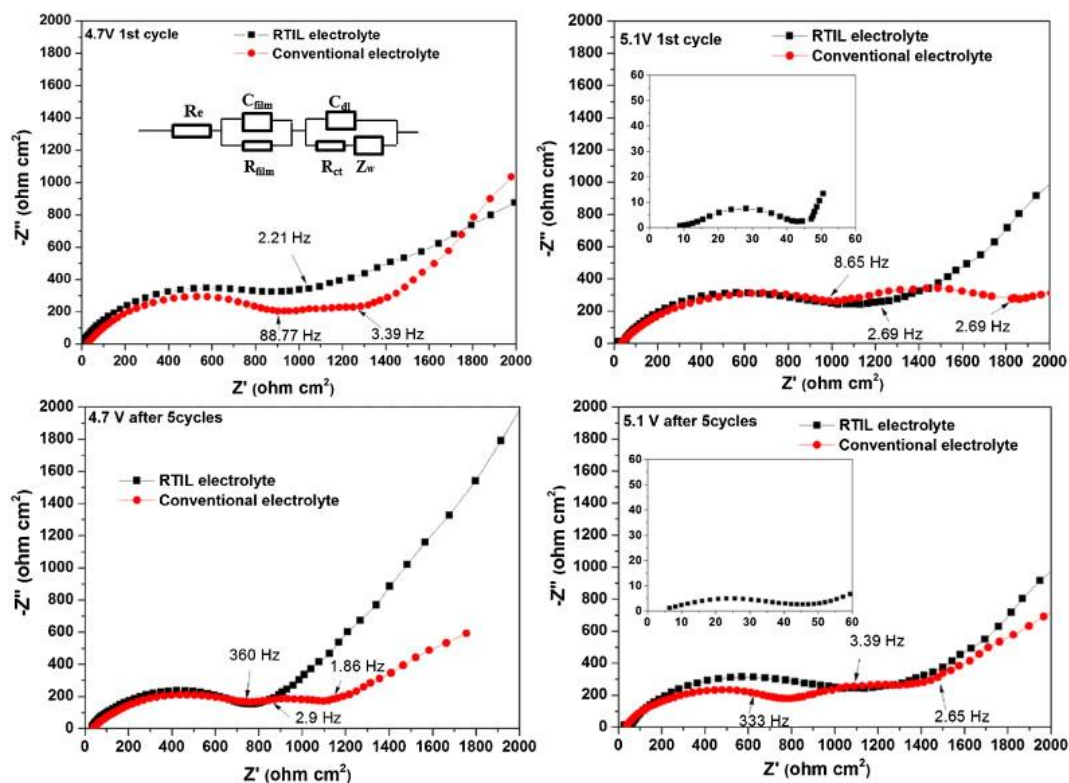
Figure 8.6 EIS spectra obtained from Li/ LiNi$_{0.5}$Mn$_{1.5}$O$_4$ cells for the 1st (top) and 6th (bottom) cycles using conventional and RTIL electrolytes. The electrode potentials are 4.7 V (left) and 5.1 V (right).

Table 8.2 R$_{film}$ and R$_{ct}$ for different testing states calculated from Nyquist plots for LiNi$_{0.5}$Mn$_{1.5}$O$_4$ spinel electrodes in different electrolytes.

	Conventional Electrolyte		RTIL	
Testing state	R$_{film}$ (Ohm cm^2)	R$_{ct}$ (Ohm cm^2)	R$_{film}$ (Ohm cm^2)	R$_{ct}$ (Ohm cm^2)
1st 4.7 V	903	1296	56	1160
1st 5.1 V	978	1841	75	1066
6th 4.7 V	753	890	102	820
6th 5.1 V	760	1471	133	1380

8.4 Summary

In summary, $LiNi_{0.5}Mn_{1.5}O_4$ nanoparticles can be prepared by a rheological phase method. RTIL ($LiNTf_2$-$C_4mpyrNTf_2$) can be a better electrolyte than the conventional alternative for $LiNi_{0.5}Mn_{1.5}O_4$ electrodes, as it improves the coulombic efficiency. The cell using RTIL as electrolyte shows a higher initial coulombic efficiency of 66.4%, while the cell using conventional electrolyte only shows an initial coulombic efficiency of 45.7 %. The results suggest that RTIL could be a promising electrolyte for $LiNi_{0.5}Mn_{1.5}O_4$ cells in terms of non-flammability, safety, and better electrochemical performance.

Chapter 9   Conclusion and Research Outlook

9.1 General Conclusion

In this doctoral work, three major components in the lithium-ion battery (LIB) system have been investigated, including ionic liquid electrolyte, anode materials, and cathode materials. The synthesis, physical features, and electrochemical performance of various nanostructured electrode materials for lithium batteries were thoroughly characterized. In the case of Ge nanoparticles as anode material, the effects of polypyrrole (PPy) additive were studied. LiV_3O_8/polyaniline (PAn) and $LiNi_{0.5}Mn_{1.5}O_4$/PPy nanocomposites were also investigated as cathode materials. In the case of $Ni_{0.5}Zn_{0.5}Fe_2O_4$ nanospheres prepared at different reaction temperatures, the morphology and electrochemical performance were compared. Finally, the application of room temperature ionic liquid as electrolyte at high voltage (> 5 V vs. Li/Li^+) was studied. Based on the work presented in this dissertation, this doctoral work can broaden our knowledge in the field of advanced materials for electrode and electrolyte in LIBs.

The development of the LIB in this thesis started with preparation of anode materials. Ge-PPy nanocomposite was synthesized by a simple chemical reduction method at room temperature. The field-emission scanning electron microscope (FESEM) images show that deposition of Ge nanoparticles onto the surfaces of polypyrrole take places during the reaction. The electrochemical results show the Ge-PPy nanocomposite performed better in terms of higher discharge capacity and better life cycle than the pure Ge. This excellent performance of the nanocomposite could be mainly due to the conductive PPy core. It could act as a conducting medium, binder, diluting agent, and cushioning medium to

protect the electrode from pulverization and delamination caused by the huge volume changes in the Ge nanoparticles during Li^+ insertion/extraction.

Mesoporous $Ni_{0.5}Zn_{0.5}Fe_2O_4$ (NZFO) nanospheres have been successfully prepared via a one-step solvothermal method. Through adjusting the reactant concentration, the morphologies, crystallite sizes, and diameters of NZFO nanospheres can be controlled. The formation mechanisms of the mesoporous or hollow nanosphere are explored based on Ostwald ripening process. The mesoporous NZFO nanospheres with small crystallite size and high surface area show high reversible specific capacity and better capacity retention, indicating that the mesoporous NZFO nanospheres have potential applications in LIBs.

Novel LiV_3O_8 nanorods were synthesized by the hydrothermal method, combined with a convenient solid-state reaction. After that, LiV_3O_8 nanorods were coated with a conductive polyaniline layer by an anionic surfactant. The composite of LiV_3O_8 with 12 wt. % PAn coating shows significantly better cycle life and substantially improved high rate capacity compared to that of the bare LiV_3O_8 electrode. These improvements can be attributed to the PAn coating in the matrix, which is responsible for improving the electrical conductivity of the LiV_3O_8 materials, as well as preventing aggregation and dissolution of active material in the electrolyte.

Nanocomposites of $LiNi_{0.5}Mn_{1.5}O_4$ (LNMO) coated with conductive PPy have been successfully synthesized by a simple polymerization reaction in aqueous solution. The LNMO-5 wt. % PPy nanocomposite showed very stable cycling up to 300 cycles compared to those of bare LNMO and LNMO with other PPy content at room temperature. It also delivered higher coulombic efficiency and discharge capacity at

144

elevated temperature. The electrochemical results suggest that the PPy layer works not only as an effective conductive agent for the electrode, but also as a protective layer for the suppression of manganese and nickel dissolution in the LNMO during Li^+ insertion/de-insertion processes. In addition, the PPy layer can also protect the electrode surface from the products which originate from the decomposition of the electrolyte at elevated temperature.

In addition to electrode materials, a new type of electrolyte was also studied to complete the full lithium battery system. In terms of candidate electrolyte materials for the LIB, room temperature ionic liquid (RTIL) with high electrochemical stability (4.0-5.7 V), thermal stability, and safety was chosen as a promising electrolyte for the LIB at high voltage. $LiNi_{0.5}Mn_{1.5}O_4$ nanoparticles prepared by a rheological phase method were used as cathode material and lithium foil was used as counter electrode. The charge-discharge measurement results showed that RTIL can be a better electrolyte compared to conventional electrolyte for $LiNi_{0.5}Mn_{1.5}O_4$ electrodes, as it improves the coulombic efficiency. The initial coulombic efficiency increased from 45.7 % to 66.4 % with RTIL electrolyte, when the cut-off voltage was extended up to 5.1 V.

9.2 Outlook

Based on the work presented in this thesis, it is shown that high capacity alternative electrode materials could be synthesized using simple, safe, and efficient methods, that meets the growing requirements of green chemistry. We expect our strategy to synthesize nanostructured materials could be of general interest and have influence on synthesis methods for other potential electrode materials. The nanostructured active materials with

different morphologies are beneficial towards lithium storage and show several advantages, including (i) better accommodation of the strain of lithium insertion/removal, improving cycle life; (ii) new reactions not possible with bulk materials; (iii) higher electrode/electrolyte contact area, leading to higher charge/discharge rates; (iv) short path lengths for electronic transport (permitting operation with low electronic conductivity or at higher power); and (v) short path lengths for Li^+ transport (permitting operation with low Li^+ conductivity or higher power). On the other hand, there are still many disadvantages associated with the development of nanostructured electrodes for lithium batteries. Disadvantages include (i) an increase in undesirable electrode/electrolyte reactions due to high surface area, leading to self-discharge, poor cycling and calendar life; (ii) inferior packing of particles leading to lower volumetric energy densities unless special compaction methods are developed; and (iii) potentially more complex synthesis. With these advantages and disadvantages in mind, we explored the addition of conductive polymer into the electrode material, which is proven to be effective method in enhancing the electrochemical properties. The conductive polymer not only can provide efficient electronic pathways for the active materials, but also protect the electrode from pulverization and delamination. In addition, the future work also may be focused on the improvement of the energy density and safety of the LIB that can be achieved by using room temperature ionic liquid electrolyte at high voltage (> 5.0 V). The main advantage of RTIL over conventional organic solvents is its non-flammability, negligible vapour pressure, and high chemical and thermal stability.

In summary, the Li-based battery chemistry is relatively young, and as such, is a source of inspiration as well as numerous exciting challenges. The efforts should be highly multidisciplinary with strong roots in the fields of organic and inorganic chemistry, physics, surface science and corrosion. Through materials design, we can expect

significant improvements in energy density. As Li-rechargeable batteries just enter their next decades, scientists and engineers predict an even brighter future lies ahead.

REFERENCES

1. D. Linden and T. B. e. Reddy, eds., *Handbook of Batteries, 3rd edn*, McGraw-Hill, 2002.

2. H. c. D. Abrun~a, Y. Kiya and J. C. Henderson, *Print edition*, 2008, **61**, 43-47.

3. R. M. Dell and D. A. J. Rand, eds., *Understanding Batteries*, The Royal Society of Chemistry, Cambridge, 2001.

4. K. Mizushima, P. C. Jones, P. J. Wiseman and J. B. Goodenough, *Solid State Ion.*, 1981, **3-4**, 171-174.

5. R. Yazami and P. Touzain, *J. Power Sources*, 1983, **9**, 365-371.

6. V. Etacheri, R. Marom, R. Elazari, G. Salitra and D. Aurbach, *Energy & Environmental Science*, 2011, **4**, 3243-3262.

7. J. B. Goodenough and Y. Kim, *Chem. Mater*, 2010, **22**, 587-603.

8. J. M. Tarascon and M. Armand, *Nature*, 2001, **414**, 359-367.

9. R. Koksbang, J. Barker, H. Shi and M. Y. Saidi, *Solid State Ion.*, 1996, **84**, 1-21.

10. M. S. Whittingham, *Chem Rev*, 2004, **104**, 4271-4301.

11. E. Antolini, *Solid State Ion.*, 2004, **170**, 159-171.

12. J. Akimoto, Y. Gotoh and Y. Oosawa, *J Solid State Chem*, 1998, **141**, 298-302.

13. Y. Wang and G. Z. Cao, *Adv Mater*, 2008, **20**, 2251-2269.

14. J. R. Dahn, U. Vonsacken, M. W. Juzkow and H. Aljanaby, *J. Electrochem. Soc.*, 1991, **138**, 2207-2211.

15.   X. L. Zeng, P. Wu, F. L. Luo, C. Zhou and D. G. Tong, *J Phys Chem Solids*, 2010, **71**, 1404-1409.

16.   T. D. Ge, T. A. Dong, C. Wei, T. L. Xing, H. K. Long, H. Yi and J. X. Yang, *Mater Chem Phys*, 2008, **107**, 385-391.

17.   Y. A. Gao, M. V. Yakovleva and W. B. Ebner, *Electrochem Solid St*, 1998, **1**, 117-119.

18.   A. R. Armstrong and P. G. Bruce, *Nature*, 1996, **381**, 499-500.

19.   B. Ammundsen, *Proc. Int. Symp. Electrochem. Soc.*, 2000, **99-24**, 57-67.

20.   J. O. Besenhard and M. Winter, *Pure Appl Chem*, 1998, **70**, 603-608.

21.   G. Amatucci, A. Du Pasquier, A. Blyr, T. Zheng and J. M. Tarascon, *Electrochimica Acta*, 1999, **45**, 255-271.

22.   G. G. Amatucci, N. Pereira, T. Zheng, I. Plitz and J. M. Tarascon, *J. Power Sources*, 1999, **81**, 39-43.

23.   Y. X. Qian, Y. F. Deng, Z. C. Shi, Y. B. Zhou, Q. C. Zhuang and G. H. Chen, *Electrochem Commun*, 2013, **27**, 92-95.

24.   D. Aurbach, B. Markovsky, Y. Talyossef, G. Salitra, H. J. Kim and S. Choi, *J. Power Sources*, 2006, **162**, 780-789.

25.   C. Arbizzani, F. De Giorgio, L. Porcarelli, M. Mastragostino, V. Khomenko, V. Barsukov, D. Bresser and S. Passerini, *J. Power Sources*, 2013, **238**, 17-20.

26.   A. K. Padhi, K. S. Nanjundaswamy, C. Masquelier and J. B. Goodenough, *J. Electrochem. Soc.*, 1997, **144**, 2581-2586.

27.   A. K. Padhi, K. S. Nanjundaswamy, C. Masquelier, S. Okada and J. B. Goodenough, *J. Electrochem. Soc.*, 1997, **144**, 1609-1613.

28.   H. Li, Z. X. Wang, L. Q. Chen and X. J. Huang, *Adv Mater*, 2009, **21**, 4593-4607.

29.   G. X. Wang, H. Liu, J. Liu, S. Z. Qiao, G. Q. M. Lu, P. Munroe and H. Ahn, *Adv Mater*, 2010, **22**, 4944-4949.

30.   A. S. Andersson, B. Kalska, L. Haggstrom and J. O. Thomas, *Solid State Ion.*, 2000, **130**, 41-52.

31.   N. N. Bramnik and H. Ehrenberg, *J Alloy Compd*, 2008, **464**, 259-264.

32.   S. K. Martha, B. Markovsky, J. Grinblat, Y. Gofer, O. Haik, E. Zinigrad, D. Aurbach, T. Drezen, D. Wang, G. Deghenghi and I. Exnar, *J. Electrochem. Soc.*, 2009, **156**, A541-A552.

33.   Q. D. Truong, M. K. Deyaraju, Y. Sasaki, H. Hyodo, T. Tomai and I. Honma, *Chem. Mater*, 2014, **26**, 2770-2773.

34.   T. N. L. Doan and I. Taniguchi, *J. Power Sources*, 2011, **196**, 1399-1408.

35.   D. Y. Wang, H. Buqa, M. Crouzet, G. Deghenghi, T. Drezen, I. Exnar, N. H. Kwon, J. H. Miners, L. Poletto and M. Graetzel, *J. Power Sources*, 2009, **189**, 624-628.

36.   S. K. Martha, J. Grinblat, O. Haik, E. Zinigrad, T. Drezen, J. H. Miners, I. Exnar, A. Kay, B. Markovsky and D. Aurbach, *Angew. Chem. Int. Edit.*, 2009, **48**, 8559-8563.

37.   R. Sharabi, E. Markevich, V. Borgel, G. Salitra, D. Aurbach, G. Semrau, M. A. Schmidt, N. Schall and C. Stinner, *Electrochem. Commun.*, 2011, **13**, 800-802.

38.   C. Delmas, S. Brethes and M. Menetrier, *Cr. Acad. Sci. Ii.*, 1990, **310**, 1425-1430.

39.   K. Nassau and D. W. Murphy, *J. Non-Cryst. Solids*, 1981, **44**, 297-304.

40.   J. Desilvestro and O. Haas, *J. Electrochem. Soc.*, 1990, **137**, C5-C22.

41.   G. Pistoia, M. Pasquali, G. Wang and L. Li, *J. Electrochem. Soc.*, 1990, **137**, 2365-2370.

42.   B. Z. C. K .West, S. Skaarup, Y. Saidi, J. Barker, I. I.Olsen, R. Pynenburg, R. Koksbang, *J. Electrochem.. Soc*, 1996, **143**, 830.

43.   F. Bonino, A. Selvaggi and B. Scrosati, *Solid State Ion.*, 1988, **28**, 853-856.

44.   Z. H. Liu, Q. Yao and L. M. Liu, *J. Power Sources*, 1993, **45**, 15-19.

45.   J. X. Dai, S. F. Y. Li, Z. Q. Gao and K. S. Siow, *J. Electrochem. Soc.*, 1998, **145**, 3057-3062.

46.   J. Kawakita, Y. Katayama, T. Miura and T. Kishi, *Solid State Ion.*, 1998, **107**, 145-152.

47.   G. Pistoia, M. Pasquali, G. Wang and L. Li, *J. Electrochem. Soc.*, 1990, **137**, 2365-2370.

48.   M. Y. Saidi, I. I. Olsen, R. Koksbang, J. Barker, R. Pynenburg, K. West, B. Zachauchristiansen and S. Skaarup, *Solid State Ionics Iv*, 1995, **369**, 201-209.

49.   J. Kawakita, T. Kato, Y. Katayama, T. Miura and T. Kishi, *J. Power Sources*, 1999, **81**, 448-453.

50.   L. A. Depicciotto, K. T. Adendorff, D. C. Liles and M. M. Thackeray, *Solid State Ion.*, 1993, **62**, 297-307.

51.   J. Kawakita, T. Miura and T. Kishi, *J. Power Sources*, 1999, **83**, 79-83.

52.   H. Y. Xu, H. Wang, Z. Q. Song, Y. W. Wang, H. Yan and M. Yoshimura, *Electrochimica Acta*, 2004, **49**, 349-353.

53.   C. J. Cui, G. M. Wu, J. Shen, B. Zhou, Z. H. Zhang, H. Y. Yang and S. F. She, *Electrochimica Acta*, 2010, **55**, 2536-2541.

54.   N. H. Idris, M. M. Rahman, J. Z. Wang, Z. X. Chen and H. K. Liu, *Composites Science and Technology*, 2011, **71**, 343-349.

55.   C. Q. Feng, S. Y. Chew, Z. P. Guo, J. Z. Wang and H. K. Liu, *J. Power Sources*, 2007, **174**, 1095-1099.

56.   P. He, H. J. Yu, D. Li and H. S. Zhou, *J. Mater Chem*, 2012, **22**, 3680-3695.

57.   H. J. Yu and H. S. Zhou, *J. Phys. Chem. Lett.*, 2013, **4**, 1268-1280.

58.   B. H. Song, Z. W. Liu, M. O. Lai and L. Lu, *Phys. Chem. Chem. Phys.*, 2012, **14**, 12875-12883.

59.   A. Boulineau, L. Simonin, J. F. Colin, C. Bourbon and S. Patoux, *Nano Letters*, 2013, **13**, 3857-3863.

60.   C. C. Wang and A. Manthiram, *J. Materials Chemistry A*, 2013, **1**, 10209-10217.

61.   M. Gu, A. Genc, I. Belharouak, D. P. Wang, K. Amine, S. Thevuthasan, D. R. Baer, J. G. Zhang, N. D. Browning, J. Liu and C. M. Wang, *Chem. Mater*, 2013, **25**, 2319-2326.

62.   H. Shirakawa, E. J. Louis, A. G. Macdiarmid, C. K. Chiang and A. J. Heeger, *J. Chem . Soc. Chem. Comm.*, 1977, 578-580.

63.   P. Passiniemi and J. E. Osterholm, *Synthetic Met.*, 1987, **18**, 637-644.

64.   A. Ivaska, J. E. Osterholm, P. Passiniemi, P. Kuivalainen, H. Isotalo and H. Stubb, *Synthetic Met.*, 1987, **21**, 215-221.

65.   J. Caja, R. B. Kaner, A. G. Macdiarmid, T. Uchida and W. L. Worrell, *J. Electrochem. Soc.*, 1984, **131**, C91-C91.

66.   J. Caja, R. B. Kaner and A. G. Macdiarmid, *J. Electrochem. Soc.*, 1984, **131**, 2744-2750.

67.   P. Novak, K. Muller, K. S. V. Santhanam and O. Haas, *Chem. Rev.*, 1997, **97**, 207-281.

68.   W. C. Su and J. O. Iroh, *Synthetic Met.*, 1998, **95**, 159-167.

69.   Y. Kudoh, K. Akami and Y. Matsuya, *Synthetic Met.*, 1998, **95**, 191-196.

70.   Y. F. Li, B. H. Deng, G. F. He, R. Q. Wang and C. H. Yang, *J. Appl. Polym. Sci.*, 2001, **79**, 350-355.

71.   Y. S. Cohen, M. D. Levi and D. Aurbach, *Langmuir*, 2003, **19**, 9804-9811.

72.   K. Naoi, H. Sakai, S. Ogano and T. Osaka, *J. Power Sources*, 1987, **20**, 237-242.

73.   T. Osaka, K. Naoi, H. Sakai and S. Ogano, *J. Electrochem. Soc.*, 1987, **134**, 285-289.

74.   S. Panero, P. Prosperi and B. Scrosati, *Electrochimica Acta*, 1987, **32**, 1465-1468.

75.   N. Mermilliod, J. Tanguy and F. Petiot, *J. Electrochem. Soc.*, 1986, **133**, 1073-1079.

76.   H. B. Wang, Y. Q. Zeng, K. L. Huang, S. Q. Liu and L. Q. Chen, *Electrochimica Acta*, 2007, **52**, 5102-5107.

77.   H. B. Zhao, A. B. Yuan, B. D. Liu, S. Y. Xing, X. Y. Wu and J. Q. Xu, *J. Appl. Electrochem.*, 2012, **42**, 139-144.

78.   X. Z. Ren, C. Shi, P. X. Zhang, Y. K. Jiang, J. H. Liu and Q. L. Zhang, *Mater. Sci. Eng. B-Adv. Funct. Solid-State Mater.*, 2012, **177**, 929-934.

79.   G. X. Wang, L. Yang, Y. Chen, J. Z. Wang, S. Bewlay and H. K. Liu, *Electrochimica Acta*, 2005, **50**, 4649-4654.

80.   J. Z. Wang, S. L. Chou, J. Chen, S. Y. Chew, G. X. Wang, K. Konstantinov, J. Wu, S. X. Dou and H. K. Liu, *Electrochem. Commun.*, 2008, **10**, 1781-1784.

81.   A. Du Pasquier, F. Orsini, A. S. Gozdz and J. M. Tarascon, *J. Power Sources*, 1999, **81**, 607-611.

82.   A. G. Macdiarmid, J. C. Chiang, A. F. Richter and A. J. Epstein, *Synthetic Met.*, 1987, **18**, 285-290.

83. S. W. Ng, K. G. Neoh, J. T. Sampanthar, E. T. Kang and K. L. Tan, *J. Phys. Chem. B*, 2001, **105**, 5618-5625.

84. W. S. Huang, B. D. Humphrey and A. G. Macdiarmid, *J. Chem. Soc. Farad. T .1.*, 1986, **82**, 2385-&.

85. F. Cheng, W. Tang, C. Li, J. Chen, H. Liu, P. Shen and S. Dou, *Chemistry – A European Journal*, 2006, **12**, 3082-3088.

86. A. R. Hopkins, D. D. Sawall, R. M. Villahermosa and R. A. Lipeles, *Thin Solid Films*, 2004, **469**, 304-308.

87. K. S. Ryu, K. M. Kim, S. G. Kang, G. J. Lee and S. H. Chang, *Solid State Ion.*, 2000, **135**, 229-234.

88. S. Taguchi and T. Tanaka, *J. Power Sources*, 1987, **20**, 249-252.

89. M. Mizumoto, M. Namba, S. Nishimura, H. Miyadera, M. Koseki and Y. Kobayashi, *Synthetic Met.*, 1989, **28**, C639-C646.

90. S. J. Choi and S. M. Park, *Adv. Mater.*, 2000, **12**, 1547-1549.

91. J. Liu, Y. H. Lin, L. Liang, J. A. Voigt, D. L. Huber, Z. R. Tian, E. Coker, B. Mckenzie and M. J. Mcdermott, *Chem-Eur J.*, 2003, **9**, 604-611.

92. A. R. Hopkins, R. A. Lipeles and W. Kao, *Thin Solid Films*, 2004, **447**, 474-480.

93. A. G. Macdiarmid, L. S. Yang, W. S. Huang and B. D. Humphrey, *Synthetic Met.*, 1987, **18**, 393-398.

94. N. A. Kaskhedikar and J. Maier, *Adv. Mater.*, 2009, **21**, 2664-2680.

95. J. L. Tirado, *Mat. Sci. Eng. R*, 2003, **40**, 103-136.

96. T. Shodai, S. Okada, S. Tobishima and J. Yamaki, *Solid State Ion.*, 1996, **86-8**, 785-789.

97. J. R. Dahn, T. Zheng, Y. H. Liu and J. S. Xue, *Science*, 1995, **270**, 590-593.

98.   H. Azuma, H. Imoto, S. Yamada and K. Sekai, *J. Power Sources*, 1999, **81**, 1-7.

99.   Q. Wang, H. Li, L. Q. Chen and X. J. Huang, *Solid State Ion.*, 2002, **152**, 43-50.

100.   Q. Wang, H. Li, L. Q. Chen and X. J. Huang, *Carbon*, 2001, **39**, 2211-2214.

101.   H. Li, L. H. Shi, Q. Wang, L. Q. Chen and X. J. Huang, *Solid State Ion.*, 2002, **148**, 247-258.

102.   M. Winter and J. O. Besenhard, *Electrochimica Acta*, 1999, **45**, 31-50.

103.   J. Yang, M. Wachtler, M. Winter and J. O. Besenhard, *Electrochem. Solid St.*, 1999, **2**, 161-163.

104.   R. A. Huggins, *J. Power Sources*, 1999, **81**, 13-19.

105.   M. Winter, J. O. Besenhard, M. E. Spahr and P. Novak, *Adv. Mater.*, 1998, **10**, 725-763.

106.   H. Lee, M. G. Kim, C. H. Choi, Y. K. Sun, C. S. Yoon and J. Cho, *J. Phys. Chem. B*, 2005, **109**, 20719-20723.

107.   I. Sandu, P. Moreau, D. Guyomard, T. Brousse and L. Roue, *Solid State Ion.*, 2007, **178**, 1297-1303.

108.   G. L. Cui, L. Gu, L. J. Zhi, N. Kaskhedikar, P. A. van Aken, K. Mullen and J. Maier, *Adv. Mater.*, 2008, **20**, 3079-3083.

109.   J. Saint, M. Morcrette, D. Larcher, L. Laffont, S. Beattie, J. P. Peres, D. Talaga, M. Couzi and J. M. Tarascon, *Adv. Funct. Mater.*, 2007, **17**, 1765-1774.

110.   H. Kim, B. Han, J. Choo and J. Cho, *Angew. Chem. Int. Edit.*, 2008, **47**, 10151-10154.

111.   S. Bourderau, T. Brousse and D. M. Schleich, *J. Power Sources*, 1999, **81**, 233-236.

112. S. L. Chou, X. W. Gao, J. Z. Wang, D. Wexler, Z. X. Wang, L. Q. Chen and H. K. Liu, *Dalton T.*, 2011, **40**, 12801-12807.

113. H. Wu and Y. Cui, *Nano Today*, 2012, **7**, 414-429.

114. J. R. Szczech and S. Jin, *Energy & Environmental Science*, 2011, **4**, 56-72.

115. B. Key, R. Bhattacharyya, M. Morcrette, V. Seznec, J. M. Tarascon and C. P. Grey, *J. Am. Chem. Soc.*, 2009, **131**, 9239-9249.

116. T. D. Hatchard and J. R. Dahn, *J. Electrochem. Soc.*, 2004, **151**, A838-A842.

117. N. G. Rudawski, B. R. Yates, M. R. Holzworth, K. S. Jones, R. G. Elliman and A. A. Volinsky, *J. Power Sources*, 2013, **223**, 336-340.

118. C. H. Kim, H. S. Im, Y. J. Cho, C. S. Jung, D. M. Jang, Y. Myung, H. S. Kim, S. H. Back, Y. R. Lim, C. W. Lee, J. Park, M. S. Song and W. I. Cho, *J. Phys. Chem. C*, 2012, **116**, 26190-26196.

119. A. M. Chockla, K. C. Klavetter, C. B. Mullins and B. A. Korgel, *ACS Appl.. Mater. Interfaces*, 2012, **4**, 4658-4664.

120. M. H. Park, M. G. Kim, J. Joo, K. Kim, J. Kim, S. Ahn, Y. Cui and J. Cho, *Nano Letters*, 2009, **9**, 3844-3847.

121. L. Yuan, J. Wang, S. Y. Chew, J. Chen, Z. P. Guo, L. Zhao, K. Konstantinov and H. K. Liu, *J. Power Sources*, 2007, **174**, 1183-1187.

122. L. F. Cui, J. A. Shen, F. Y. Cheng, Z. L. Tao and J. Chen, *J. Power Sources*, 2011, **196**, 2195-2201.

123. Y. J. Jung, N. Singh and K. S. Choi, *Angew. Chem. Int. Edit.*, 2009, **48**, 8331-8334.

124. S. Y. Chew, Z. P. Guo, J. Z. Wang, J. Chen, P. Munroe, S. H. Ng, L. Zhao and H. K. Liu, *Electrochem. Commun.*, 2007, **9**, 941-946.

125. P. Poizot, S. Laruelle, S. Grugeon, L. Dupont and J. M. Tarascon, *Nature*, 2000, **407**, 496-499.

126. F. Badway, N. Pereira, F. Cosandey and G. G. Amatucci, *J. Electrochem. Soc.*, 2003, **150**, A1209-A1218.

127. F. Badway, N. Pereira, F. Cosandey and G. G. Amatucci, *Solid State Ion.-2002*, 2003, **756**, 207-218.

128. P. Poizot, S. Laruelle, S. Grugeon and J. M. Tarascon, *J. Electrochem. Soc.*, 2002, **149**, A1212-A1217.

129. H. Li, G. Richter and J. Maier, *Adv. Mater.*, 2003, **15**, 736-739.

130. E. Peled and H. Yamin, *J. Electrochem. Soc.*, 1979, **126**, C308-C308.

131. A. S. Arico, P. Bruce, B. Scrosati, J. M. Tarascon and W. Van Schalkwijk, *Nat. Mater.*, 2005, **4**, 366-377.

132. P. Simon and Y. Gogotsi, *Nat. Mater.*, 2008, **7**, 845-854.

133. L. F. Hu, L. M. Wu, M. Y. Liao, X. H. Hu and X. S. Fang, *Adv. Funct. Mater.*, 2012, **22**, 998-1004.

134. T. Y. Wei, C. H. Chen, H. C. Chien, S. Y. Lu and C. C. Hu, *Adv. Mater.*, 2010, **22**, 347.

135. P. F. Teh, Y. Sharma, S. S. Pramana and M. Srinivasan, *J. Mater. Chem.*, 2011, **21**, 14999-15008.

136. W. Luo, X. L. Hu, Y. M. Sun and Y. H. Huang, *J. Mater. Chem.*, 2012, **22**, 8916-8921.

137. G. Q. Zhang, B. Y. Xia, C. Xiao, L. Yu, X. Wang, Y. Xie and X. W. Lou, *Angew. Chem. Int. Edit.*, 2013, **52**, 8643-8647.

138. H. L. Wang, Q. M. Gao and L. Jiang, *Small*, 2011, **7**, 2454-2459.

139.	C. Z. Yuan, J. Y. Li, L. R. Hou, L. Yang, L. F. Shen and X. G. Zhang, *J Mater Chem*, 2012, **22**, 16084-16090.

140.	D. G. Zhang, Z. W. Tong, G. Y. Xu, S. Z. Li and J. J. Ma, *Solid State Sci*, 2009, **11**, 113-117.

141.	G. Q. Zhang, H. B. Wu, H. E. Hoster, M. B. Chan-Park and X. W. Lou, *Energy & Environmental Science*, 2012, **5**, 9453-9456.

142.	J. P. Liu, Y. Y. Li, H. J. Fan, Z. H. Zhu, J. Jiang, R. M. Ding, Y. Y. Hu and X. T. Huang, *Chem Mater*, 2010, **22**, 212-217.

143.	M. V. Reddy, T. Yu, C. H. Sow, Z. X. Shen, C. T. Lim, G. V. S. Rao and B. V. R. Chowdari, *Adv Funct Mater*, 2007, **17**, 2792-2799.

144.	P. Lavela and J. L. Tirado, *J. Power Sources*, 2007, **172**, 379-387.

145.	M. Bomio, P. Lavela and J. L. Tirado, *J Solid State Electr*, 2008, **12**, 729-737.

146.	N. Sivakumar, S. R. P. Gnanakan, K. Karthikeyan, S. Amaresh, W. S. Yoon, G. J. Park and Y. S. Lee, *J Alloy Compd*, 2011, **509**, 7038-7041.

147.	N. Sharma, K. M. Shaju, G. V. S. Rao and B. V. R. Chowdari, *J. Power Sources*, 2003, **124**, 204-212.

148.	Y. Sharma, N. Sharma, G. V. S. Rao and B. V. R. Chowdari, *Electrochimica Acta*, 2008, **53**, 2380-2385.

149.	X. W. Lou, D. Deng, J. Y. Lee, J. Feng and L. A. Archer, *Adv Mater*, 2008, **20**, 258-+.

150.	Y. N. NuLi, Y. Q. Chu and Q. Z. Qin, *J. Electrochem. Soc.*, 2004, **151**, A1077-A1083.

151.	Z. Xing, Z. C. Ju, J. Yang, H. Y. Xu and Y. T. Qian, *Nano Res*, 2012, **5**, 477-485.

152. X. W. Guo, X. Lu, X. P. Fang, Y. Mao, Z. X. Wang, L. Q. Chen, X. X. Xu, H. Yang and Y. N. Liu, *Electrochem Commun*, 2010, **12**, 847-850.

153. N. Ponpandian, A. Narayanasamy, C. N. Chinnasamy, N. Sivakumar, J. M. Greneche, K. Chattopadhyay, K. Shinoda, B. Jeyadevan and K. Tohji, *Appl Phys Lett*, 2005, **86**.

154. D. Guyomard and J. M. Tarascon, *J. Electrochem. Soc.*, 1992, **139**, 937-948.

155. J. M. Tarascon, W. R. Mckinnon, F. Coowar, T. N. Bowmer, G. Amatucci and D. Guyomard, *J. Electrochem. Soc.*, 1994, **141**, 1421-1431.

156. K. Xu, *Chem Rev*, 2004, **104**, 4303-4417.

157. P. Verma, P. Maire and P. Novak, *Electrochimica Acta*, 2010, **55**, 6332-6341.

158. D. Aurbach, M. D. Levi, K. Gamulski, B. Markovsky, G. Salitra, E. Levi, U. Heider, L. Heider and R. Oesten, *J. Power Sources*, 1999, **81**, 472-479.

159. E. Zinigrad, L. Larush-Asraf, J. S. Gnanaraj, M. Sprecher and D. Aurbach, *Thermochim Acta*, 2005, **438**, 184-191.

160. S. Yonezawa, M. Yamasaki and M. Takashima, *J Fluorine Chem*, 2004, **125**, 1657-1661.

161. D. Yaakov, Y. Gofer, D. Aurbach and I. C. Halalay, *J. Electrochem. Soc.*, 2010, **157**, A1383-A1391.

162. L. J. Fu, H. Liu, C. Li, Y. P. Wu, E. Rahm, R. Holze and H. Q. Wu, *Solid State Sci*, 2006, **8**, 113-128.

163. N. Byrne, P. C. Howlett, D. R. MacFarlane and M. Forsyth, *Adv Mater*, 2005, **17**, 2497-2501.

164. S. L. Chou, J. Z. Wang, J. Z. Sun, D. Wexler, M. Forsyth, H. K. Liu, D. R. MacFarlane and S. X. Dou, *Chem Mater*, 2008, **20**, 7044-7051.

165. S. Fang, Z. Zhang, Y. Jin, L. Yang, S.-i. Hirano, K. Tachibana and S. Katayama, *J. Power Sources*, 2011, **196**, 5637-5644.

166. M. Galinski, A. Lewandowski and I. Stepniak, *Electrochimica Acta*, 2006, **51**, 5567-5580.

167. H. Sakaebe, H. Matsumoto and K. Tatsumi, *J. Power Sources*, 2005, **146**, 693-697.

168. K. Hayashi, Y. Nemoto, K. Akuto and Y. Sakurai, *J. Power Sources*, 2005, **146**, 689-692.

169. A. Guerfi, S. Duchesne, Y. Kobayashi, A. Vijh and K. Zaghib, *J. Power Sources*, 2008, **175**, 866-873.

170. A. Lewandowski and A. Swiderska-Mocek, *J. Power Sources*, 2009, **194**, 601-609.

171. A. Fernicola, F. Croce, B. Scrosati, T. Watanabe and H. Ohno, *J. Power Sources*, 2007, **174**, 342-348.

172. J. M. G. Cowie, *Polymers: Chemistry and Physics of Modern Materials*, Chapman and Hall, 1991.

173. J. Clayden, N. Greeves and S. Warren, *Organic chemistry*, Oxford University Press, 2000.

174. M. Armand and J. M. Tarascon, *Nature*, 2008, **451**, 652-657.

175. M. S. Whittingham, *Chem. Rev.*, 2004, **104**, 4271-4302.

176. H. Lee and J. Cho, *Nano Lett.*, 2007, **7**, 2638-2641.

177. L. F. Cui, R. Ruffo, C. K. Chan, H. L. Peng and Y. Cui, *Nano Letters*, 2009, **9**, 491-495.

178. K. H. Seng, M. H. Park, Z. P. Guo, H. K. Liu and J. Cho, *Angewandte Chemie*, 2012, **124**, 5755-5759.

179.   Y. Wang, M. Wu, Z. Jiao and J. Y. Lee, *Chem. Mater.*, 2009, **21**, 3210-3215.

180.   J. Graetz, C. C. Ahn, R. Yazami and B. Fultz, *J. Electrochem. Soc.*, 2004, **151**, A698-A702.

181.   C. K. Chan, X. F. Zhang and Y. Cui, *Nano Letters*, 2008, **8**, 307-309.

182.   M. Winter and J. O. Besenhard, *Electrochimica Acta*, 1999, **45**, 31-50.

183.   A. Magasinski, P. Dixon, B. Hertzberg, A. Kvit, J. Ayala and G. Yushin, *Nat.. Mater.*, 2010, **9**, 353-358.

184.   L. C. Yang, Q. S. Gao, L. Li, Y. Tang and Y. P. Wu, *Electrochem.. Commun.*, 2010, **12**, 418-421.

185.   G. Jo, I. Choi, H. Ahn and M. J. Park, *Chem Commun*, 2012, **48**, 3987-3989.

186.   R. A. DiLeo, S. Frisco, M. J. Ganter, R. E. Rogers, R. P. Raffaelle and B. J. Landi, *J Phys Chem C*, 2011, **115**, 22609-22614.

187.   R. A. DiLeo, M. J. Ganter, R. P. Raffaelle and B. J. Landi, *J. Mater. Res.*, 2010, **25**, 1441-1446.

188.   A. M. Chockla, M. G. Panthani, V. C. Holmberg, C. M. Hessel, D. K. Reid, T. D. Bogart, J. T. Harris, C. B. Mullins and B. A. Korgel, *J. Phys. Chem. C*, 2012, **116**, 11917-11923.

189.   J. S. Cheng and J. Du, *Crystengcomm.*, 2012, **14**, 397-400.

190.   Z. P. Guo, J. Z. Wang, H. K. Liu and S. X. Dou, *J. Power Sources*, 2005, **146**, 448-451.

191.   L. Yuan, J. Wang, S. Y. Chew, J. Chen, Z. P. Guo, L. Zhao, K. Konstantinov and H. K. Liu, *J. Power Sources*, 2007, **174**, 1183-1187.

192.   Z. J. Du, S. C. Zhang, Y. Liu, J. F. Zhao, R. X. Lin and T. Jiang, *J. Mater. Chem,.* 2012, **22**, 11636-11641.

193. X. Liang, Z. Y. Wen, Y. Liu, H. Zhang, J. Jin, M. F. Wu and X. W. Wu, *J. Power Sources*, 2012, **206**, 409-413.

194. C. Lai, G. R. Li, Y. Y. Dou and X. P. Gao, *Electrochimica Acta*, 2010, **55**, 4567-4572.

195. P. M. Dziewonski and M. Grzeszczuk, *Electrochimica Acta*, 2010, **55**, 3336-3347.

196. K. S. Park, S. B. Schougaard and J. B. Goodenough, *Adv. Mater.*, 2007, **19**, 848.

197. I. Boyano, J. A. Blazquez, I. de Meatza, M. Bengoechea, O. Miguel, H. Grande, Y. H. Huang and J. B. Goodenough, *J. Power Sources*, 2010, **195**, 5351-5359.

198. S. Y. Chew, C. Feng, S. H. Ng, J. Wang, Z. Guo and H. Liu, *J. Electrochem. Soc.*, 2007, **154**, A633-A637.

199. J. H. Wu, Y. G. Sun, R. J. Zou, G. S. Song, Z. G. Chen, C. R. Wang and J. Q. Hu, *Crystengcomm.*, 2011, **13**, 3674-3677.

200. Y. F. Zhang, Y. H. Tang, N. Wang, C. S. Lee, I. Bello and S. T. Lee, *Phys. Rev. B*, 2000, **61**, 4518-4521.

201. Y. Furukawa, S. Tazawa, Y. Fujii and I. Harada, *Synthetic Met.*, 1988, **24**, 329-341.

202. M. J. L. Santos, A. G. Brolo and E. M. Girotto, *Electrochimica Acta*, 2007, **52**, 6141-6145.

203. F. Genoud, M. Guglielmi, M. Nechtschein, E. Genies and M. Salmon, *Phys. Rev. Lett.*, 1985, **55**, 118-121.

204. T. F. Otero, H. Grande and J. Rodríguez, *J. Electroanalytic. Chem.*, 1995, **394**, 211-216.

205. L. Baggetto and P. H. L. Notten, *J. Electrochem. Soc.*, 2009, **156**, A169-A175.

206. S. Yoon, C. M. Park and H. J. Sohn, *Electrochem. Solid. St.*, 2008, **11**, A42-A45.

207. H. Lee and J. Cho, *Nano Letters*, 2007, **7**, 2638-2641.

208. Y. Kudoh, *Synthetic Met.*, 1996, **79**, 17-22.

209. Y. S. Hu, Y. G. Guo, W. Sigle, S. Hore, P. Balaya and J. Maier, *Nat. Mater.*, 2006, **5**, 713-717.

210. M. H. Oh, T. Yu, S. H. Yu, B. Lim, K. T. Ko, M. G. Willinger, D. H. Seo, B. H. Kim, M. G. Cho, J. H. Park, K. Kang, Y. E. Sung, N. Pinna and T. Hyeon, *Science*, 2013, **340**, 964-968.

211. T. Brezesinski, J. Wang, S. H. Tolbert and B. Dunn, *Nat. Mater.*, 2010, **9**, 146-151.

212. J. Cabana, L. Monconduit, D. Larcher and M. R. Palacin, *Adv. Mater.*, 2010, **22**, E170-E192.

213. X. H. Wang, L. Qiao, X. L. Sun, X. W. Li, D. K. Hu, Q. Zhang and D. Y. He, *J. Mater. Chem. A*, 2013, **1**, 4173-4176.

214. M. M. Titirici, M. Antonietti and A. Thomas, *Chem. Mater.*, 2006, **18**, 3808-3812.

215. S. L. Chou, J. Z. Wang, D. Wexler, K. Konstantinov, C. Zhong, H. K. Liu and S. X. Dou, *J. Mater. Chem.*, 2010, **20**, 2092-2098.

216. Y. Ding, Y. F. Yang and H. X. Shao, *Solid State Ion.*, 2012, **217**, 27-33.

217. Y. Ding, Y. F. Yang and H. X. Shao, *Electrochimica Acta*, 2011, **56**, 9433-9438.

218. H. X. Zhao, Z. Zheng, K. W. Wong, S. M. Wang, B. J. Huang and D. P. Li, *Electrochem. Commun.*, 2007, **9**, 2606-2610.

219. H. W. Liu, H. Zhu and H. M. Yang, *Mater Res Bull*, 2013, **48**, 1587-1592.

220. H. X. Zhao, H. M. Jia, S. M. Wang, D. Q. Xue and Z. Zheng, *J. Exp. Nanosci.*, 2011, **6**, 75-83.

221. C. C. Ai, M. C. Yin, C. W. Wang and J. T. Sun, *J. Mater. Sci.*, 2004, **39**, 1077-1079.

222. Y. F. Deng, Q. M. Zhang, S. D. Tang, L. T. Zhang, S. N. Deng, Z. C. Shi and G. H. Chen, *Chem. Commun.*, 2011, **47**, 6828-6830.

223. N. N. Wang, H. Y. Xu, L. Chen, X. Gu, J. Yang and Y. T. Qian, *J. Power Sources*, 2014, **247**, 163-169.

224. C. T. Cherian, M. V. Reddy, G. V. S. Rao, C. H. Sow and B. V. R. Chowdari, *J. Solid State Electr.*, 2012, **16**, 1823-1832.

225. X. Li and G. S. Wang, *J. Magn .Magn. Mater.*, 2009, **321**, 1276-1279.

226. S. Zhou, X. D. Fang, Z. H. Deng, D. Li, W. W. Dong, R. H. Tao, G. Meng, T. Wang and X. B. Zhu, *J .Cryst. Growth*, 2008, **310**, 5375-5379.

227. W. Q. Jiang, Z. Cao, R. Gu, X. Z. Ye, C. F. Jiang and X. L. Gong, *Smart Mater .Struct.*, 2009, **18**.

228. X. H. Lin, G. B. Ji, Y. S. Liu, Q. H. Huang, Z. H. Yang and Y. W. Du, *Crystengcomm..*, 2012, **14**, 8658-8663.

229. J. Q. Wang, P. King and R. A. Huggins, *Solid State Ion.*, 1986, **20**, 185-189.

230. Y. Sharma, N. Sharma, G. V. S. Rao and B. V. R. Chowdari, *Adv. Funct. Mater.*, 2007, **17**, 2855-2861.

231. X. B. Zhu, S. L. Chou, L. Wang, Q. Li, D. Q. Shi, J. Z. Wang, Z. X. Chen, Y. P. Sun, H. K. Liu and S. X. Dou, *Electrochem . Solid St.*, 2009, **12**, A176-A180.

232. L. L. Li, S. J. Peng, Y. L. Cheah, Y. Ko, P. Teh, G. Wee, C. L. Wong and M. Srinivasan, *Chem-Eur. J.*, 2013, **19**, 14823-14830.

233. L. L. Li, S. J. Peng, Y. L. Cheah, P. F. Teh, J. Wang, G. Wee, Y. W. Ko, C. L. Wong and M. Srinivasan, *Chem-Eur. J.*, 2013, **19**, 5892-5898.

234. F. Bonino, S. Panero, M. Pasquali and G. Pistoia, *J. Power Sources*, 1995, **56**, 193-196.

235. V. Manev, A. Momchilov, A. Nassalevska, G. Pistoia and M. Pasquali, *J. Power Sources*, 1995, **54**, 501-507.

236. S. Panero, M. Pasquali and G. Pistoia, *J. Electrochem. Soc.*, 1983, **130**, 1225-1227.

237. Q. Liu, H. Liu, X. Zhou, C. Cong and K. Zhang, *Solid State Ion.*, 2005, **176**, 1549-1554.

238. S. H. Ju and Y. C. Kang, *Electrochimica Acta*, 2010, **55**, 6088-6092.

239. J. Xie, J. Li, H. Zhan and Y. Zhou, *Materials Letters*, 2003, **57**, 2682-2687.

240. Y. Liu, X. Zhou and Y. Guo, *Mater. Chem. Phys.*, 2009, **114**, 915-919.

241. M. Dubarry, J. Gaubicher, D. Guyomard, N. Dupré and C. Grey, *Solid State Ion.*, 2009, **180**, 1511-1516.

242. H. Liu, Y. Wang, K. Wang, Y. Wang and H. Zhou, *J. Power Sources*, 2009, **192**, 668-673.

243. S. Jouanneau, A. L. G. L. Salle, A. Verbaere and D. Guyomard, *J. Electrochem.. Soc.*, 2005, **152**, A1660-A1667.

244. Q. Gong, Y. S. He, Y. Yang, X. Z. Liao and Z. F. Ma, *J. Solid State Electr.*, 2012, **16**, 1383-1388.

245. A. D. Pasquier, F. Orsini, A. S. Gozdz and J. M. Tarascon, *J. Power Sources*, 1999, **81–82**, 607-611.

246.   R. Vidu and P. Stroeve, *Industrial & Engineering Chemistry Research*, 2004, **43**, 3314-3324.

247.   J. Wang, J. Chen, K. Konstantinov, L. Zhao, S. H. Ng, G. X. Wang, Z. P. Guo and H. K. Liu, *Electrochimica Acta*, 2006, **51**, 4634-4638.

248.   I. Boyano, J. A. Blazquez, I. de Meatza, M. Bengoechea, O. Miguel, H. Grande, Y. Huang and J. B. Goodenough, *J. Power Sources*, 2010, **195**, 5351-5359.

249.   W. M. Chen, Y. H. Huang and L. X. Yuan, *J. Electroanalyt. Chem.*, 2011, **660**, 108-113.

250.   K. Parka, H. Songa, Y. Kima, C. a. c. i. S. Mhoa, *Electrochimica Acta*, 2010, **11**, 8023-8029.

251.   P. Novák, K. Müller, K. S. V. Santhanam and O. Haas, *Chem. Rev.*, 1997, **97**, 207-282.

252.   L. A. de Picciotto, K. T. Adendorff, D. C. Liles and M. M. Thackeray, *Solid State Ion.*, 1993, **62**, 297-307.

253.   X. Zhang and R. Frech, *Electrochimica Acta*, 1997, **43**, 861-868.

254.   M. Jain and S. Annapoorni, *Synthetic Met.*, 2010, **160**, 1727-1732.

255.   L. Liu, L. Jiao, J. Sun, Y. Zhang, M. Zhao, H. Yuan and Y. Wang, *Electrochimica Acta*, 2008, **53**, 7321-7325.

256.   J. Kawakita, Y. Katayama, T. Miura and T. Kishi, *Solid State Ion.*, 1998, **107**, 145-152.

257.   M. Dubarry, J. Gaubicher, D. Guyomard, N. Steunou, J. Livage, N. Dupré and C. P. Grey, *Chem. Mater.*, 2006, **18**, 629-636.

258.   J. B. Goodenough, *Accounts Chem. Res.*, 2013, **46**, 1053-1061.

259.   J. F. von Bulow, H.-L. Zhang and D. E. Morse, *Adv. Energy Mater.*, 2012, **2**, 309-315.

260.   J. Hassoun, K. S. Lee, Y. K. Sun and B. Scrosati, *J. Am. Chem. Soc.*, 2011, **133**, 3139-3143.

261.   Q. M. Zhong, A. Bonakdarpour, M. J. Zhang, Y. Gao and J. R. Dahn, *J. Electrochem. Soc.*, 1997, **144**, 205-213.

262.   L. Zhou, D. Y. Zhao and X. W. Lou, *Angew. Chem. Int. Edit.*, 2012, **51**, 239-241.

263.   N. P. W. Pieczonka, Z. Y. Liu, P. Lu, K. L. Olson, J. Moote, B. R. Powell and J. H. Kim, *J. Phys. Chem. C*, 2013, **117**, 15947-15957.

264.   J. B. Goodenough and Y. Kim, *ChemInform.*, 2010, **41**, no-no.

265.   R. Prasad, R. Benedek, A. J. Kropf, C. S. Johnson, A. D. Robertson, P. G. Bruce and M. M. Thackeray, *Phys. Rev. B*, 2003, **68**.

266.   X. Hao and B. M. Bartlett, *J. Electrochem. Soc.*, 2013, **160**, A3162-A3170.

267.   R. Benedek, M. M. Thackeray, J. Low and T. Bucko, *J. Phys. Chem. C*, 2012, **116**, 4050-4059.

268.   Y. K. Sun, K. J. Hong, J. Prakash and K. Amine, *Electrochem. Commun.*, 2002, **4**, 344-348.

269.   J. Mun, T. Yim, K. Park, J. H. Ryu, Y. G. Kim and S. M. Oh, *J. Electrochem.. Soc.*, 2011, **158**, A453-A457.

270.   Y. K. Sun, Y. S. Lee, M. Yoshio and K. Amine, *J. Electrochem.. Soc.*, 2003, **150**, L11-L11.

271.   J. C. Arrebola, A. Caballero, L. Hernan and J. Morales, *J. Power Sources*, 2010, **195**, 4278-4284.

272.   B. Huang, X. H. Li, Z. X. Wang, H. J. Guo, X. H. Xiong and J. X. Wang, *J. Alloy Compd.*, 2014, **583**, 313-319.

273.   T. Noguchi, I. Yamazaki, T. Numata and M. Shirakata, *J. Power Sources*, 2007, **174**, 359-365.

274.   Z. Qiao, O. Sha, Z. Y. Tang, J. Yan, S. L. Wang, H. B. Liu, Q. Xu and Y. J. Su, *Mater. Lett.*, 2012, **87**, 176-179.

275.   D. Liu, J. Trottier, P. Charest, J. Frechette, A. Guerfi, A. Mauger, C. M. Julien and K. Zaghib, *J. Power Sources*, 2012, **204**, 127-132.

276.   D. Liu, Y. Bai, S. Zhao and W. Zhang, *J. Power Sources*, 2012, **219**, 333-338.

277.   J. Liu and A. Manthiram, *Chem. Mater.*, 2009, **21**, 1695-1707.

278.   T. Y. Yang, N. Q. Zhang, Y. Lang and K. N. Sun, *Electrochimica Acta*, 2011, **56**, 4058-4064.

279.   X. Fang, M. Ge, J. Rong and C. Zhou, *J. Mater. Chem. A*, 2013, **1**, 4083-4088.

280.   H. Guo, L. Liu, H. Shu, X. Yang, Z. Yang, M. Zhou, J. Tan, Z. Yan, H. Hu and X. Wang, *J. Power Sources*, 2014, **247**, 117-126.

281.   M. Sugita, H. Noguchi, Y. Soejima and M. Yoshio, *Electrochemistry*, 2000, **68**, 587-590.

282.   J. U. Kim, I. S. Jeong, S. I. Moon and H. B. Gu, *J. Power Sources*, 2001, **97-8**, 450-453.

283.   J. H. Park, J. H. Cho, E. H. Lee, J. M. Kim and S. Y. Lee, *J. Power Sources*, 2013, **244**, 442-449.

284.   J. H. Cho, J. H. Park, M. H. Lee, H. K. Song and S. Y. Lee, *Energy & Environmental Science*, 2012, **5**, 7124-7131.

285.   Y. Deng, Z. Li, Z. Shi, H. Xu, F. Peng and G. Chen, *RSC Adv.*, 2012, **2**, 4645-4647.

286. K. Amine, H. Tukamoto, H. Yasuda and Y. Fujita, *J. Electrochem. Soc.*, 1996, **143**, 1607-1613.

287. N. M. Hagh, F. Cosandey, S. Rangan, R. Bartynski and G. G. Amatucci, *J. Electrochem. Soc.*, 2010, **157**, A305-A319.

288. D. Aurbach, K. Gamolsky, B. Markovsky, G. Salitra, Y. Gofer, U. Heider, R. Oesten and M. Schmidt, *J. Electrochem. Soc.,* 2000, **147**, 1322-1331.

289. T. Ohzuku, S. Takeda and M. Iwanaga, *J. Power Sources*, 1999, **81–82**, 90-94.

290. Q. Zhong, A. Bonakdarpour, M. Zhang, Y. Gao and J. R. Dahn, *J. Electrochem. Soc.*, 1997, **144**, 205-213.

291. K. Ariyoshi, Y. Iwakoshi, N. Nakayama and T. Ohzuku, *J. Electrochem. Soc.*, 2004, **151**, A296-A303.

292. J. S. Wilkes and M. J. Zaworotko, *J. Chem. Soc. Chem. Comm.*, 1992, 965-967.

293. M. Galiński, A. Lewandowski and I. Stępniak, *Electrochimica Acta*, 2006, **51**, 5567-5580.

294. M. Armand, F. Endres, D. R. MacFarlane, H. Ohno and B. Scrosati, *Nat. Mater.*, 2009, **8**, 621-629.

295. J. Wang, S. Y. Chew, Z. W. Zhao, S. Ashraf, D. Wexler, J. Chen, S. H. Ng, S. L. Chou and H. K. Liu, *Carbon*, 2008, **46**, 229-235.

296. L. X. Yuan, J. K. Feng, X. P. Ai, Y. L. Cao, S. L. Chen and H. X. Yang, *Electrochem. Commun.*, 2006, **8**, 610-614.

297. J. Z. Wang, S. L. Chou, S. Y. Chew, J. Z. Sun, M. Forsyth, D. R. MacFarlane and H. K. Liu, *Solid State Ion.*, 2008, **179**, 2379-2382.

298.   S. L. Chou, J. Z. Wang, J. Z. Sun, D. Wexler, M. Forsyth, H. K. Liu, D. R. MacFarlane and S. X. Dou, *Chem. Mater.*, 2008, **20**, 7044-7051.

299.   S. Y. Chew, J. Sun, J. Wang, H. Liu, M. Forsyth and D. R. MacFarlane, *Electrochimica Acta*, 2008, **53**, 6460-6463.

300.   D. R. MacFarlane, P. Meakin, J. Sun, N. Amini and M. Forsyth, *J. Phys. Chem. B*, 1999, **103**, 4164-4170.

301.   P. C. Howlett, D. R. MacFarlane and A. F. Hollenkamp, *Electrochem. Solid St.*, 2004, **7**, A97-A101.

302.   M. Kunduraci and G. G. Amatucci, *J. Power Sources*, 2007, **165**, 359-367.

303.   J. Cabana, S.-H. Kang, C. S. Johnson, M. M. Thackeray and C. P. Grey, *J. Electrochem. Soc.*, 2009, **156**, A730-A736.

304.   H. Wang, H. Xia, M. O. Lai and L. Lu, *Electrochem. Commun.*, 2009, **11**, 1539-1542.

305.   T. Ohzuku, K. Ariyoshi, S. Takeda and Y. Sakai, *Electrochimica Acta*, 2001, **46**, 2327-2336.

306.   P. C. Howlett, N. Brack, A. F. Hollenkamp, M. Forsyth and D. R. MacFarlane, *J. Electrochem. Soc.*, 2006, **153**, A595-A606.

307.   P. C. Howlett, E. I. Izgorodina, M. Forsyth and D. R. MacFarlane, *Zeitschrift für Physikalische Chemie*, 2006, **220**, 1483-1498.

308.   S. B. Park, W. S. Eom, W. I. Cho and H. Jang, *J. Power Sources*, 2006, **159**, 679-684.

309.   H. Sakaebe, H. Matsumoto and K. Tatsumi, *Electrochimica Acta*, 2007, **53**, 1048-1054.

310.   B. S. C.A. Vincent, ed., *Modern Batteries. Wiley*, 1997.

311.   K. Hayashi, Y. Nemoto, K. Akuto and Y. Sakurai, *J. Power Sources*, 2005, **146**, 689-692.

312.   A. Zaban, E. Zinigrad and D. Aurbach, *J. Phys. Chem.*, 1996, **100**, 3089-3101.

313.   D. Aurbach, I. Weissman, A. Zaban and O. Chusid, *Electrochimica Acta*, 1994, **39**, 51-71.

314.   D. Aurbach, B. Markovsky, A. Shechter, Y. EinEli and H. Cohen, *J. Electrochem. Soc.*, 1996, **143**, 3809-3820.

APPENDIX A: PUBLICATIONS

1. Gao, X. W., Wang, J. Z., Chou, S. L., Liu, H. K. Synthesis and electrochemical performance of LiV_3O_8/polyaniline as cathode material for the lithium battery. *J. Power Sources* **220**, 47-53, (2012).

2. Gao, X. W., Feng, C. Q., Chou, S. L., Wang, J. Z., Sun, J. Z., Forsyth. M., MacFarlane, D. R., Liu, H. K., $LiNi_{0.5}Mn_{1.5}O_4$ spinel cathode using room temperature ionic liquid as electrolyte. *Electrochimica Acta* **101**, 151-157, (2013).

3. Gao, X. W., Luo, W. B., Zhong, C., Wexler, D., Chou, S. L., Liu, H. K., Shi, Z. C., Chen, G. H., Ozawa, K., Wang, J. Z., Novel germanium/polypyrrole composite for high power lithium-ion battery, *Scientific Reports*, **4**, 6095, (2014).

4. Gao, X. W., Deng, Y. F., Wexler, D., Chen, G. H., Chou, S. L., Liu, H. K., Shi, Z. C., Wang, J. Z., Improving the electrochemical performance of $LiNi_{0.5}Mn_{1.5}O_4$ spinel by polypyrrole coating as cathode material for the lithium-ion battery, *Journal of Materials Chemistryl A,* **3(1)**, 404-411, (2015).

5. Zhang, M., **Gao, X. W**., Zi, Z. F., Dai, J. M., Wang, J. Z., Chou, S. L., Liang, C. H., Zhu, X. B., Sun, Y. P., Liu, H. K., Porous $Ni_{0.5}Zn_{0.5}Fe_2O_4$ Nanospheres: Synthesis, Characterization, and Application for Lithium Storage, (submitted to *Electrochimica. Acta*).

6. Chou, S. L. **Gao, X. W.**,Wang, J. Z.,Wexler, D., Wang, Z. X., Chen, L. Q., Liu, H, K., Tin/polypyrrole composite anode using sodium carboxymethyl cellulose binder for lithium-ion batteries. *Dalton T.,* **40**, 12801-12807, (2011).

7. Zhang, B. **Gao, X. W.**, Wang, J. Z., Chou, S. L., Konstantinov, K., Liu, H. K., CuS Nanoflakes, Microspheres, Microflowers, and Nanowires: Synthesis and Lithium Storage Properties., *Journal of Nanoscience and Nanotechnology,* **13**, 1309-1316, (2013).

8. Lu, L., Wang, J. Z., **Gao, X. W.**, Zhu, X. B., Liu, H. K. Enhanced Cycling Performance of Nanocrystalline Fe_3O_4/C as Anode Material for Lithium-Ion Batteries., *Journal of Nanoscience and Nanotechnology,* **12**, 1246-1250, (2012).

9. Zhong, C. Wang, J. Z., **Gao, X. W.**, Chou, S. L.,Konstantinov, K., Liu, H. K., One-Step Spray Pyrolysis Synthesized CuO-Carbon Composite Combined with Carboxymethyl Cellulose Binder as Anode for Lithium-Ion Batteries. *Journal of Nanoscience and Nanotechnology*, **12**, 1314-1317, (2012).

10. Zhong, C., Wang, J. Z., **Gao, X. W.,** Wexler, D., Liu, H. K. In situ one-step synthesis of a 3D nanostructured germanium-graphene composite and its application in lithium-ion batteries, *Journal of Materials Chemistry A* **1**, 10798-10804, (2013).

11. Lu, L., Wang, J. Z., Zhu, X. B., **Gao, X. W.,** Liu, H. K. High capacity and high rate capability of nanostructured $CuFeO_2$ anode materials for lithium-ion batteries. *J. Power Sources* **196**, 7025-7029, (2011).

12. Wang, J._,_ Wang, J. Z., Sun, Z. Q., **Gao, X. W.**, Zhong, C., Chou, S. L., Liu, H. K., A germanium/single-walled carbon nanotube composite paper as a free-standing anode for lithium-ion batteries. *Journal of Materials Chemistry A* **2**, 4613-4618, (2014).

APPENDIX B: RECEIVED AWARDS

2013 Chinese Government Award for Outstanding Self-financed Students Abroad, China Scholarship Council.

2013 Postgraduate Student Merit Award, Institute for Superconducting and Electronic Materials, University of Wollongong, 29 Apr. 2013.

Best poster Award, The Inaugural Asia-Pacific Conference on Electrochemical Energy Storage and Conversion (APEnergy 2014), Brisbane Convention & Exhibition Centre, University of Queensland, Australia, 5-8 Feb. 2014.

Best Poster Presentation Award, International Union of Materials Research Societies-International Conference on Electronic Materials 2010 (IUMRS-ICEM 2010), Seoul, Republic of Korea, 27 Aug. 2010.